Fall 2021

Development of a Multi-Scale Mechano-Electrochemical Battery Model

Drew J. Pereira

DEVELOPMENT OF A MULTI-SCALE MECHANO-ELECTROCHEMICAL BATTERY MODEL

by

Drew J. Pereira

Bachelor of Science
Missouri University of Science and Technology, 2015

Submitted in Partial Fulfillment of the Requirements

For the Degree of Doctor of Philosophy in

Chemical Engineering

College of Engineering and Computing

University of South Carolina

2021

Accepted by:

John W. Weidner, Major Professor

Sirivatch Shimpalee, Major Professor

John R. Regalbuto, Committee Member

William E. Mustain, Committee Member

Taylor R. Garrick, Committee Member

Melissa A. Moss, Committee Member

Tracey L. Weldon, Interim Vice Provost and Dean of the Graduate School

ACKNOWLEDGEMENTS

I would first like to thank my advisors, Dr. John W. Weidner and Dr. Sirivatch Shimpalee, for their generous support of my graduate experience as a Ph.D. Candidate at the University of South Carolina. They prepared me for and encouraged me to pursue unique research opportunities within the chemical engineering department as well as General Motors, Savannah River National Laboratory, and the National Renewable Energy Laboratory. I would also like to thank Dr. John R. Regalbuto and Dr. Melissa A. Moss for their support and encouragement in their role on my committee, as well as providing me with the opportunity to gain teaching experience. I appreciate all that Dr. William M. Mustain has done for me, including his role on my committee, his effort to challenge me to always improve, and his willingness to help me think through ideas. I look to thank Dr. Taylor R. Garrick, whose mentorship was key for the development of the work presented in this dissertation and whose friendship helped me through challenges.

Several colleagues at General Motors provided friendship and support, including Miguel Fernandez, Kat Streng, Yiling Dai, Peter Hou, John Moote, and Raghunathan K. I also received much support and made many friends while at the National Renewable Energy Laboratory, including Trevor Harris, Kae Fink, Ryan Brow, Josh Major, Donal Finegan, Ankit Verma, Anudeep Mallarapu, Matt Keyser, and especially my mentor, Shriram Santhanagopalan. Each of these people played a significant role in my growth as a scientist and my growing love for research.

I would like to recognize how fortunate I am to have several colleagues at the University of South Carolina who provide insight, assistance, guidance, and friendship, including Wes Taylor, Ben Ng, Hunter Dean, Hanna Soucie, Travis Omasta, Hailey Boyer, John Weiss, and Ashton Aleman. I would specifically like to thank my lab mates for their continued support: Bahareh Tavakoli, Pongsarun (Boom) Satjaritanun, Cody Wilkins, Mitch Sepe, Kris Likit-Anurak, and Joseph Lopata.

Finally, I'd like to express my deepest gratitude to my friends elsewhere and my family, including my brother, Nic, my sister, Angie, my companion, Tippy the Wonderdog, and especially my parents, John and Mary Lou, for their support, encouragement, trust, and love.

ABSTRACT

As the automotive industry moves towards large format electric vehicles, such as trucks and SUVs, the need for highly efficient, energy-dense electrodes rapidly increases. Several promising active materials have been studied and proposed, however, many of these materials undergo significant volume change upon lithiation and de-lithiation. Cell and pack designers struggle to understand and predict how active material volume change at the particle scale will affect mechano-electrochemical behavior on the electrode, cell, and pack scales. Additionally, many of these active materials suffer in their cycle life due to a mechanically-driven degradation of the electrode matrix. Therefore, the focus of this work is to develop a multi-scale model that accounts for relationships between mechanical and electrochemical phenomena at each scale in the battery system.

The resulting model establishes three novel improvements to the field of mechano-electrochemical battery modeling: (1) A representative volume element model was incorporated into standard battery models to generate realistic predictions of mechanical behavior in the battery cell and pack. (2) Thermodynamically non-ideal, lithiation-based volume change behavior of the active materials was accounted for in the model, leading to higher accuracy in simulations of pressure and cell strain and a stronger understanding of how anode/cathode capacity balance impacts volume change. And (3) a mechano-electrochemical model of a blended electrode was developed, bringing a better

understanding of how active materials preferentially lithiate and the resulting effects on mechano-electrochemical behavior of the cell.

TABLE OF CONTENTS

LIST OF TABLES

LIST OF FIGURES

LIST OF SYMBOLS

Alphabetical

c_i	concentration of the binary electrolyte ($i = n, s,$ or p), mol m^{-3}
c_0	initial electrolyte concentration, mol m^{-3}
$c_{s,i}$	concentration of lithium ion in average solid particle in region i ($i = n$ or p), mol m^{-3}
$c_{s,AM}$	concentration of lithium ion in solid-phase mol m^{-3}
$D_{eff,i}$	effective diffusion coefficient of region i ($i = n, sep,$ or p)
$D_{electrolyte}$	diffusion coefficient of electrolyte
E	Young's Modulus, Pa
$E_{AM}(\tau_{AM})$	lithiation-dependent Young's Modulus of active material
E_i	Young's Modulus for region i ($i = ncc$ or pcc)
$E_{ak,i}$	activation energy for kinetic reaction in electrode i ($i = n, s,$ or p), J mol^{-1}
E_{cell}	cell voltage between anode and cathode current collectors, V
f	Function describing strain response to applied pressure
F	Faraday's constant, 96485 C/mol
j	Average local current density, A/cm^3
J_i	local volumetric current density in electrode i ($i = n$ or p), A m^{-3}
k_i	electrochemical reaction rate constant for electrode i ($i = n$ or p), m s^{-1}
L_i	length in thickness direction of cell on the unit cell scale for region i ($i = ncc, n, s, p,$ or $, pcc$), m
n	electrons transferred in reaction
n_{AM}	electrons transferred in lithiation reaction of active material

$N_{m,i}$	MacMullin Number or region i ($i = n, sep,$ or p)
P	pressure, Pa
Q	Theoretical Capacity
r_i	radial coordinates of average active material particle in electrode i ($i = n$ or p), m
R	universal gas constant, J mol^{-1} K^{-1}
R_{AM}	radius of average active material particle, m
R_e	resistance of the electrolyte phase, Ohm m^2
R_i	radius of average active material particle in region i ($i = n$ or p), m
s_{AM}	stoichiometric coefficient of lithiation reaction of active material
s_i	stoichiometric coefficient of lithiation reaction in region i ($i = n$ or p)
t	Time, s
T	absolute temperature, K
U_{AM}	equilibrium potential of the active material intercalation reaction, V
x	Mass Fraction or spatial coordinate in thickness direction of cell, m
y	Volume fraction
y_{AM}	volume fraction of active material in the electrode

Greek and Special

$\alpha_{a,i}$	anodic transfer coefficient in electrode i ($i = n$ or p)
$\alpha_{c,i}$	cathodic transfer coefficient in electrode i ($i = n$ or p)
β_{AM}	representative parameter or coefficient of active material
$\Delta\hat{V}$	Total molar volume expansion of the active material particle, cm^3/mol
$\Delta\hat{V}_i$	lithiation-based molar volume expansion of active material particle in electrode i ($i = n$ or p), m^3 mol^{-1}

$\Delta\hat{V}_{AM}$	lithiation-based molar volume expansion of active material particle, m^3 mol^{-1}
$\frac{\Delta\hat{V}}{\hat{V}^0}$	Ratio of the total active material volume change to the un-lithiated active material volume
$\left[\frac{\Delta\hat{V}}{\hat{V}^0}\right]_{AM}(\tau_{AM})$	volume of active material divided by the fully delithiated volume of active material as a function of state-of-lithiation of active material
$\left[\frac{\Delta\hat{V}}{\hat{V}^0}\right]_{i}(\tau_i)$	volume of active material divided by the fully delithiated volume of active material as a function of state-of-lithiation of active material in i (i = n, s, or p)
ε	Porosity
ε_i	porosity of region i (i = n, s, or p)
$\varepsilon_{AM,i}$	volume fraction of active material in electrode i (i = n or p)
$\varepsilon_{f,i}$	volume fraction of fillers (binder and conductive carbon) of electrode i (i = n or p)
η_{AM}	overpotential of the active material's intercalation reaction
Γ_2	tortuosity of the liquid phase
θ_i	dimensionless concentration of lithium ions in the intercalation particle of electrode i (i = n or p)
ρ_i	average density of electrode i (i = n or p), kg m^{-3}
$\phi_{1,i}$	solid-phase potential of the active material in region i (i = n or p), V
$\phi_{2,i}$	liquid-phase (electrolyte) potential in region i (i = n or p), V
φ_i	dimensional strain of region i (i = n or p)
$\varphi_{int,i}$	intercalation-based dimensional strain response of electrode i (i = n or p)
$\varphi_{mech,i}$	mechanics-based dimensional strain response of region i (i = n or p)
σ	Stress, Pa
τ	State of charge of the local electrode
τ_{AM}	average state-of-lithiation of active material

τ_i	average state-of-lithiation of electrode i active material ($i = n$ or p)
$\overline{t_n^{Li^+}}$	average time for lithium ion to diffuse across region i ($i = n$ or p)

Subscripts and superscripts

0	Initial
$-$	Anode or internal boundary
$+$	Cathode or external boundary
a	anodic
AM	active material
app	applied
$binder$	electrode binder
c	cathodic
C	Graphitic Carbon
$comp$	Cell component
$cell$	unit cell
$charged$	fully charged cell state
$discharged$	fully discharged cell state
i	denotes region within cell model geometry: ncc, n, s, p, pcc
max	maximum
n	negative electrode region
ncc	negative current collector region
p	positive electrode region
$packing$	foam packaging region
pcc	positive current collector region
s	separator region
Si	Silicon

$surf$	surface
total	unit cell scaled-up to pouch cell

LIST OF ABBREVIATIONS

EV.....Electric Vehicle

ICE ..... Internal Combustion Engine

MSM.....Multi-Scale Model

P2D.....Pseudo Two-Dimensional

RVE.....Representative Volume Element

SPM..... Single Particle Model

CHAPTER 1

INTRODUCTION

A societal push to utilize clean, renewable energy has encouraged the automotive industry to offer electric vehicles (EVs) in their lineups. However, most currently offered EVs are small-the size of a coupe or sedan. In recent years, sales trends of traditional internal combustion engine (ICE) vehicles indicate that consumers are shifting away from smaller vehicles in preference for large-format vehicles, such as crossovers, sport utility vehicles (SUVs), and trucks.(1) Furthermore, transport, labor, technical, and delivery services are hesitant to switch to electric transportation until large-format vehicles, capable of hauling personnel, tools, and goods through a full workday, become available.

Consequently, several automotive manufacturers are pushing to provide fully electric, large-format vehicles. However, the burden of comparison to traditional ICE vehicles results in significant obstacles blocking the road to large-format EV adoption. Presently, manufacturers are continually improving their EVs to more resemble or improve upon ICE vehicles in terms cost, charging (fueling) time, capacity (range) on a single charge (fuel tank), and capacity (range) retention over the lifetime of the vehicle. For large-format vehicles and their applications, a sufficient capacity becomes significantly more difficult to provide. The larger vehicle size and mass reduces efficiency, and thus, range of the vehicle. To maintain a reasonable range, more cells can be added to the automotive battery. However, the large-format vehicles being used for transporting people, tools, or goods will require an additional capacity to account for the higher payloads. For these

reasons, battery designers must work to improve battery capacity while still maintaining or improving battery performance, cost, and safety.

Presently, lithium ion (Li-ion) is considered the premier energy storage chemistry used in batteries for portable electronic devices as well as EVs. These Li-ion batteries consist of six main components: a negative current collector, a negative electrode (anode), a separator, a positive electrode (cathode), a positive current collector, and liquid electrolyte to carry charge through the cell. Electrodes are typically constructed by mixing active material, binder, and a conductive additive into a slurry, which is then calendared onto the current collector. This results in a composite electrode with pores to contain electrolyte. The positive and negative electrodes are kept electrically insulated from each other by the separator, which is also porous to contain electrolyte. This unit cell can then be rolled, folded, or stacked and inserted into a cylindrical, prismatic, or pouch for use in portable electronic applications. These Li-ion batteries generally function as follows. During charge, Li^+ ions diffuse in the solid phase to the surface of the cathode active material, where a de-intercalation reaction occurs. The Li^+ ions then diffuse in the liquid phase (electrolyte), through the separator, towards the surface of the anode active material. The anode intercalation reaction occurs, inserting Li^+ ions into the solid phase of the anode. The stored energy can be released (cell discharge) by completing the electric circuit between the anode and cathode current collectors; this causes a reversal of the charge process.

Battery performance is directly linked to several design parameters and materials. Much of a batteries' rate capability, capacity, and cost is determined by the active materials used in the anode and cathode. The most common anode active material is graphitic carbon

(372 mAh/g).(2-9) Common cathode active materials for EV applications include $LiNi_xMn_yCo_zO_2$ (10)(NMC), $LiNi_xCo_yAl_zO_2$ (11-13)(NCA), $LiCoO_2$ (2, 3)(LCO), and $LiMnO_2$ (14-17)(LMO). Battery designers looking to improve capacity for large format EVs will focus on energy-dense chemistries, like Ni-Rich NMC cathodes. Each of the materials will have their own Li^+ transport and intercalation reaction properties. Other cell design variables, like electrolyte transport properties, electrode and separator porosity, component thickness, and more, will also affect battery performance. As a result, cell designers consider an overwhelming number of variable combinations and are ultimately limited by testing capability. For this reason, cell designers benefit from the ability to predict cell performance based on the changing variables mentioned here.

Several groups began developing this predictive ability in the form of computational models. The first model containing the three main battery components (anode, separator, and cathode) and simulating dual insertion (anode and cathode lithiation) was presented by Fuller.(18) This model operated under the assumption that transport could be modeled in one dimension in the through-plane direction of the battery, accounting for transport in liquid phase using concentrated solution theory. Figure 1.1 illustrates the model's capability to simulate concentration during a galvanostatic discharge. This capability was used to indicate that the major process limiting high-rate cell operation is the increase in concentration overpotential from depletion of the electrolyte. Doyle and Newman(19, 20) continued this investigation by simulating extreme cases, such as no liquid phase diffusion limitations, completely uniform or non-uniform reaction rates, and no solid phase diffusion limitations. Moreover, they illustrated how the model can be used

for parameter optimization as well as deriving analytic expressions for a cell's attainable specific energy and average specific power.

A similar model type has been developed by Zhang(21) that simplifies the transport in the anode and cathode. This model foundation employs the use of a representative single particle with an equivalent surface area as the electrode being studied, and is often called the "single particle model" (SPM).(22) The SPM is often a decent representation of a battery, as the solid phase diffusion and the active material intercalation reaction dictate much of the battery performance. The SPM method simplifies the battery to the point that porosity, electrode dimensions, and liquid phase transport are not accounted for. This results in simulations that are accurate for low-rate operation of batteries with thin electrodes and that require significantly less computation time. For the most accurate battery simulation, researchers combine the transport in the liquid phase and the solid phase.

This model foundation is often called the Newman-type or Pseudo Two Dimension (P2D) model, where the first dimension represents the through-plane direction in the cell and the pseudo-second dimension represents the radial direction of an active material particle. This approach is one of the most commonly employed modeling methods to predict battery performance. Figure 1.2 illustrates an example geometry for the P2D model(23) and Table 1.1 lists examples of the primary governing equations used to describe electrochemical behavior of the battery in the P2D model.(24) Following the path of a Li^+ ion during cell charge: the Li^+ ion will diffuse in the solid phase along the pseudo-second dimension (the radial direction of the cathode active material particle), which is governed by the coupled material balance and charge balance equations for the solid phase.

At the liquid/solid interface, the rate of transfer of Li^+ from solid to liquid phase is governed by the intercalation reaction rate. The reaction rate is ultimately dependent on the overpotential, which accounts for difference in potential between the solid and liquid phase, as well as the equilibrium potential, U_i, of the active material. Then, the Li^+ moves from the cathode, through the separator, to the anode, governed by the coupled mass and charge balance for the liquid phase. The intercalation reaction and solid phase at the anode side will operate under the same governing equations as the cathode, only differing in variable inputs, such as solid phase diffusivity and equilibrium potential. The P2D model foundation is a computationally inexpensive means to solve for concentration and potential in the liquid and solid phases, and therefore, has led to several derivative battery models for the study and optimization of battery design.

Numerous studies have been conducted to investigate the effects of varying cell design and operation. Arora(25) employed the P2D model to examine how cell design parameters, such as electrode thickness, active material loading, and initial electrolyte concentration, affect transport through the cell. They improved agreement between simulation and experimental data by adding an adjustable parameter to represent contact resistance at the current collector/electrode interface. They also realized the diffusion coefficient must be reduced to accurately represent diffusion limitations during high-rate discharge. Doyle(26) continued development of this model type with experimental validation for a graphite/LMO cell, and then illustrated how the model could be used to estimate design parameters as well as material variables, such as the solid phase diffusion coefficient for carbon. Key findings from this work include the minor solid-phase diffusion limitations in the carbon electrode and the notable diffusion limitations during high-rate

operation of the cell, especially with low electrolyte concentrations. These types of models proved great for simulation of the initial cell design, but cells will degrade in performance after several cycles.

To address cell aging, Ning(23) developed a generalized first principles based charge-discharge model to simulate cycle life. Their main development was the incorporation of both an electrochemical parasitic reaction and an increasing film resistance. With this model, they were able to simulate the effect of depth of discharge, end of charge voltage, and overvoltage on cycle life with good agreement. Ramadass(27) expanded upon this, studying the effect of parameters such as end of charge voltage, depth of discharge, film resistance, exchange current density, and overpotential of the parasitic reaction. They improved qualitative accuracy by continually updating parameters after each cycle. They also found that reactions such as electrolyte oxidation and phase transformation, which are active material-specific, can improve model prediction of capacity fade. However, these models did not account for the mechanical degradation in the electrode, which significantly contributes to capacity fade.

To improve understanding of mechanical degradation, several groups developed models to predict stress formation in the battery system. Zhang and Sastry(28) developed a model to simulate intercalation-driven stress in active material particles with spherical or ellipsoidal geometries. Their primary findings show that larger particles will experience higher stresses, but increasing aspect ratio will decrease stress. Park and Sastry(29) further develop this idea by proposing a volume expansion and diffusion model to evaluate stresses due to phase transition. They note that stress levels are closely related to particle geometry, lithium diffusivity, and input current density. They also find that the stress caused by phase

transformation is about an order of magnitude higher than that of just Li^+ intercalation. Ultimately, they connected that lower diffusivity and higher current density induce a larger gradient in Li concentration, which leads to higher stress. These studies illustrated the ability to relate Li concentration gradient to stress for cathode materials used in current generation batteries. However, new active material chemistries are continually being considered.

Several classes of anode active materials have been proposed in recent years. Figure 1.3 illustrates relationship between potential and specific capacity for several material classes of interest.(30) In particular, silicon has received considerable attention as a result of its high theoretical capacity (4200 mAh/g for $Li_{22}Si_5$)(31). However, developers have not yet been able to realize pure Si anodes with sufficient cycle life for commercial use, due in large part to the significant volume change induced by lithium intercalation and deintercalation. During the intercalation process for some high-capacity anode materials, like silicon, the Li forms an alloy. That is, insertion of Li^+ will lead to the breaking of bonds, or changes to the crystalline structure.(32-37) The result is that these alloying materials with high capacity will undergo significant intercalation-driven volume change and structural deformation. Silicon is known to cycle through at least 4 stable alloy phases during a charge/discharge cycle, leading to a complete transformation in the crystal structure and a ~400% volume expansion between the fully charged and fully discharged states.(38, 39) The coupled high crystallographic strain and large volume change leads to Si fracturing and pulverization, which detaches Si from the electrode during discharge, rapidly decreasing capacity and electrical contact.(40) In fact, metallurgical silicon loses nearly all of its capacity after only ~10 cycles.

Golmon(41) focused on relating single particle stress, determined from diffusion and surface kinetics, to mechanical fracturing, using silicon as the representative material. They showed that the stressed caused by intercalation can be above the tensile failure stress of silicon depending on the particle size and discharge rate. Similarly, Cheng(42) related the same intercalation-induced stress to particle fracture based on the active material tensile strength. They found that the stress and strain energy can evolve differently under electrolytic and galvanostatic control and suggest that charging strategies may be used to mitigate degradation. However, the stress and strain behavior of materials like silicon are so significant that other factors must be considered.

Significant active material volume change will also impact mechanical behavior at the electrode and cell scales. Stress generated in the anode will in turn cause stress and dimensional changes throughout the rest of the cell. In EVs, pouch cells contained in the battery pack will undergo dimensional changes caused by the active material volume change. Some battery packs have modules that contain cooling fins, thermistors, foam separators, and repeating frame elements to hold the cells, maintain temperature, and manage the volume change.(43) Additionally, each module is connected to adjacent modules with bus bars and structural bars. As the cells expand and contract during cycling, the stresses generated can cause the materials in the module to deform or crack, resulting in a loss of electrical contact, decreasing range, or a loss of heat transfer fluid, which results in a loss of effective cooling. The pressures that generate inside the pack can contribute to decreased electrode porosity, increasing ionic transport resistance the cell(44), as well as contribute to the pulverization and detachment of the active material inside the electrode matrix, reducing capacity.(45) For these reasons, it is necessary to account for the complex

linkages between mechanical and electrochemical phenomena in the pouch cell environment when trying to design new cells, especially for those containing active materials with a high intercalation-driven volume change.

Battery designers hoping to comprehensively consider promising future cell chemistries, like silicon, would benefit considerably from a method to accurately predict the coupled, mechano-electrochemical phenomena at the material, electrode, cell, and pack scales. Because of experimental limitations in simultaneous observation of each scale, a multi-scale modeling (MSM) approach shows promise to comprehensively account for mechano-electrochemical behavior and fill the gap in knowledge.

Initial efforts of MSM approaches focused on systems of interest with low volume change. Christensen and Newman(32) developed a model to account for stresses generated in spherical particles for active materials with low volume change upon Li^+ intercalation. However, this model and similar models(46) would operate under the assumption that active material volume change would not significantly impact the porosity in the cell. For the low volume change materials considered in these studies, this assumption is valid. As energy-dense active materials with high volume change, such as silicon, are considered, the changes to electrode porosity and dimensions increase significantly.

Both porosity and electrode dimensions have an impact on liquid phase diffusion, mentioned previously to be an important factor in cell performance. Therefore, some studies have focused on accounting for the impact of active material volume change on electrode geometry. Jain(47) modified the material balance equation to account for changing volume in a one-dimensional model. From there, the model was extended to improve studies on design and parameter estimation.(48) These studies showed

improvements to parameter estimation and prediction of capacity, however, they assumed porosity to remain constant and that volume change would only cause dimensional changes of the electrode. Conversely, Chandrasekaran developed a model(49, 50) for lithium-silicon electrodes that accounts for volume change with changes to porosity, and not dimensional changes of the electrode. This study revealed that the porosity can limit transport during high-rate operation. Accounting for dimensional changes and accounting for porosity changes represent the two extreme cases on the impact of volume change in electrode geometry. These two extremes are represented in Figure 1.4a and 1.4b as an electrode with a perfectly rigid casing (i.e., all volume change goes into a change in electrode porosity) and an electrode with a completely compliant casing (i.e., all volume change goes into a change in electrode dimensions), respectively.

It is theorized that active material volume change in an electrode would likely cause changes to both electrode dimensions and electrode porosity, as illustrated in Figure 1.4c. Gomadam and Weidner(51) addressed this through the development of a three dimensional electrode model. To do this, a material balance was developed that accounts for porosity changes, dimensional changes, and reaction products. It wasn't clear how active material volume change contributed to either dimensional or porosity change. Therefore, a parameter called the swelling coefficient was introduced to account for the relative change to porosity and electrode dimensions. The swelling coefficient required experimental measurement or had to be predicted a priori.

Garrick and Weidner(52-54) continued development of this model by coupling the stress in the entire battery system to the material balances in the electrode. To do this, they employed porous rock mechanics to describe the compressive response of the electrode.

Their volume change model indicated the significant effect of a cell casing's compressibility on porosity and dimensional changes of the electrode. Moreover, they showed how formation of non-uniform reaction distributions will impact changes in porosity during high-rate operation. Their work resulted in a strong multi-scale modeling foundation for studies linking mechanical and electrochemical phenomena at the particle, electrode, and cell scales.

Some groups have since proposed similar MSM models to investigate varying topics. Mai(55) reformulated the battery model to couple large mechano-electrochemical deformations at the particle and electrode levels. Ai(56) coupled particle-scale mechanical physics into a P2D model, which allowed them to model stress inhomogeneity in Li-ion pouch cells, similar to cathode-focused work of Dai(57). Their work indicated the experimental phenomenon of electrode particle fragmentation occurring towards the separator. While each of these studies produced novel insight to coupled mechano-electrochemical phenomena, there is still a deep need for a comprehensive understanding of the coupled mechano-electrochemical phenomena at every scale in the battery, especially for the cell designers considering promising chemistries with large volume change.

The focus of this dissertation is to understand the link between fundamental mechanical and electrochemical behavior at each scale through the development of a practical mechano-electrochemical MSM. This was completed by (1) accurately representing the cell mechanics during operation through the implementation of a representative volume element (RVE) model into a standard P2D model, (2) accounting for the relationship between intercalation-based phase changes and volume change by

incorporating thermodynamically non-ideal, lithiation-based volume change behavior of the active material, and (3) developing a blended electrode model to accurately simulate how multiple active materials within the same electrode will preferentially lithiate, and how that preferential lithiation impacts volume change phenomena.

1.2 TABLES AND FIGURES

Table 1.1. Examples of the governing equations used in a P2D model.(24)

Description	**Governing Equation**
Material Balance in the Liquid Phase	$\varepsilon_i \frac{\partial c_i}{\partial t} = \frac{\partial}{\partial x}\left(D_{eff,i} \frac{\partial c_i}{\partial x}\right) + (1 - t_+^0) a_i J_i$
Material Balance in the Solid Phase	$\frac{\partial c_{s,i}}{\partial t} = D_{s,i} \frac{1}{r_i^2} \frac{\partial}{\partial r_i}\left(r_i^2 \frac{\partial c_{s,i}}{\partial r_i}\right)$
Charge Balance in the Liquid Phase	$-\frac{\partial}{\partial x}\left(\kappa_{eff,i} \frac{\partial \phi_{2,i}}{\partial x}\right) + \frac{2RT(1 - t_+^0)}{F} \frac{\partial}{\partial x}\left(\kappa_{eff,i} \frac{\partial (\ln c_i)}{\partial x}\right) = a_i F J_i$
Charge Balance in the Solid Phase	$-\sigma_{eff,i} \frac{\partial^2 \phi_{1,i}}{\partial x^2} = a_i F J_i$
Intercalation Reaction Rate	$j_i = i_0 \left[exp\left(\frac{\alpha_{a,i} n_i F}{RT} \eta_i\right) - exp\left(-\frac{\alpha_{c,i} n_i F}{RT} \eta_i\right)\right]$
Overpotential	$\eta_i = \phi_{1,i} - \phi_{2,i} - U_i$

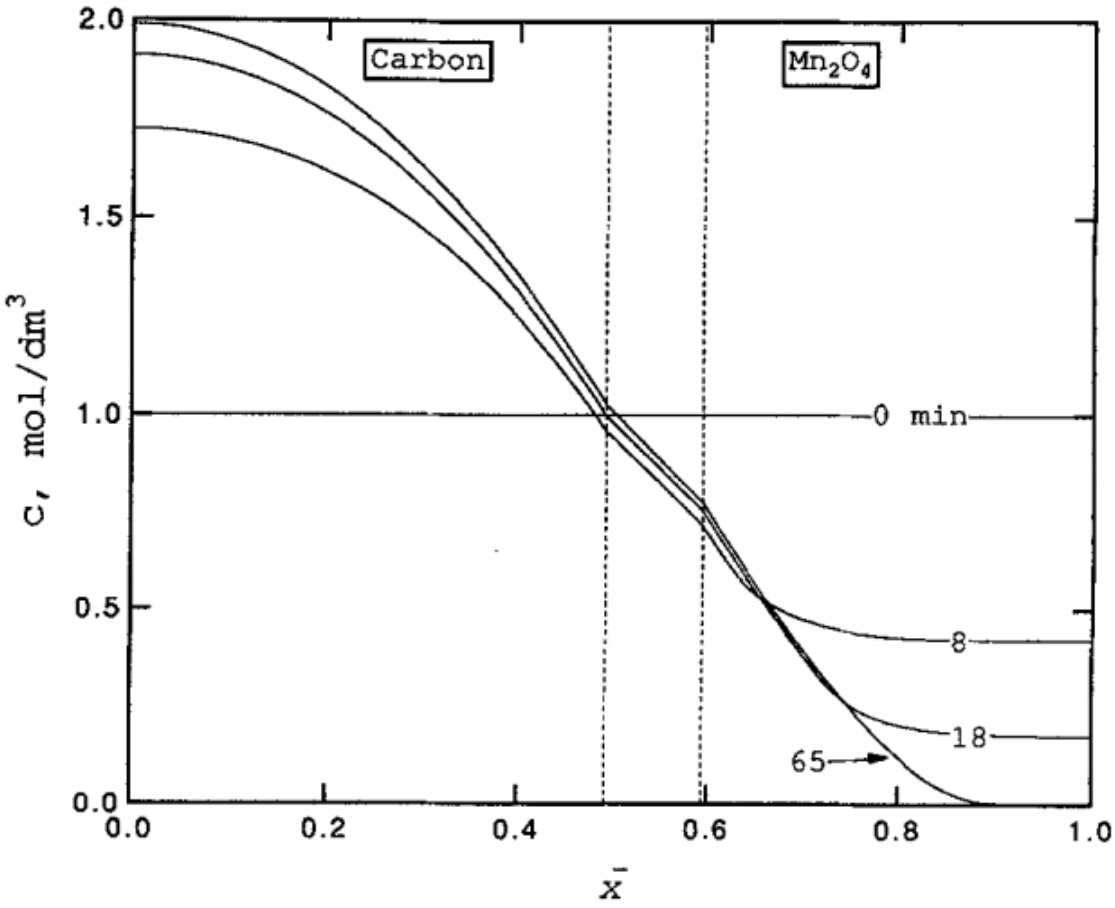

Figure 1.1. Concentration profiles across the cell containing a carbon anode and an LMO cathode during galvanostatic discharge at I=4.0 mA/cm^2. The separator region is set off by the dashed lines.(18)

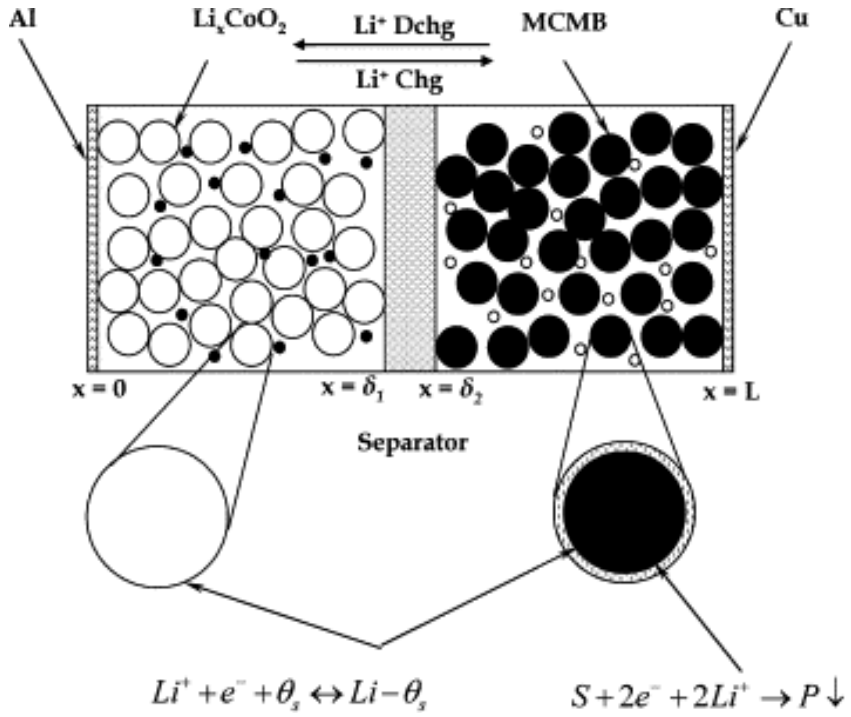

Figure 1.2. Example of the Pseudo Two-Dimensional geometry.(23)

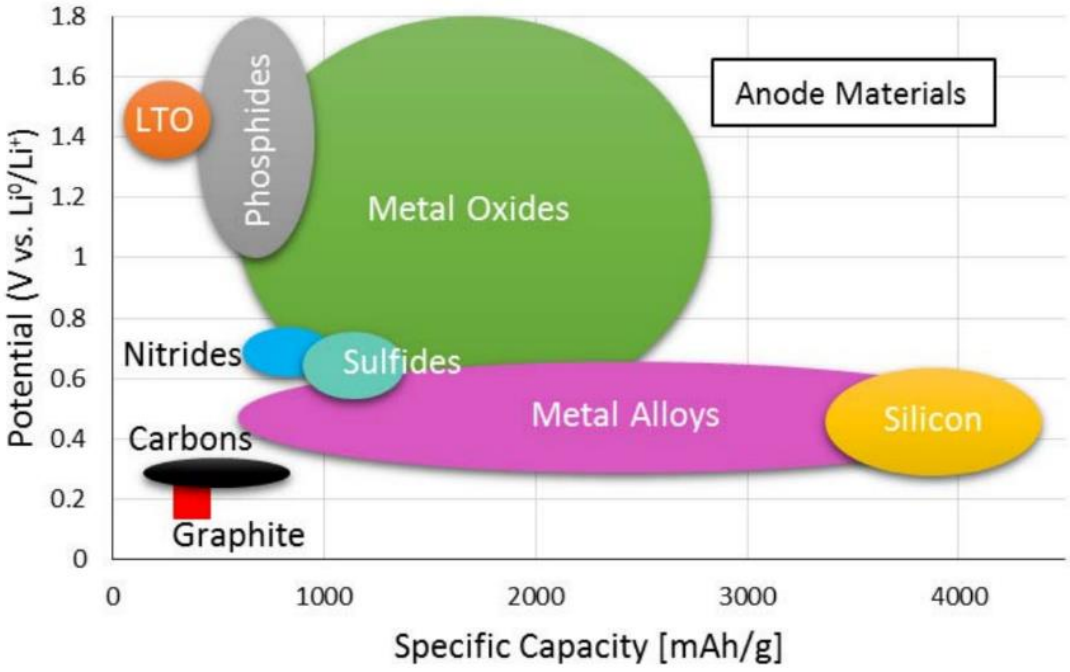

Figure 1.3. Specific capacity of varying anode active materials.(30)

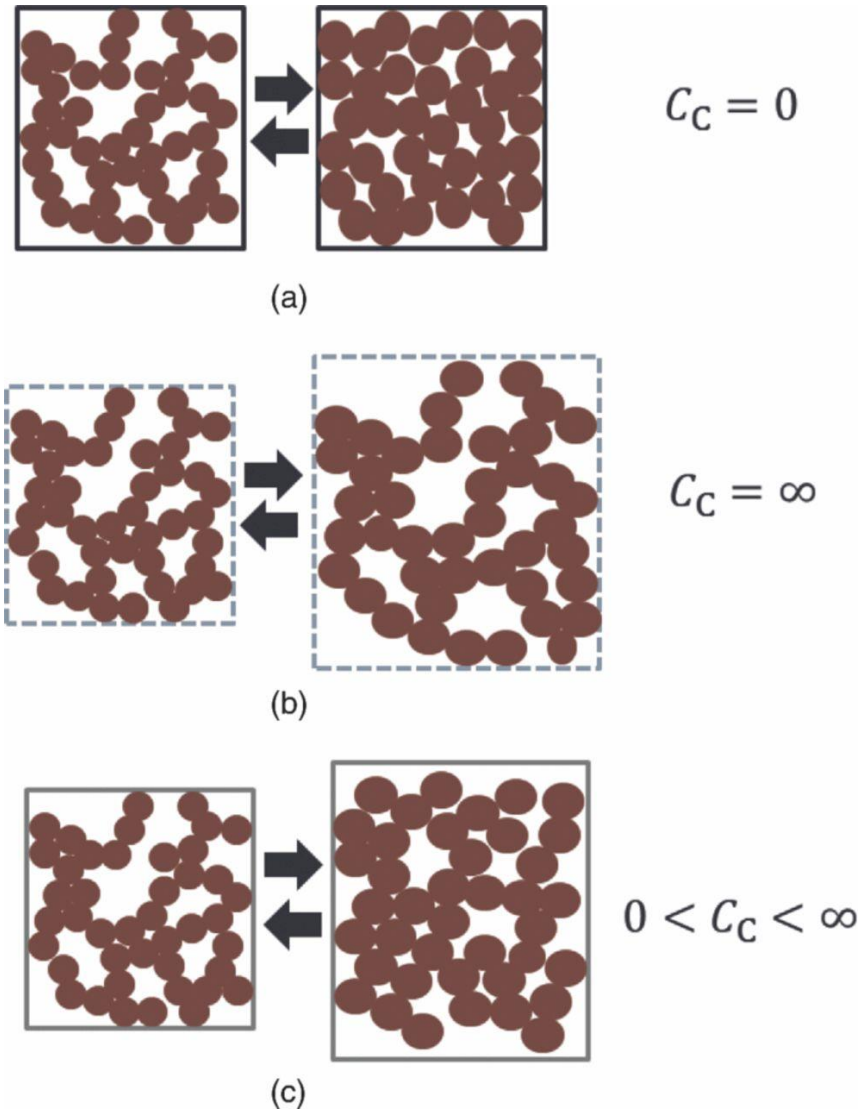

Figure 1.4. Depiction of an electrode with (a) a completely rigid volume, (b) a completely compliant volume, and (c) a more partial volume compliance resembling a real-world electrode.

CHAPTER 2

THE EFFECT OF VOLUME CHANGE ON THE ACCESSIBLE CAPACITIES OF POROUS SILICON-GRAPHITE COMPOSITE ANODES

This chapter focuses on the development and implementation of a representative volume element model to accurately simulate mechano-electrochemical behavior in pouch cells containing composite silicon-graphite anodes. Some results from this work were presented at the Meeting of the Electrochemical Society in Dallas, Texas, May 2019.(58) This work has also been published(59) in the Journal of the Electrochemical Society in April 2019.

The desire to realize large scale and cost-effective electric vehicle (EV) commercialization has caused several classes of anode active materials to be proposed in recent years, and silicon has received considerable attention as a result of its high theoretical capacity (4200 mAh/g for $Li_{22}Si_5$).(31) However, developers have not yet been able to realize pure Si anodes with sufficient cycle life for commercial use, due in part to the large volume change that occurs during lithium intercalation. Silicon cycles through at least 4 stable alloy phases during a charging and discharging cycle, leading to a complete transformation in the crystal structure and a ~400% volume expansion between the fully charged and fully discharged states.(38, 60) The coupled high crystallographic strain and large volume change leads to Si fracturing and pulverization, which detaches Si from the

electrode during discharge, rapidly decreasing capacity and electrical contact.(40) In fact, metallurgical silicon loses nearly all of its capacity after only ~10 cycles. To mitigate structural strain, and thus, reduce capacity loss with cycling, researchers are using silicon/graphite (Si/C) composites to incorporate the energy dense silicon active material without excessive expansion.(61, 62) However, it is still poorly understood how stresses develop in the porous structure during cycling, and how materials, electrodes, cells, and ultimately battery packs can be rationally designed to mitigate the effects of volume change inherent in these silicon-based chemistries. Therefore, we have developed a model that links electrochemical and mechanical phenomena of the individual components up through the cell level to aid in the rational design of commercially acceptable Li-Si/C batteries and packs. In consideration of Si/C composite chemistries, Dash and Pannala recently modeled the theoretical capacities of anodes with varying Si/C composite ratios.(63) However, their study assumed that the volume of the anode layer is fixed and that the active material volume change would only affect the porosity of the composite electrode. They predicted capacities by allowing the active material to expand completely into the void fraction of the fixed anode volume, resulting in zero porosity at full lithiation of the active material. That is, they assumed all the volume change went into porosity changes and ignored stresses that build up in the cell. However, our group previously developed a model that predicted the split between electrode porosity and dimensional changes upon lithiation.(52-54) Stresses that build up in the cell during lithiation cause the electrode layer to expand rather than only filling the void volume. Coupling mechanical and electrochemical properties of the cell is necessary to accurately predict both capacity as a function of the Si/C ratio and the conditions where safety limits may be exceeded. In this study, we employ

our coupled electrochemical and mechanical model to determine the accessible capacities of varying Si/C composite electrodes based on practical design limitations, cell face pressure and electrode porosity. Most current production EVs contain the cells in a battery pack or module to maintain electrical conductivity and provide efficient cooling. Typical modules contain cooling fins, thermistors, foam separators, and repeating frame elements to hold the cells.(43) Each module is connected to an adjacent module with bus bars and structural bars. As the cells expand and contract during cycling, the stresses generated can cause the materials in the battery module to deform and crack, resulting in a loss of electrical contact and therefore, decreased range, or a loss of heat transfer fluid, which could result in a loss of effective cooling and induce thermal runaway. This cell face pressure also has an effect inside the cell, leading to decreased porosity, meaning higher ionic diffusion resistance across the electrode thickness; as well as the pulverization and detachment of the active material from the porous electrode matrix, reducing capacity.(45) In order to accurately predict pressure and porosity to aid in practical cell design, we incorporated mechanical behavior of the individual components of the cell as well as the cell packing itself into our previously developed model. Recently, Zhang et al. conducted mechanical tests to evaluate the constitutive properties of porous electrodes, for both anode and cathode.(64) Zhang's experimental work gave insight into the mechanical behavior of the fully formed electrode as opposed to the mechanical behavior of the individual materials in the electrode. Using Zhang's experimental results as an input to our model allowed us to mimic realistic mechanical behavior for the anode and cathode. Likewise, we incorporated component level mechanical behavior for the separator(65) and a generic polyurethane packing material(66) into our model to produce an accurate representation of

mechanical behavior in a full battery pack. The incorporation of these realistic component mechanical behaviors allowed us to develop practical dimensional predictions in our model.

2.1 MODEL SETUP

During charging, Li+ ions move from the cathode to the Si/C composite anode resulting in an expansion of the active material. For this study, we assumed low-rate charging of the anode to focus on maximizing volumetric and gravimetric energy density in order to aid in selection of silicon composites. Performance studies that incorporate high-rate charging and discharging of cells with silicon composite anodes will be the focus of future work. As shown previously by Garrick and Weidner,(52-54) the volume change of the anode is based on the material balance governing equation shown below:

$$\frac{\partial(1-\varepsilon)}{\partial t} + (1-\varepsilon)\frac{\partial \varphi}{\partial t} = -\frac{s\Delta\hat{V}}{nF} j \qquad [2.1]$$

The right side of the equal sign represents the volume change due to the intercalation of lithium into the anode active material, which then either affects the electrode layer dimensional changes (second term on the left) or porosity changes (first term on the left). The average volumetric current density, j, and the anode porosity and strain, ε and φ, respectively, are the variables linking electrochemical behavior to mechanical behavior. The equations governing j and all relevant electrochemical initial conditions and boundary conditions have been taken from previous works.(18, 24, 26, 67) Before we can properly couple mechanical and electrochemical behavior, we must accurately represent the mechanical behavior of the cell and each of its components. Each cell component will exhibit a different strain response to a given pressure, and the total cell face pressure is generated based on the relative compliance and thickness of each

component. Therefore, the individual component thicknesses and their respective stress-strain responses must be incorporated in our calculations. Our previous model incorporated porous rock mechanics to describe the strain response from an applied stress for our electrode component.8 Here, we utilize a cubic spline interpolation function, f_{comp}, to describe the strain response for each porous component: the anode, cathode, separator, and foam packing. The stress-strain response of most porous materials can be described as a second or third order polynomial when considering the pressure ranges applicable to an EV battery pack during normal operation. Therefore, the cubic spline interpolation would produce a more accurate representation of the material behavior than a linear interpolation. These interpolation functions, built from experimentally measured mechanical responses, provide a realistic mechanical behavior input for each porous component. In this simulation, the porous anode and cathode have two phenomena that contribute to their overall strain. The first is the electrode compression from an externally applied pressure. This is described as the previously mentioned anode or cathode interpolation function, f_{-} or f_{+}, respectively. The second phenomenon is the electrode expansion caused by the active material volume expansion upon lithium intercalation, φ_i. Because we assume a constant low charge rate, we can correlate current density to average state of charge of the electrodes, $\tau_{\pm}$. We also assume that the volume change is linearly dependent on state of charge and that the individual active materials in the anode composite lithiate at approximately the same rate. Therefore, we use the following governing equation to predict the active material volume change's contribution to the overall strain response for the electrodes.

$$\varphi_{i,\pm} = \left[\frac{\Delta\widehat{V}}{\widehat{V}^0}\right]_{\pm} \tau_{\pm} \qquad [2.2]$$

$\left[\frac{\Delta\hat{V}}{\hat{V}^0}\right]_{\pm}$ is the ratio of the total active material volume change to the unlithiated active material volume. For the composite anode, $\left[\frac{\Delta\hat{V}}{\hat{V}^0}\right]_{-}$ is calculated as the sum of the individual active material molar volume expansion ratios multiplied by their respective volume fractions.

$$\left[\frac{\Delta\hat{V}}{\hat{V}^0}\right]_{-} = \left[\frac{\Delta\hat{V}}{\hat{V}^0}\right]_{C} y_C + \left[\frac{\Delta\hat{V}}{\hat{V}^0}\right]_{Si} y_{Si} \quad [2.3]$$

Combining the two strain phenomena produces the overall electrode strain response in an operating cell. This equation can then be incorporated for both anode and cathode mechanics.

$$\varphi_{\pm} = \left(\varphi_{m,\pm} + \varphi_{i,\pm}\right) = -f_{\pm}(\sigma) + \left[\frac{\Delta\hat{V}}{\hat{V}^0}\right]_{\pm} \tau_{\pm} \quad [2.4]$$

The strain for the anode and cathode current collectors is assumed to follow linear elastic mechanics:

$$\varphi = \frac{\sigma}{E} \quad [2.5]$$

The Young's Moduli, E, used for the copper anode current collector and aluminum cathode current collectors are significantly high. These high Young's Moduli values rendered the current collectors virtually incompressible compared to the other components at the low pressure windows needed for practical cell operation. In summary of our model, we assume that each component will experience the same stress, known as the cell face pressure. This pressure variable, along with each component's strain response, which is described by an interpolation, Eq. 2.4, or Eq. 2.5, is what links each individual component strain. Then, as the active materials expand and contract upon cell operation, described by Eq. 2.1, changes in electrode dimensions, pressure, and porosity will occur. These changes are fully detailed in our previous work.(52-54, 68) The degree to which the anode active

material will expand is determined by the Si/C ratio and Eq. 2.3; as more silicon is incorporated into the active material, the total anode volume expansion will increase. Additionally, the individual component strain responses and thicknesses can be used to determine the overall cell displacement, or cell strain, as a function of cell pressure.

2.2 RESULTS AND DISCUSSION

We produced a simulation to represent pouch cells with foam packing, as would be seen in an EV battery pack. The simulation incorporates the mechanics of all internal cell components as well as the packing itself. This enables us to observe the effect that packing will have on pressure generation in the cell as well as the overall cell strain during operation. Figure 2.1 shows the cell geometry considered in our model. The cross-sectional area of each cell component is considered to be uniform with negligible end effects, therefore we solved our model in 1D across the x-axis. Initial component thicknesses reflect the thicknesses seen in current-production large format pouch cells with the foam packing thickness being 30% of the total cell thickness. The initial cell face pressure is 0 kPa, meaning each component's initial thickness is unaffected by a compressive strain response. Either end of the geometry is held in a fixed position meaning the total geometry length, including packing, is held constant. COMSOL Multiphysics was used to run our simulation using a Time Dependent solver that was set to run through a full charging of a balanced cell from 2.5 to 3.2 V, representing a 0 and 1 state of charge of the cell, respectively. The physics of the cell were simulated numerically, using the Partial Differential Equation interface. This model is solved in one dimension along the thickness direction of the cell, with respect to voltage, electrolyte concentration, strain, reaction rate, and porosity; where uniformity was assumed in the other two dimensions. Lithium

concentration in the solid phase was solved using a pseudo two dimensional (P2D) method,(18) where one dimension is the length of the cell along the x-axis and the pseudo second dimension was solved along the radius of a theoretical active material particle. The electrochemical governing equations are connected to the mechanical governing equations through the electrodes linked by dependent variables: porosity, stress, and state of charge. When considering an expanding active material, the pressure generation and decrease in porosity are two major design limitations that need to be considered when comparing to a traditional graphite anode. Therefore, we observed the effects of varying the Si/C ratio and the initial anode composite porosity. The anode used here contained 5% binder and an initial porosity of 0.37. This initial porosity was chosen based on a previous study,(64) however, the model is versatile and can incorporate lower or higher initial porosities if desired. The overall volume change ratio was calculated with Eq. 2.3, using experimentally measured molar volume expansions for silicon and graphite from literature, 280% and 10%, respectively.(35, 69, 70) The composite anode was assumed to be a fully mixed composite with no variations in local electrode composition. It was also assumed that the Si and C lithiate at approximately the same rate. We used a 3% expansion volume ratio for an NMC cathode.(71) We chose design limitations for both pressure and porosity based on EV pack design limitations. Pressure limitations, 250 kPa and 500 kPa, are chosen to represent pressures where the module or pack may see cracking, or pressures where cells may be at risk of shorting if any dendrite growth or lithium plating is seen. Porosity limitation, 0.25, was chosen to represent power cells that may require a minimum porosity requirement to avoid ionic diffusion resistances, whereas energy cells that sees low charge/discharge rates could still operate properly at a lower porosities. For the mechanical

properties of the anode and cathode, realistic stress-strain curves were obtained from Zhang's previous study.(72) Likewise, we incorporated separator data(65) and selected a generic polyurethane foam,(66) to represent the packing region for this study because a softer material is needed to account for the large volume change of a Si/C composite anode. Each of these components' stress-strain interpolation functions were assigned to their individual component domains within the model geometry in COMSOL. The copper anode and aluminum cathode current collectors followed linear elastic mechanics, Equation 2.5, using Young's Moduli of 110 GPa and 70 GPa, respectively.(73)

Simulating pressure generation.—Initially, we simulated a full charge of a cell containing a composite anode with silicon percentages from 0% to 25% to highlight the increase in pressure generation within the cell. Figure 2.2a shows the resulting pressures generated as a function of anode state of charge for composite anodes with varying percentages of silicon in a cell with foam packing. The pressure increases as a function of state of charge, similar to the results seen in earlier studies that consider single electrodes.(54) Here, we illustrate how increasing the silicon composition in the anode results in differing rates of pressure generation due to the change in active material volumetric expansion. Even the predictions with 0% silicon show moderate pressure generation over a charge due to the assumed 10% expansion of graphite. Figure 2.2b shows the same simulation if the total cell volume was fixed (i.e., the foam packing volume would be rigid and hold the cell volume constant). This second simulation's purpose is to show the importance of including packing mechanical behavior in a coupled mechanical and electrochemical simulation. When we assume a fixed anode volume as in Figure 2.2b, we only see an exponential increase in the pressure, which is representative of the sum of the

components inside the cell. When considering 0% silicon, or a pure graphite anode, for fixed cell and foam-packed cell, we have pressures of 392.3 kPa and 89.1 kPa at the end of a full charge, respectively. These details indicate that even for anodes with less significant expansion, in this case, graphite with 10% expansion, we still observe the significant impact that the foam packing mechanical response has on the prediction of the full cell mechanics, and why most battery packs containing pouch cells with graphite anodes have foam to contain the cell expansion. As seen here, if a fixed cell volume is assumed, the pure graphite anode would not meet a 250 kPa pressure design limitation after a full charge. Hence, prismatic battery designers will leave space within the rigid casing to allow for cell material expansion. Additionally, from Figure 2.2a, the pressure generation follows a unique profile which includes an initial linear increase in pressure, a plateau, and then exponential increase. This profile aligns with the stress-strain of our generic foam packing, which is the most compliant component of our simulation geometry.

Accessible capacities based on pressure.—Dash and Pannala's study indicates that increasing silicon percentage in the composite anode will only lead to an increase in gravimetric capacity.(63) This is because their gravimetric capacity calculations are unaffected by the increasing initial porosity required to allow the active material to fully expand into the void space. Whereas, volumetric capacity will increase until a "threshold value", or the silicon percentage to maximize volumetric capacity. This threshold value is found where the increasing capacity from adding silicon meets the decreasing capacity from increasing initial porosity. We built upon their concept for calculating threshold values by two means: first, we account for the impact that mechanical limitations will have on the anode, second, we consider that we need to maintain a porosity large enough to

avoid significant ionic resistances instead of letting the active material completely expand into the void space. To determine the accessible anode capacities, we must determine the anode's operational state of charge, τ, range where the pressure limitations are avoided. In effect, the state of charge at which the pressure meets the design limitation would be the selected cutoff point. The horizontal lines in Figure 2.2 illustrate where the state of charge cutoff points would be for a pressure limitation of 250 kPa and 500 kPa. The state of charge cutoff can then be used to determine the accessible capacity. The accessible capacity is calculated by multiplying the state of charge cutoff value with the theoretical capacity of the anode active materials. Theoretical capacity, Q_- , is the sum of theoretical capacity for Si and C multiplied by their respective compositions in the composite anode.

$$Q_- = Q_C x_C + Q_{Si} x_{Si} \quad [2.6]$$

With the determination of the accessible capacity, we can then convert between gravimetric or volumetric capacities. Gravimetric capacity is accessible capacity divided by the total mass of the anode materials (including binder) and volumetric capacity is dividing the accessible capacity by the total anode volume at a τ value of 0. Figure 2.3 shows the resulting accessible gravimetric and volumetric capacities as a function of silicon percentages for the simulation including foam packing. From Figure 2.3, we see a linear increase in anode capacity with increasing percent silicon. This trend follows Eq. 2.6, which is the calculation of theoretical capacity unaffected by the pressure cutoff. Then, at a certain silicon composition, we observe a non-linear decrease in anode capacity, caused by the pressure cutoff limitation occurring at decreasing τ with increasing silicon composition. Using our simulation of a cell with foam packing, we determined the threshold capacity to be 461 mAh/g at 5% silicon and 689 mAh/g at 13.5% silicon for the

250 kPa and 500 kPa limitations, respectively. For this given cell geometry and chemical design, these would represent the ideal silicon percentages to use without generating damaging pressures. However, this model is also able to tune chemistries, component thicknesses, and packing thicknesses. Therefore, the model can act as a tool for engineers designing cells, choosing foam packing, and determining pack structure requirements.

Simulating porosity change.—As previously mentioned, another mechanical design limitation is electrode porosity. There are minimum porosities required to avoid significant ionic resistance in the electrolyte, and these ideal design porosities would vary depending on the function of the cell; high power cells would require a higher porosity due to the need for significant diffusion of ions through the electrolyte. On the other hand, energy cells see lower C-rates, meaning ionic transport resistance in the electrolyte is not as significant of a contributor to voltage losses; therefore, these cells can tolerate sacrificing more porosity to increase capacity. To observe how the porosity requirement may affect other design aspects, we observe four silicon percentages from our simulation of a cell with foam packing: 0%, 5% (optimal Si percent for 250 kPa), 13.5% (optimal Si percent for 500 kPa), and 25% (the maximum silicon composition simulated). Then, porosity as a function of state of charge was simulated while varying initial porosity of the anode from 0.25 to 0.3. Figure 2.4 shows the resulting plot from the 25% silicon composition. As expected, in Figure 2.4 the porosity initially decreases due to the expanding active material in the anode, and because silicon expands more than graphite, we see a large porosity change as a function of state of charge with a high silicon composition in the active material. However, near a state of charge of 0.3, we observe a slight increase in porosity until a state of charge of about 0.45. This is another indication of the foam's mechanical behavior. With a 25%

silicon composition, the anode active material expansion generates pressures linearly until the pressures reach the foam's "plateau" region in its stress-strain response. The "plateau" represents a region of high strain-rate, in other words, large increases in strain, or material expansion, generate much less pressure as the foam is extremely compliant in this region. This means that in the high strain-rate region, the dimensional growth contribution in Eq. 2.1, or the second term on the left side of the equal sign, will be favored heavily because of the relatively constant cell face pressure, and therefore the porosity will increase. After a porosity of 0.45, we see the porosity exponentially decrease as pressures quickly develop after the high strain-rate region.

Accessible capacities based on porosity.—Similar to the pressure design limitation analysis, we assigned a 0.25 porosity cutoff to represent either power or energy cell design requirements. As we did in the pressure study, we can calculate accessible capacities using Eq. 2.6 and the porosity cutoff condition. Figure 2.5 shows the resulting volumetric capacities as a function of state of charge for each silicon percentage, 0%, 5%, 13.5%, and 25% Si. This concept is similar to how Dash and Pannala adjusted initial porosity to allow the active material to completely fill the void space;7 where instead, we built upon their concept and assigned a minimum porosity for practical applications. As seen in Figure 2.5, as initial porosity increases, we see the accessible capacity increase; this is due to the initial porosity moving further away from the porosity cutoff, meaning the anode can achieve a higher τ before hitting the porosity cutoff limitation due to active material expansion during charging. However, after a certain initial porosity, volumetric capacity linearly decreases. This decrease is caused by the loss of initial anode active material with increasing initial porosity. From the circles in Figure 2.5, we can see that the max accessible capacity of the

composite anode occurs exactly where the anode porosity cutoff no longer affects the capacity calculations. Again, we observed the impact that the stress-strain response of the foam has on the results when considering the circled values in Figure 2.5. The max accessible capacities for 5% and 13.5% silicon occur at nearly the same initial anode porosity. This is caused by both values taking place in the high strain-rate "plateau" region, where porosity remains almost constant. However, the max capacity for the anode with 25% silicon occurs at an initial anode porosity significantly higher because it lies within the region with an exponential increase in pressure. Indicated here, by using a numerical solving method, the optimal initial porosity and silicon composition can be determined based on common mechanical design specifications by using measured mechanical properties of the individual components and component materials. For this simulation, we found that for conservative cutoff values of 250 kPa and 0.25 for pressure and porosity, respectively, we can see a ∼59% increase in accessible capacity by using a 5% Si/C composite instead of a traditional graphite anode.

Component strain prediction.—In addition to pressure and porosity limitations, practical cell and pack design will require a total strain limitation of the cell or its individual components. Because the anode active material expansion is linked to the mechanical behavior of all cell components, we can observe the component strain (compression/expansion) as a function of state of charge. Figure 2.6 illustrates this concept for a 5% silicon Si/C composite with a generic foam packing. As can be seen in Figure 2.6, as the cell charges, the anode expands and in turn compresses the other internal components. The most significant compressive strain is seen with the cathode, caused by the pressure generation and the de-lithiation of the cathode active material. The packing

compresses to accommodate for the overall cell expansion, so the displacement of the anode does not directly correlate to the compression of the cathode and separator. For a more rigid foam packing, we would see similar component displacements without much cell or packing displacement. From this simulation, we can translate anode and cathode expansion and contraction to separator displacement. In this case the separator is being displaced by nearly 17 microns, which is over half of a typical separator thickness. The repeated displacement of the separator can lead to the wearing of the edges of the separator, a critical safety factor for lifetime cell usage. The ability to model anode porosity, pressure in the cell, and strain of cell and individual cell components is imperative for practical pack design. The simulations here show realistic mechanical behavior of the battery and its components which can be used to optimize the design of battery systems using Si/C composite chemistries. In the future, the model can be experimentally validated and applied to cell and battery pack design.

2.3 CONCLUSIONS

The objective here was to determine the accessible capacities of varying Si/C composite ratios while appropriately accounting for the volume change of the electrode active materials. This was achieved by using a battery model that couples electrochemical and mechanical phenomena and incorporating realistic mechanical behavior for each cell component. We emulated realistic mechanics by linking experimentally measured mechanical behavior for each component. Then, we simulated a full charge of a pouch cell within a generic foam packing for anodes with varying Si/C ratios. Our simulations allowed us to predict mechanical changes (i.e., porosity, strain, and pressure) that occurred while charging. Then, the accessible capacities were determined based on realistic design

limitations, cell face pressure and anode porosity. This study revealed that, when incorporating the full cell and packing in mechanical predictions, there are possibilities to incorporate more silicon in the composite anodes used in automotive battery pack applications. Throughout this study, we observed the extremely significant effect that packing material has on the mechanical predictions in the cell. For this particular model study of Si/C composites, using conservative 250 kPa pressure and 0.25 porosity cutoffs, we found that an appropriate balance of initial anode porosity and silicon percentage in the anode active material could lead to anodes with ~59% more capacity than traditional graphite anodes. This modeling process could be used to predict and account for anode composite volume change for cell and pack design applications. Additionally, this model can be tuned to simulate and optimize other features of the cell, such as cell component thicknesses, different electrode/electrolyte chemistries, and different packing thicknesses/materials.

2.4 FIGURES

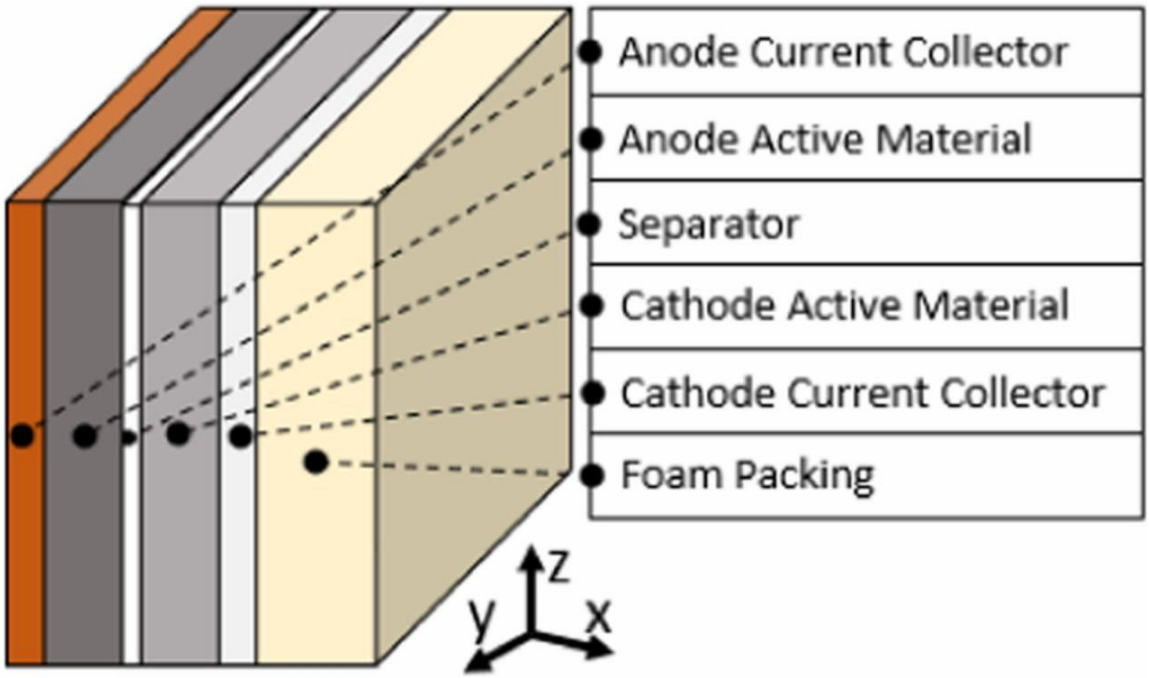

Figure 2.1. The cell geometry considered in model development.

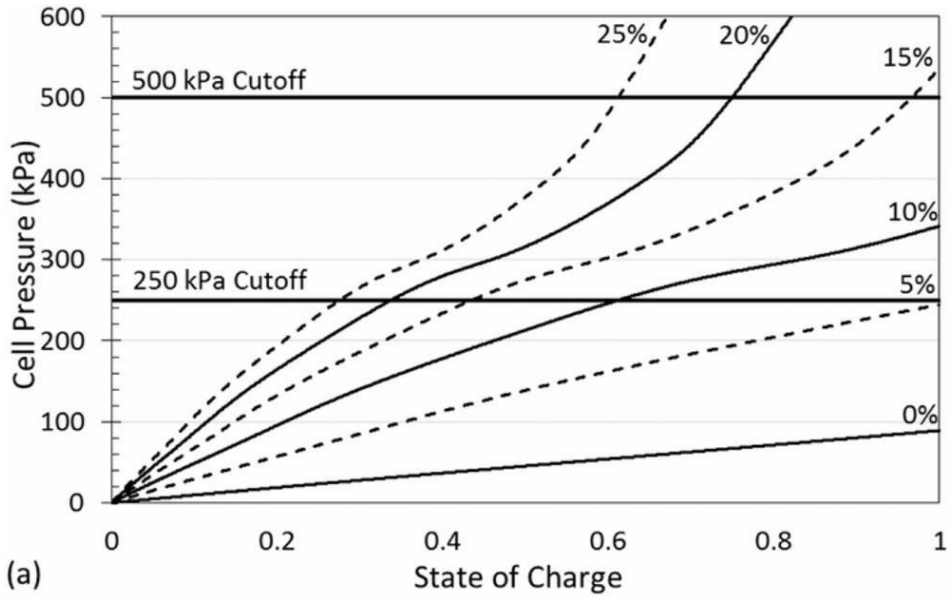

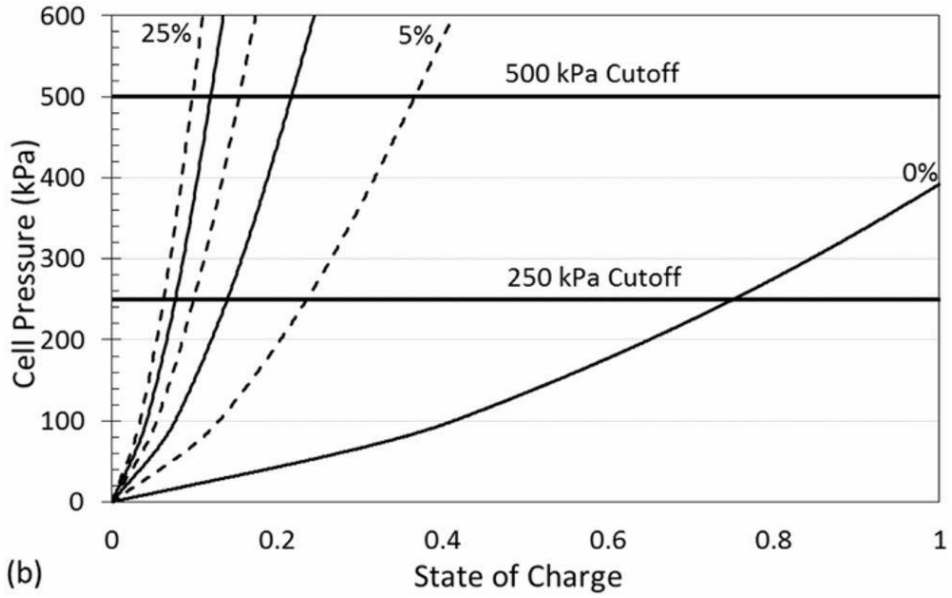

Figure 2.2. Cell pressure as a function of τ for a cell within (a) foam packing or (b) a fixed volume with an initial anode porosity of 0.37. Solid and dashed curves represent incremental 5% increases in silicon composition in the Si/C composite, from 0% to 25%. The solid horizontal lines represent pressure limitations of 250 kPa and 500 kPa.

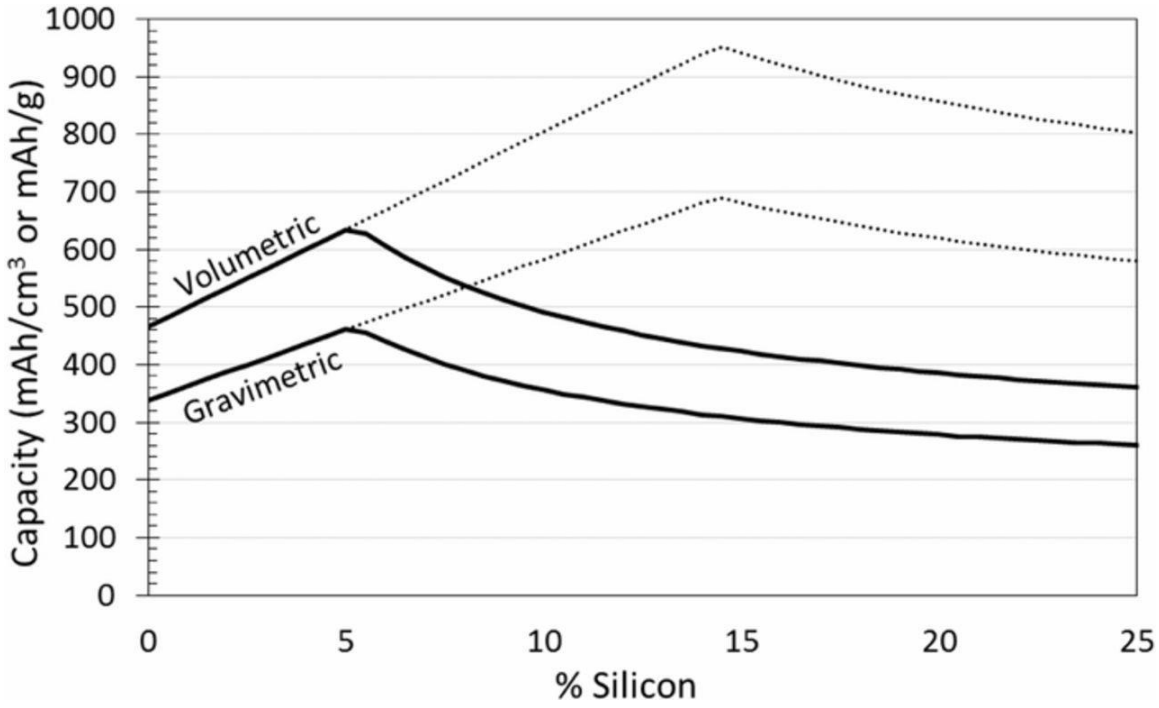

Figure 2.3. Accessible gravimetric and volumetric capacities for a cell with flexible packing and initial anode porosity of 0.37. Solid and dotted lines represent the accessible capacities for the 250 kPa and 500 kPa cutoffs, respectively.

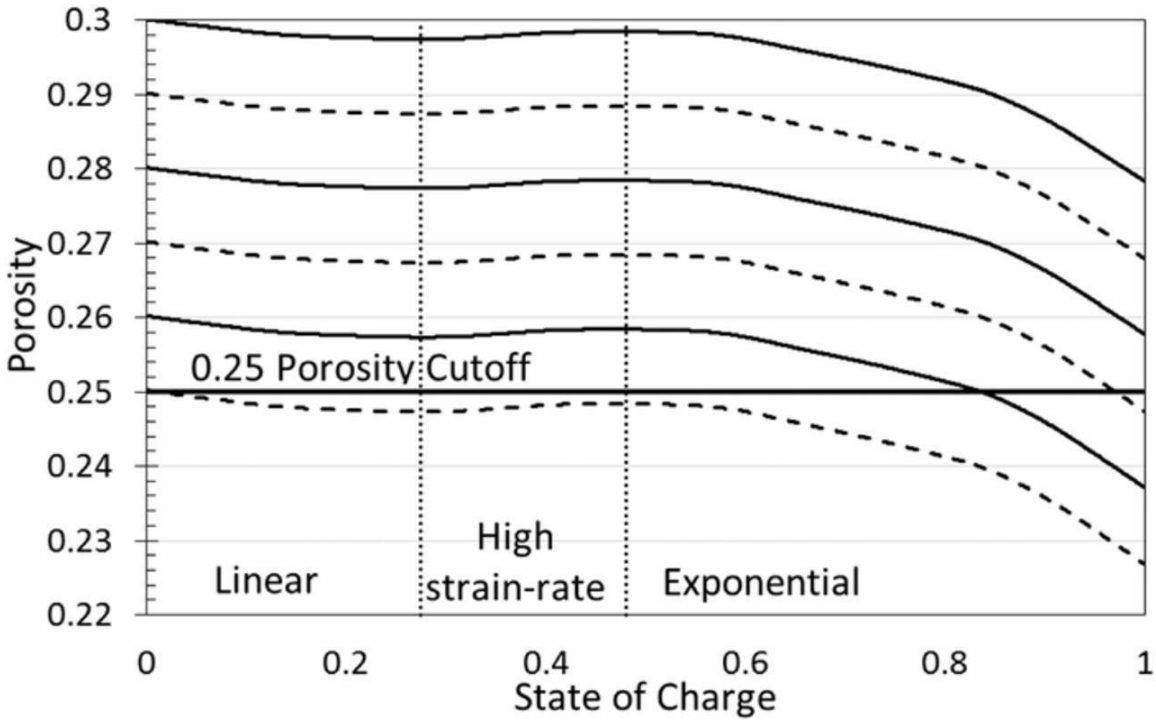

Figure 2.4. Porosity as a function of state of charge for an anode with 25% silicon inside a cell with foam packing. Solid and dashed lines represent incremental 0.01 increases in initial anode porosity from 0.25 to 0.3. The horizontal solid line represents the assigned porosity cutoff of 0.25.

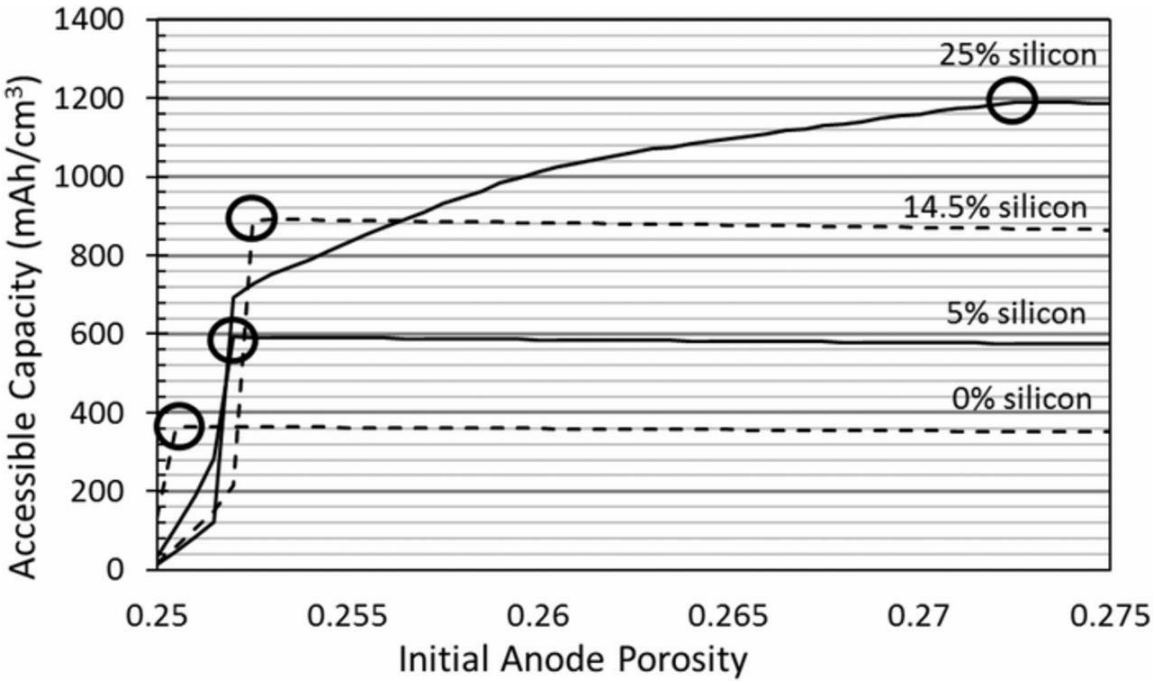

Figure 2.5. Accessible anode capacity, based on the 0.25 porosity limitation, as a function of the initial anode porosity for 0%, 5%, and 13.5%, and 25% silicon anodes within a cell with flexible foam packing. Circles indicate where the accessible capacity peaks then begins to decrease.

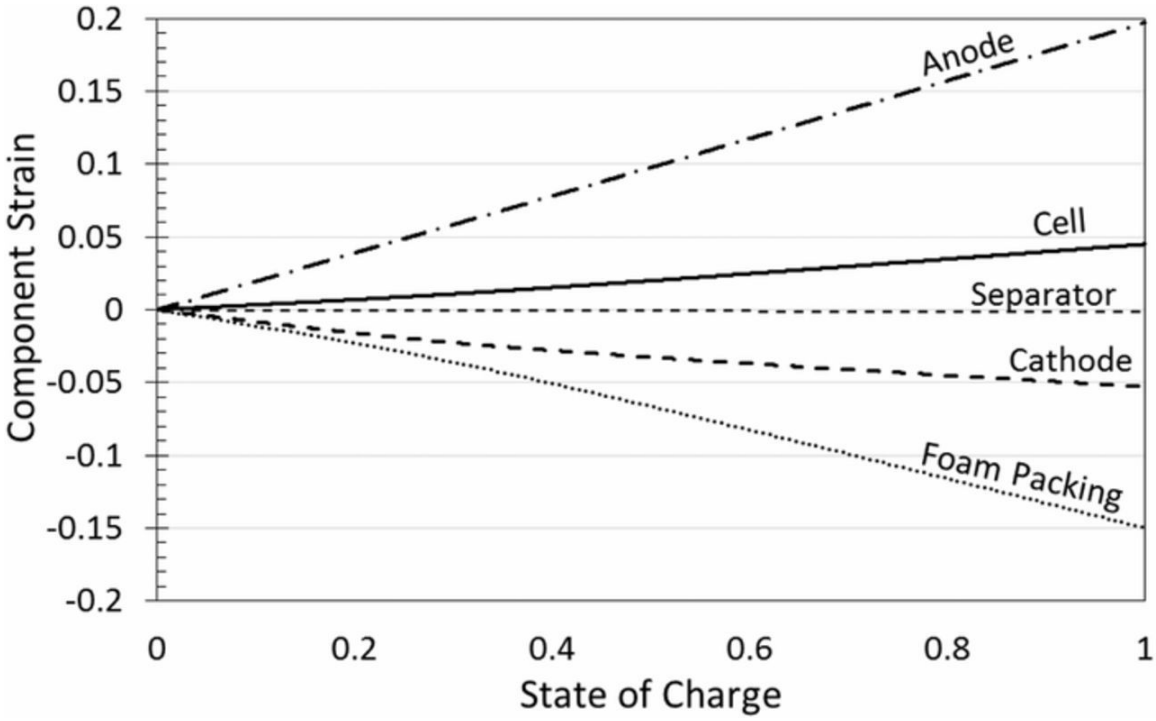

Figure 2.6. Individual component (anode, cathode, separator, and foam packing) and the overall cell expansion/compression as a function of state of charge.

CHAPTER 3

ACCOUNTING FOR NON-IDEAL, LITHIATION-BASED ACTIVE MATERIAL VOLUME CHANGE IN MECHANO-ELECTROCHEMICAL POUCH CELL SIMULATION

This chapter focuses on accounting for non-ideal, lithiation-based active material volume change to generate more accurate simulations of cell level volume change and includes experimental validation. Some results from this work were presented at the Meeting of the Electrochemical Society in Atlanta, Georgia in October 2019 and virtually in October 2020.(74, 75) This work was also published in the Journal of the Electrochemical Society in April 2020.(76)

The societal push to utilize clean, renewable energy has increased motivation for the automotive industry to manufacture electric vehicles (EVs). However, obstacles including high costs, charging time, and driving range, have prevented widespread public adoption of EVs.(77) EV manufacturers focus much effort on the battery pack design with the objective of reducing or removing these obstacles; however, active material volume change phenomena significantly complicates their efforts. Many current production EVs contain large-format pouch cells inside the battery pack. These pouch cells will undergo dimensional changes during the charge/discharge cycle, caused by lithiation-based active material expansion and contraction in the anode and cathode layers. Some battery packs

have modules that contain cooling fins, thermistors, foam separators, and repeating frame elements to hold the cells, maintain temperature, and manage volume change.(43) Additionally, each module is connected to an adjacent module with bus bars and structural bars. As the cells expand and contract during cycling, the stresses generated can cause the materials in the module to deform and crack, resulting in a loss of electrical contact and therefore, decreased range, or a loss of heat transfer fluid, which results in a loss of effective cooling. The pressure generation also has an effect inside the cell, leading to decreased porosity, meaning higher ionic diffusion resistance across the electrode thickness(44); as well as the pulverization and detachment of the active material inside the electrode matrix, reducing capacity.(45) In addition to the effects from pressure generation, lithiation-based dimensional changes of the anode and cathode can also affect the cell's performance (e.g., the ionic and solid phase diffusion will dynamically vary with cell state-of-charge and active material state-of-lithiation, respectively).

It is necessary to account for the complex linkages between mechanical and electrochemical phenomena in the pouch cell environment when selecting new cell and pack materials or designing the electrode, cell, module, and overall pack structure. Furthermore, understanding the coupled mechano-electrochemical phenomena is becoming increasingly important as new, promising anode active materials exhibit significantly more volume change than the 10% volume change of traditional graphite anodes.(69) For example, silicon shows promise as an anode active material because of its high theoretical capacity (4200 mAh/g for $Li_{22}Si_5$(78)); however, silicon can undergo up to 400% volume change between the fully lithiated and delithiated states.(38, 60) Battery designers hope to comprehensively consider promising future cell and pack designs while

accounting for active material volume change. Mechano-electrochemical predictive ability would accelerate the development of promising battery technology while decreasing the required testing load and cost.

To better understand the link between lithium-ion (Li-ion) battery mechanics and electrochemistry, many research groups have investigated and modeled a variety of mechano-electrochemical phenomena. On the particle scale, Christensen and Newman developed a mathematical model of stress generation and fracturing inside spherical Lithium Manganese Oxide (LMO) particles due to lithium intercalation and material phase change.(79) Zhang et al. simulated intercalation-induced internal stress of ellipsoidal particles and probed the impact of aspect ratio(80), while Ansari et al. evaluated particles with geometric discontinuities.(81) Park et al. produced 3D numerical simulations of stress generation in LMO particles to find that lower diffusivity and higher current density induce a larger gradient in the lithium concentration, which leads to higher stress levels.(82) On the electrode scale, Shim et al. studied the electrochemical response of a natural graphite anode compressed to differing densities.(83) Zhang et al. modeled the mechanical failure behavior of individual electrodes to enable prediction of the consequential electrical/thermal responses.(64) And Zheng et al. studied the correlationship between electrode mechanics and long-term cycling performance for graphite anodes.(84) Finally, on the cell scale, Cannarela et al. investigated the effect of pouch cell constraint on stress evolution and capacity fade.(45) And Xu et al. showed that cell state-of-charge is a critical factor in the cell structure stiffness.(85)

While these previous studies provided significant insight into mechano-electrochemical phenomena, knowledge of how these phenomena impact each other on the

particle, electrode, and cell scales remains incomplete. Because of experimental limitations in simultaneous observation of each scale, a multi-scale modeling (MSM) approach shows promise to comprehensively account for mechano-electrochemical behavior and fill the gap in knowledge. Some groups have used MSM approaches to investigate/predict different mechano-electrochemical phenomena in Li-ion batteries. Zhang et al. developed a representative-sandwich model to simultaneously couple mechanical, electrical, and thermal simulation of a cell under indentation tests.(72) Mai et al. reformulated the pseudo two-dimensional (P2D) battery model to couple large electro-mechanical deformations at the particle and electrode levels.(86) Recently, Ai et al. coupled particle-scale mechanical physics into a pseudo-2D model which allowed them to model stress inhomogeneity in Li-ion pouch cells and indicated the experimental phenomenon of electrode particle fragmentation occurring towards the separator.(87) Previously, our group developed a model which predicts the split between electrode porosity and electrode dimensional changes upon active material particle lithiation.(52-54) This volume change model was used to show the theoretical effect of a cell casing's compressibility on porosity as well as the formation of non-uniform reaction distributions at high C-rates. Recently, our group incorporated realistic mechanical behavior for the individual cell components and cell packing to simulate realistic electrode-scale and cell-scale mechanical responses.(59) This MSM was used to show how varying the Si/C ratio in the composite anode would affect cell pressure generation and electrode porosity during cell operation.

However, our previous work assumed a linear or "ideal" relationship between active material lithiation and volume change. In reality, active materials can have a

thermodynamically “non-ideal” relationship between volume change and solid phase lithium concentration due to crystalline structure or phase changes. That is, active materials volume will be dependent on lithium concentration, but may undergo crystalline structure or phase changes that can affect the rate at which the active material volume changes upon lithiation. For example, the commonly used graphite anode active material undergoes several stages of lithiation, which includes a “liquidlike” phase that exhibits very little volume change during lithiation.(88) Commonly used cathode active materials, $LiMn_2O_4$ and $LiNi_{1/3}Co_{1/3}Mn_{1/3}O_2$, have also been shown to have non-ideal atomic unit cell volume change as the materials lithiate.(89) In this study, we consider that material-specific volume change behavior may be important to appropriately predict electrode and cell scale phenomena. Therefore, non-ideal, lithiation-based volume change behavior for the active materials on the particle level was incorporated into our model. To illustrate the impact of non-ideal volume change on mechano-electrochemical predictions, the resulting simulations were compared with experimental measurements of a representative large-format pouch cell and with simulations that assumed ideal volume change behavior.

3.1 MODELING METHODS

The fundamental governing equations and construction of the coupled mechano-electrochemical model used in this study has been described in previous work.(52-54, 59) During charging and discharging, Li^+ ions move from the cathode to the anode and from the anode to the cathode, respectively. The lithiation and de-lithiation of the anode and cathode lead to active material volume change. As shown previously by Garrick et al.(54), the volume change phenomena are based on the material balance governing equation shown below:

$$\frac{\partial\,(1-\varepsilon_i)}{\partial \mathrm{t}} + (1-\varepsilon_i)\frac{\partial\,\varphi_i}{\partial \mathrm{t}} = -\frac{s_i \Delta \hat{V}_i}{n_i F} J_i \qquad [3.1]$$

The right side of the equal sign represents the volume change due to the intercalation or de-intercalation of Li^+ in the electrode active material. This volume change either causes change in the electrode layer dimensions (second term on the left) or change in electrode porosity (first term on the left). J_i, is the variable that links the volume change behavior to electrochemical kinetics, and thus, the rest of the electrochemical and transport phenomena within the anode, cathode, and separator.

In order to accurately simulate mechanical behavior of the full pouch cell (e.g., the thickness change, pressure generation, etc.), the mechanical behavior of each individual cell component must be incorporated. Previously, the porous electrodes were assumed to follow porous rock mechanics(52-54); however, a recent study measured the practical stress/strain response of an electrode saturated with incompressible electrolyte.(64) The porous components in the cell will have a unique stress/strain relationship due to the decreasing porosity (increasing mechanical contact) as well as flow of electrolyte upon compression, therefore, experimentally measured mechanical response was imported from literature for this study to ensure realistic simulation. Mechanical responses of the anode, separator, and cathode were determined in the model using an interpolation function, f_i, of the measured data. This strain response from an externally applied pressure will be denoted, $\varphi_{mech,i}$. However, in an electrochemical cell system, the anode and cathode layers will have another contribution to their overall strain response. The second phenomenon is the electrode layer expansion/contraction caused by the active material volume change due to Li^+ intercalation, $\varphi_{int,i}$. The magnitude of the volume change is related to active material

state-of-lithiation, τ_i. In this study, it is considered that anode and cathode active material state-of-charge ranges can differ between each other and the overall cell state-of-charge, based on how the cell chemistries are balanced in a given pouch cell system. To avoid confusion throughout this report, these differences are distinguished by defining dimensionless unit or pouch cell charge as "state-of-charge" and dimensionless active material charge as "state-of-lithiation", τ_i.

The novelty of this study is that the thermodynamically non-ideal (non-linear) active material volume change relationship with state-of-lithiation is accounted for, where previously, an ideal (linear) relationship was assumed.(59) That is, the effects of changing crystalline phase upon lithiation is accounted for in the prediction of volume change. Therefore, $\left[\frac{\Delta\hat{V}}{\hat{V}^0}\right]_i$, is redefined from our previous studies to be the non-ideal volume change ratio. That is, $\left[\frac{\Delta\hat{V}}{\hat{V}^0}\right]_i$, is the ratio of the current active material volume to the volume of the active material at a fully delithiated state. The non-ideal lithiation behavior for each active material was obtained from literature(88-90) and incorporated into the model via an interpolation function, where $\left[\frac{\Delta\hat{V}}{\hat{V}^0}\right]_i$ is a function of τ_i. Therefore, the intercalation-based active material volume change's contribution to total electrode strain is as follows:

$$\varphi_{int,i} = \left[\frac{\Delta\hat{V}}{\hat{V}^0}\right]_i (\tau_i) \qquad [3.2]$$

Composite electrodes are often used to include promising new chemistries while balancing performance, stability, and capacity.(78) For composite electrodes, $\left[\frac{\Delta\hat{V}}{\hat{V}^0}\right]_i (\tau_i)$, is

calculated as the sum of the individual active material non-ideal volume change ratios multiplied by their respective initial volume fractions in the electrode:

$$\left[\frac{\Delta\hat{V}}{\hat{V}^0}\right]_i(\tau_i) = \sum\left(\left[\frac{\Delta\hat{V}}{\hat{V}^0}\right]_{AM}(\tau_i) * y_{AM}\right) \quad [3.3]$$

Combining the mechanical and intercalation-based strain contributions produces an overall electrode-layer strain response in an operating cell. This equation represents the operando mechanical response of the cathode and anode layers.

$$\varphi_i = (\varphi_{mech,i} + \varphi_{int,i}) = -f_i(P) + \left[\frac{\Delta\hat{V}}{\hat{V}^0}\right]_i(\tau_i) \quad [3.4]$$

The strain for the anode and cathode current collectors is assumed to follow linear elastic mechanics:

$$\varphi_i = \frac{P}{E_i} \quad [3.5]$$

The high Young's Moduli values, E, for the copper anode current collector and aluminum cathode current collector render them virtually incompressible compared to the other components within the cell, especially when considering the pressure windows relevant to automotive battery packs.

In summary, we assume that each component in the cell will experience the same stress in the thickness direction of the cell, or the cell's face pressure. This pressure variable, along with each component's strain response, which is described by a data-driven interpolation, Eq. [3.4], or Eq. [3.5], is what links each individual component strain. Then, as the electrode active materials expand and contract upon cell operation (linked to electrochemical operation by Equation [3.1]), changes in electrode dimensions, pressure,

and porosity will occur. Many of the parameters that dynamically vary with the active material volume change also affect electrochemical calculations (e.g., porosity and electrode thicknesses will affect diffusion through the liquid phase).

In this study, we specifically focus on the effect of non-ideal active material volume change on the prediction of a large-format pouch cell's thickness. EV battery pack manufacturers have a minimum pressure requirement at assembly for packs containing pouch cells to ensure sufficient thermal, mechanical, and electrical contact. They aim to maintain this pressure over the life of the pack, and typically will accomplish this using foam inserts between the cells. Therefore, the model simulations in this study were run with an initial applied pressure, typical of the pressures seen at pack assembly, which is maintained even as the pouch cell changes in volume. To do this, a perfectly compliant region was added to the model geometry, allowing for the unit cell to expand and contract freely, while still maintaining the initial applied pressure. This constant pressure effectively isolates the lithiation-based volume change and its impact on dimensional changes, while negating the strain and relaxation responses that changing pressure might have on each of the cell components. Then, the simulation could be scaled up from component scale to the cell and pouch scales, representing the ability for simulation of total large-format pouch cell mechano-electrochemical behavior.

3.2 EXPERIMENTAL METHODS

Electrochemical Measurements:

Confirming the electrochemical simulation is necessary before predicting mechano-electrochemical phenomena. In this study, we focus on low-rate operation of a large format pouch cell. Therefore, the capacity and the open circuit voltage (OCV) were

experimentally determined. The pouch cells were trickle-charged to a desired cutoff voltage. The pouch cells would be constrained to a low pressure and kept at a constant temperature using a thermal chamber to remove the effects of temperature. Then the cells could be discharged at a constant low rate to a voltage cutoff while recording voltage, current, and time. These variables could be used to determine the voltage as a function of cell state-of-charge as well as the total capacity of the cell. These electrochemical measurements could then be used to validate model simulation, confirm cell specifications, and be utilized to design the mechano-electrochemical experiments.

Measuring Intercalation-based Thickness Change:

To properly capture how a pouch cell's thickness changes due to anode and cathode intercalation-based volume change, measurement equipment is needed that can maintain a constant pressure while measuring precise changes in cell thickness. Maintaining a constant pressure is imperative in this study because the focus is on how lithiation-based active material volume change will affect dimensional changes in the electrodes, and thus, the overall pouch cell during low-rate operation. Maintaining a constant pressure provides the assurance that the measured thickness changes are not a result of any cell component strain or relaxation responses from a changing applied pressure as opposed to the changes from lithiation-based volume change. Maintaining the pressure effectively negates the mechanical effects of strain in the electrodes, separator, current collectors, and the cell's pouch itself. In practical applications, pack designers will also try to maintain constant pressure in the pack to produce sufficient electrochemical, thermal, and electrical contact without causing capacity fade or structural concerns in the cells and pack.

Therefore, an apparatus, similar to a test setup used in another study (45), was developed to maintain a constant pressure while taking precise thickness measurements of the pouch cell during electrochemical operation. A four-post press was modified as depicted in Figure 3.1, with the large-format pouch cell's location between two steel plates in the press apparatus. A mechanical load cell was spherically-seated to the top plate. Four linear variable differential transformers (LVDTs) were attached to the four corners of the top plate. The LVDTs were used to measure the strain response, or thickness change, of the cell by taking the average displacement between the top plate and bottom plate. The cell footprint was oriented centrally between the plates with the cell's tabs exposed on the side of the plates, allowing for non-invasive connection to a potentiostat. During testing, a thermocouple could also be placed near the tabs of the cell to ensure low temperature variation, thus, no thermal contribution to electrochemical or mechanical parameters in the cell. The software controlling the press was programmed to lower the top plate until reaching a desired force, which translates to the cell face pressure. After reaching the desired force, the press would continually lower the top plate to maintain that force, similar to how a mechanical creep test is performed. After the initial compression, the cell mechanically relaxes, decreasing in thickness, until reaching a point where the thickness change is no longer measurable or significant. The cell is then ready to be discharged using an appropriate low C-rate, determined from the previously measured cell capacity. As the pouch cell is discharged, the cell thickness decreases again, this time caused by lithiation-based active material volume change. The press would continue to lower the top plate to maintain the set force, causing the displacement between the top and bottom plate to

decrease. Ultimately, the displacement between the two plates and the voltage, both a function of time, were used to determine the cell thickness as a function of state-of-charge.

3.3 RESULTS AND DISCUSSION

Representative Large-Format Pouch Cell:

The representative large-format pouch cell used in this study is a NMC/LMO:Graphite pouch cell. This cell was determined to have a ~24.9 Ah at 298K capacity as measured from a common Li-ion operational voltage range, 2.5 to 3.2V.(91) The pouch cell is comprised of several negative and positive electrodes that are rolled into a jelly-roll using a polypropylene co-polymer separator.(92) The negative electrodes are made up of a graphite anode active material, bound with Styrene-Butadiene Rubber (SBR) and Carboxymethyl Cellulose (CMC) binders(93), double-side coated on a copper current collector. The positive electrodes are made of a 70% lithium-nickel-manganese-cobalt-oxide (NMC)/30% lithium-manganese-oxide (LMO) cathode active material(94), bound with a Polyvinylidene Fluoride (PVDF) binder(93), double-side coated on an aluminum current collector. The pouch cells used in this study were in a new, pack-ready condition. The specifications for this pouch cell and its individual components are reported in detail in Table 3.1.

Mechano-electrochemical Model:

The model was set up in COMSOL Multiphysics Version 4.4 using the Partial Differential Equations (PDE) interface to incorporate the governing equations for the physics, which has been described in the “Model Setup” section. Cell discharge was simulated with the Time Dependent Solver tool; the governing PDEs were solved using an

iterative, numerical solver method. Figure 3.2 depicts the model geometry and how it relates to measured thickness change for this study. The model is based on the unit cell shown in Figure 3.2, with an additional region to represent the constant pressure being applied to the cell. The unit cell can be scaled up by the number of repeating units in the pouch cell to predict the overall mechanical and electrochemical behavior of the pouch cell.

To accurately represent the mechanical behavior inside of the pouch cell, mechanical strain responses for the anode, cathode, and separator were taken from literature.(64, 95) The copper anode and aluminum cathode current collectors followed linear elastic mechanics, Equation [3.5], with their Young's Moduli being obtained from literature.(96) These stress-strain responses were used to determine the component level strain to the initially applied pressure relevant to automotive pack assembly, 30 kPa, which was held constant for this study.

The key addition to this model is the inclusion of the non-linear, lithiation-based volume change. For the graphitic anode, the volume change profile was incorporated from a previous study found in literature.(90) Figure 3.3a shows the data for graphite volume change ratio (active material volume divided by the de-lithiated volume) as a function of state-of-lithiation, from 0 to 1. Also included is the polynomial fit of the data to be used as a model input as well as the ideal (linear) volume change behavior assumed in previous models. The graphite profile exhibits a particularly unique lithiation stage, which is evident in Figure 3.3a at the lithiation fraction range of 0.25 to 0.5. The graphite is said to transition to a "liquid-like" phase between lithiation stage-3 and stage-2, noted with 2L.(88, 90) This phase is a defining feature in the graphite expansion profile, the graphite maintains a

constant volume as it lithiates, and will significantly impact the overall pouch cell's expansion profile. From Figure 3.3a, the fit of the data used in the model captures many of the unique features caused by the phase changes, while the previously assumed non-ideal volume change profile does not. Therefore, we can expect to see their impacts, especially the defining "2L+2" phase, on the overall pouch cell behavior. The cathode active material expansion profile was not readily available in literature. However, Nam et al. previously conducted a study using in-situ X-ray diffraction (XRD) to study mixed NMC/LMO composite cathodes during charge and discharge cycles.(89) One of the unique features of their study was the ability differentiate between the layered (NMC) and spinel (LMO) phases in the resulting XRD data. Because of this, they could calculate the unit cell volumes for both LMO and NMC as a function of cell charge in a functional voltage range, 2.5 to 3.2V. We assumed that the unit cell volumes could translate to the active material volume expansion and that the cell capacity within the functional voltage range could translate to the active material's lithiation fraction in order to derive volume change profiles for both NMC and LMO. Figure 3.3b shows the resulting data scaled to show the volume change ratio as a function of the active material lithiation fraction for both NMC and LMO. Like graphite, the polynomial fit was used to represent this data, however, we assumed that we could combine the profiles, weighted by the percent of material in the cathode (70% NMC and 30% LMO), to generate a unique profile for the composite cathode. Figure 3.3b shows the resulting cathode profile used as an input for our model. Because of the small volume change of NMC and the lack of major features like graphite, the difference between the ideal and non-ideal behavior is minimal, therefore, the total cell volume change profile is expected to be primarily governed by the graphite profile. The profiles used here are

assumed to be valid when considering low C-rate pouch cell operation. The impact of high C-rates on the volume expansion profiles of single and multi-material electrodes will be the focus of future studies. Incorporating these profiles into our previously developed coupled model yields the base model for unit cells with graphite-NMC/LMO chemistry. The base model is scaled up to the pouch cell level by multiplying by the number of unit cells. With the coupled model developed, it could then be paired with appropriate design specifications and model parameters for our specific pouch cell.

The base model was populated with relevant parameters to represent the NMC/LMO:Graphite cell. Table 3.2 lists all relevant parameters that were used in mechano-electrochemical model; they were measured, taken from the COMSOL material database, or taken from literature. One key aspect of this work is determining initial and final state-of-lithiation for the anode and cathode. In production cells, many manufacturers will try to maximize the lithiation fraction range of the cathode active material due to its expensive cost. This typically leaves excess graphite material. It is important to note that in practical operation, excess anode active material will still be lithiated and that the average state-of-lithiation of the active material in the electrode will decrease as the excess material increases. Additionally, when we compare this model to a practical cell, we must understand that both the anode and cathode will not fully lithiate/delithiate when using strict cutoff voltages at constant-current operation. This imbalance of cell chemistry, leading to individual anode and cathode operational state-of-lithiation ranges, is important when predicting the volume expansion profile of the cell. Therefore, the lithiation fraction ranges of the anode and cathode were determined. Using the base mechano-electrochemical model, parameter estimation was conducted with the Optimization Module

provided by COMSOL. The optimization tool was set to solve up to 300 parameter sets while using an algorithm to determine the more sensitive parameters and tuning selected parameters to minimize the Least Squares Error. The optimization tool was programed to find the starting and ending lithiation fractions of the anode and cathode using the pouch cell's measured open-circuit voltage and known electrochemical parameters of the materials inside the cell. Cell information was determined using a recently patented method to relate half-cell open circuit voltages and full-cell open circuit voltages.(97) Using practical data in the fitting method encourages the parameters to be physically-relevant, meaning better extrapolation accuracy. In this pouch cell, the anode lithiation fraction ranged from 0 to 0.71 and the cathode lithiation fraction ranged from 0 to 0.87. Note that the cell state-of-charge ranges, from 0 to 1 by default, based on the cutoff voltages. This is important information when marrying the electrode expansion profiles to the cell expansion profile. The cell's profile is formed by taking only the volume change profile within the operational range for both the anode and cathode, which creates a unique expansion profile for the cell. Our model accommodates this by using the individual active material states of charge when calculating the expansion, as opposed to cell state-of-charge. The resulting model for the NMC/LMO:Graphite pouch cell was then validated to predict electrochemical performance and pouch cell thickness change.

Electrochemical Measurements and Model Validation:

The pouch cells were first measured electrochemically to ensure model fidelity in electrochemical predictions. The cells were placed in a Cincinnati Sub-Zero Environmental Chamber for temperature control (298K) and connected to an industrial Bitrode Cycler. First, the cell was discharged (from 3.2 to 2.5V) at the estimated C/10 rate, where C is

equivalent to the capacity of the cell from 2.5 to 3.2 V divided by one hour. Figure 3.4 shows the resulting voltage profile of the pouch cell compared to the model prediction. As seen in the figure, the simulation and experimental data agree well, even in the lower state-of-charge window where the voltage drops off significantly. This means that our model is sufficiently representing the pouch cell for low-rate operation. This test was also used to determine capacity from the total discharge current. The capacity of the NMC/LMO:Graphite pouch cell was determined to be 24.9Ah, which was used to select an appropriate current for low-rate operation.

Mechano-electrochemical Measurements and Model Validation:

The thickness of three separate NMC/LMO:Graphite pouch cells during low-rate discharge was measured using a modified four-post Promess Press apparatus, depicted in Figure 3.1. The pouch cell was placed with its footprint centered between the plates and the tabs left accessible on the side of the plates. An MTS 661.19C-02 Force Transducer (Load Cell) was spherically-seated to the top plate to measure force, accurate to one Newton. Four Ametek DT5S Feather Touch probes (LVDTs), accurate to one-tenth of a micron, were attached to the corners of the top steel plate to measure the displacement between the top and bottom plate. The four LVDTs were connected to a Solartron Metrology interface to convert the voltage responses to displacements. The LVDTs were calibrated by measuring the displacement between the two plates using 8.000 mm gauge blocks. The LVDT calibration displacement was 2.500 mm because their operational measuring range is 0-5 mm and the accuracy will be highest in the center of this range. The load cell and LVDTs were connected to a DEWESoft Sirius data acquisition system which connects with DEWESoft software to manage and store the data.

The cells' tabs were connected to a Gamry Reference 3000 Potentiostat which included a Gamry Reference 30K booster. In preparation for the test, the cells were charged at C/2 until reaching a 3.2V cutoff; then the cells were potentiostatically trickle-charged until the current was less than C/200. The fully-charged cell voltage was 3.125, representing a state-of-charge of 0.99. After electrochemical relaxion for over 24 hours, the volume change would be measured.

The press controls were programmed and operated using MotionPro software. The program lowers the top plate until reaching a pressure of 30 kPa, then, the press continues to lower the top plate in order to maintain a constant pressure as the cells relax. The cells were allowed to mechanically relax for thirty minutes, where the thickness change due to relaxation was no longer significant or measurable. The cells would then be prepared for the test and were ready to be discharged. The potentiostat discharged the pouch cells at C/10 until the cell would reach a voltage cutoff of 2.5V. During discharge, the cells decrease in thickness, which triggers the MotionPro program to lower the top plate to maintain the 30 kPa pressure. The displacement between the top plate and the bottom plate was recorded as a function of time and thus, state-of-charge and voltage.

The resulting data is presented in Figure 3.5, which shows the cell strain as a function of state-of-charge. The cell strain is calculated by taking the cell thickness divided by the minimum cell thickness at a state-of-charge of 0. The experimental error between the three pouch cells tested, noted in Figure 3.5 with error bars, indicate that the manufacturing variation between cells is minimal. From Figure 3.5, reasonable agreement is shown between the measured data and the simulation case using non-ideal lithiation behavior. Meanwhile, the case with ideal volume change behavior does not capture any of

the distinguishable graphite features and significantly overestimates the total thickness change. Total cell thickness change is one of the more important specifications needed for battery pack design, especially considering pack designers who need to select dimensions of repeating frame elements, as well as the foam packing material and thickness. The simulation with non-ideal lithiation over-predicts the cell strain with an error of 2.7%, while the ideal lithiation over predicts the cell strain with an error of 10.3%. This indicates that the model using non-ideal lithiation reasonably accounts for the total cell volume change using only particle-level lithiation-based volume change as an input. However, there is more significant error in the other state-of-charge ranges. The highest error occurs at the volume change profile's "elbows", seen at a cell state-of-charge ranges of 0.05-0.3 and 0.6-0.9. This means that the unique 2L phase change that graphite undergoes is well captured in the model, but the transitions to other phases in graphite and NMC/LMO are not as well-represented.

We consider that some of the error at the "elbows" in Figure 3.5 may come from the polynomial fits, the assumed cathode volume expansion profile (weighted combination NMC and LMO profiles), or the electrode profiles' dependence on C-rate. Different C-rates can affect how NMC and LMO preferentially lithiate as well as determine how uniform the crystalline phases are in the anode and cathode. In the study shown here, we are focusing on low-rate discharge; however, the effect of C-rate on the lithiation of composite electrodes will be the focus of future work. For designers of automotive battery packs, this tool predicts the dimensional changes with great accuracy and can be used to optimize design of the pack.

Theoretical Simulations:

The model uses particle-scale active material volume change to predict electrode scale expansion and overall pouch cell scale expansion. With the cell-scale expansion showing reasonable agreement with measured data, the model can be used to further simulate internal mechano-electrochemical phenomena, and in turn, can be used to identify how changes to the cell chemistry might affect mechanical behavior. For example, this model gives information about the individual anode and cathode strain behavior. Figure 3.6 shows the cell strain simulation and data with the corresponding anode and cathode strain from the simulation. It is more evident here how the anode and cathode layers contract and expand, respectively, during the cell discharge. If the anode and cathode strains are compared to the active material volume change profiles from Figure 3.3, it is evident that the anode lithiation fraction is ~0.71 during the cell discharge while the cathode is ~0.89 as found in the parameter estimation. Information of the individual anode and cathode layer expansion/contraction during cell cycling can be valuable for some design aspects. For example, a separator in a jelly-roll can be prone to wear at the folds, and knowing the amount of separator displacement over a full cycle, caused by the anode/cathode expansion/contraction, gives helpful information for required separator durability.

We also propose that designers may be able to use this model to balance cell chemistry in a more effective way during the design phase, taking advantage of the non-linear volume expansion profiles found in current and future electrode materials. Traditionally, a method of balancing chemistry would be matching the anode and cathode electrode capacities so that there is no “wasted” electrode material (i.e., the same amount

of active lithiation sites would be found in the anode and cathode). This would reduce material cost but would also mean that the operational state-of-lithiation range for the anode and cathode would both be close to 0-1. A different method is to balance cell capacities so that there is minimal active material volume change. One example of this is to balance the cell so that the operational state-of-charge of the cell mostly coincides with graphite's 2L phase that exhibits little volume change. Because this model incorporates graphite's unique volume change profile, it can be used to determine how adding or subtracting graphite material affects the operational state-of-lithiation range in the anode. Reducing the graphite state-of-lithiation range to operate mostly along graphite's 2L phase will translate to minimal volume change in the anode and thus, less pressure generation, and possibly, less fracturing and capacity fade.

To illustrate this concept, the same automotive cell parameters were used to simulate a low-rate discharge for similar cells, only differing in delithiated anode thickness. The thickness changes translated difference in total anode active material. Therefore, the anode/cathode capacity ratio, N:P, would change as well as the operational state-of-lithiation range for the anode active material. As the N:P increased, the operational state-of-lithiation of the anode would decrease, and vice versa. Figure 3.7 shows the resulting discharge profiles from the simulation of the original cell as well as the two new cells. As the N:P increases, the overall strain exhibited by the cell during discharge decreases because of the relatively lower lithiation range of graphite. Even though the cells were discharging the same total current, the total strain for the cells were 0.021, 0.018, and 0.014, for the 1.00, 1.25, and 1.67, respectively. In Figure 3.7, volume change profile as a function of anode active material differs in relation to the lithiation range of the graphite. The 1.00

N:P cell almost utilizes the full graphite lithiation profile from Figure 3.3a, while the 1.67 N:P only operated between the active material state-of-lithiation ~0-0.55. Because of the unique 2L phase in graphite, the graphite volume change was reduced by ~33% between the 1.67 and 1.00 N:P cells. This reduction of active material volume expansion can aid in reducing the volume change effects on pack design and may prove to significantly reduce capacity fade caused by the active material volume expansion inside the electrode matrix. Figure 3.7 also includes simulations of each N:P ratio using ideal lithiation-based volume change behavior. It is evident that there are significant differences in the profiles for each case. The prediction for total cell strain seems to overpredict for both 1.25 and 1.67 N:P ratios while the 1.00 N:P ratio case underpredicts by a small amount. Again, this aligns with the unique non-ideal lithiation-based volume change behavior for the graphite active material shown in Figure 3.3a, where the ideal lithiation assumption over-predicts volume change at lithiation fractions of 0.55 and 0.71; then slightly underpredicts and 0.99. This type of model balancing shows promise for optimizing pre-lithiation techniques for anode materials as well. Promising anode active materials that have non-ideal volume expansion profiles, such as silicon(90), as well as cathode materials, can be incorporated into this model to explore maximizing capacity while minimizing volume change and perhaps capacity fade in the cell.

Porosity and Pressure Simulation:

Previously, this type of volume change model was used to simulate pressure generation and porosity change, however, the previous studies assumed the ideal volume change behavior of the active materials. This type of simulation was recreated to observe the effects of non-ideal volume change behavior. For these simulations, instead of

assuming constant pressure, we incorporated a foam packing region that is realistic for use in EV battery packs, which is described in our previous study.(59) The foam used was a generic polyurethane foam.(66) Figure 3.8 shows the simulated pressure and porosity for the simulations of both non-ideal and ideal lithiation behavior as a function of cell state-of-charge. The porosity is inversely related with pressure, which is expected because as the cell face pressure increases, the active material volume change will expand more into pore space (first term on the left of Eq. [3.1]) and less into electrode dimensional changes (second term on the left of Eq. [3.1]). When comparing the ideal and non-ideal cases, we can see the distinguishable graphite volume expansion plateau. Because the active material doesn't fully lithiate, the assumed linear volume expansion over-estimates total pressure generated and the total porosity change. Pressure and porosity are known to have an impact on capacity fade and mass transfer, respectively. This is yet another example of how accounting for the non-ideal lithiation-based volume change behavior can provide more accurate representation of mechanical phenomena inside the cell.

3.4 CONCLUSIONS

Cell and pack designers currently rely on extensive electrochemical and mechanical testing to appropriately account for the volume change. In this study, we illustrated the ability to employ a mechano-electrochemical modeling method to predict volume change, which may help reduce the required number of electrochemical and mechanical tests. To do this, non-ideal, lithiation-based volume change profiles for the electrode active materials were incorporated into a previously developed mechano-electrochemical model. Then, the cell-level simulation was validated with measured pouch cell electrochemical performance data and thickness change data during low-rate discharge. To measure thickness change as

a function of state-of-charge, a unique apparatus was set up to maintain a constant cell face pressure, measure the thickness change of the pouch cell, and electrochemically operate the cell. This assured that the measured thickness change was a result of lithiation-based active material volume change as opposed to mechanical responses from changing pressures. The model predictions proved to agree with the experimentally measured data and captured the primary feature of the volume change profile, the graphite 2L phase. The increased accuracy of the model using non-ideal lithiation behavior shows the importance of accounting for individual active material volume change behavior on cell level predictions. Theoretical predictions of individual component strain, capacity balance effects, porosity, and pressure were also explored. This model can be used to help designers to estimate pouch level volume change using knowledge of particle level lithiation-based volume change behavior. The resulting understanding from the model may aid in cell design or determining operational parameters to mitigate negative effects from active material volume change. Additionally, this model may prove useful to consider how mechanical and electrochemical phenomena intertwine as promising new chemistries are considered.

3.5 TABLES AND FIGURES

Table 3.1. Specifications for the NMC/LMO:Graphite pouch cell, which was used as the representative large-format pouch cell in this study.

	Full Pouch Cell	Anode Current Collector	Anode Coating Layer	Separator	Cathode Coating Layer	Cathode Current Collector
Thickness [µm]	7550	10	66	29	73	25
Cross Sectional Footprint [mm^2]	232x164	198x150	198x150	201x2200	194x147	194x147
Material Type	-	copper	graphite	polypropylene copolymer	70%NMC/30%LMO (by volume)	aluminum
Quantity	-	20	40	1 (rolled)	38	19

Table 3.2. List of design parameters used in the mechano-electrochemical model and analysis.

Parameter	Source	Value
$L_{ncc,0}$	measured	1.0E-6 m
$L_{n,0}$	measured	6.6E-5 m
$L_{s,0}$	measured	2.9E-5 m
$L_{p,0}$	measured	7.3E-5 m
$L_{pcc,0}$	measured	2.5E-5 m
$R_{n,0}$	assumed	8.0E-6 m
$R_{p,0}$	assumed	9.8E-6 m
ε_n	assumed	0.26
ε_s	assumed	0.39
ε_p	assumed	0.26
$\varepsilon_{f,n}$	calculated	0.124
$\varepsilon_{f,p}$	calculated	0.168
$\varepsilon_{AM,n}^0$	calculated	1-ε_n-$\varepsilon_{f,n}$
$\varepsilon_{AM,p}^0$	calculated	1-ε_p-$\varepsilon_{f,p}$
R	known	8.314 J mol^{-1} K^{-1}
F	known	96485 C mol^{-1}
T	measured	298.15 K
$\theta_{n,discharged}$	calculated (97)	2.6E-4
$\theta_{n,charged}$	calculated (97)	0.71
$\theta_{p,charged}$	calculated (97)	1.0E-5
$\theta_{p,discharged}$	calculated (97)	0.87
c_0	COMSOL Material Spec.	1000 mol m^{-3}
$D_{s,n}$	COMSOL Material Spec.	7.5E-14 m^2 s^{-1}
$D_{s,p}$	COMSOL Material Spec.	4.0E-14 m^2 s^{-1}
ρ_n	COMSOL Material Spec.	2.2 g cm^{-3}
ρ_p	COMSOL Material Spec.	3.8 g cm^{-3}
$E_{ak,n}$	COMSOL Material Spec.	70000 J mol^{-1}
$E_{ak,p}$	COMSOL Material Spec.	80000 J mol^{-1}
$\alpha_{a,n}$	assumed (57)	0.5
$\alpha_{c,n}$	assumed (57)	0.5
$\alpha_{a,p}$	assumed (57)	0.5
$\alpha_{c,p}$	assumed (57)	0.5

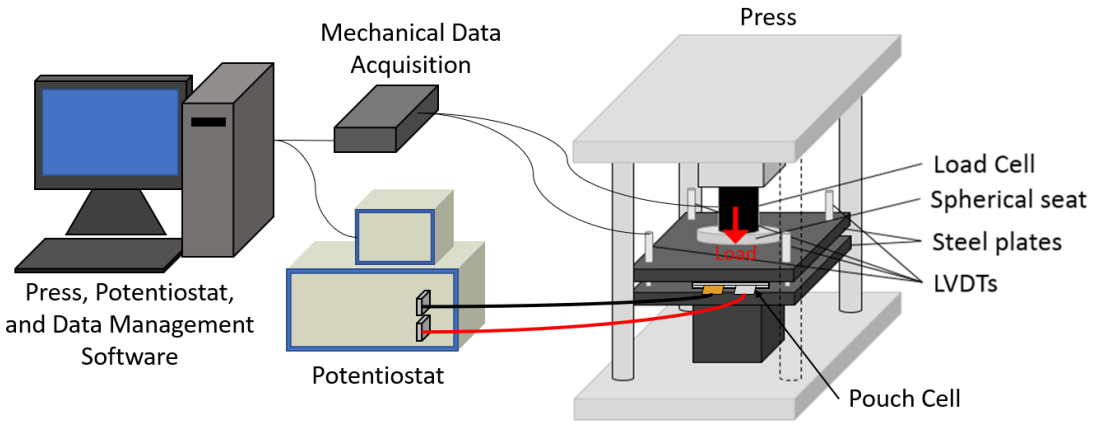

Figure 3.1. The apparatus and equipment design developed for simultaneous mechanical and electrochemical control and observation of the large-format pouch cell.

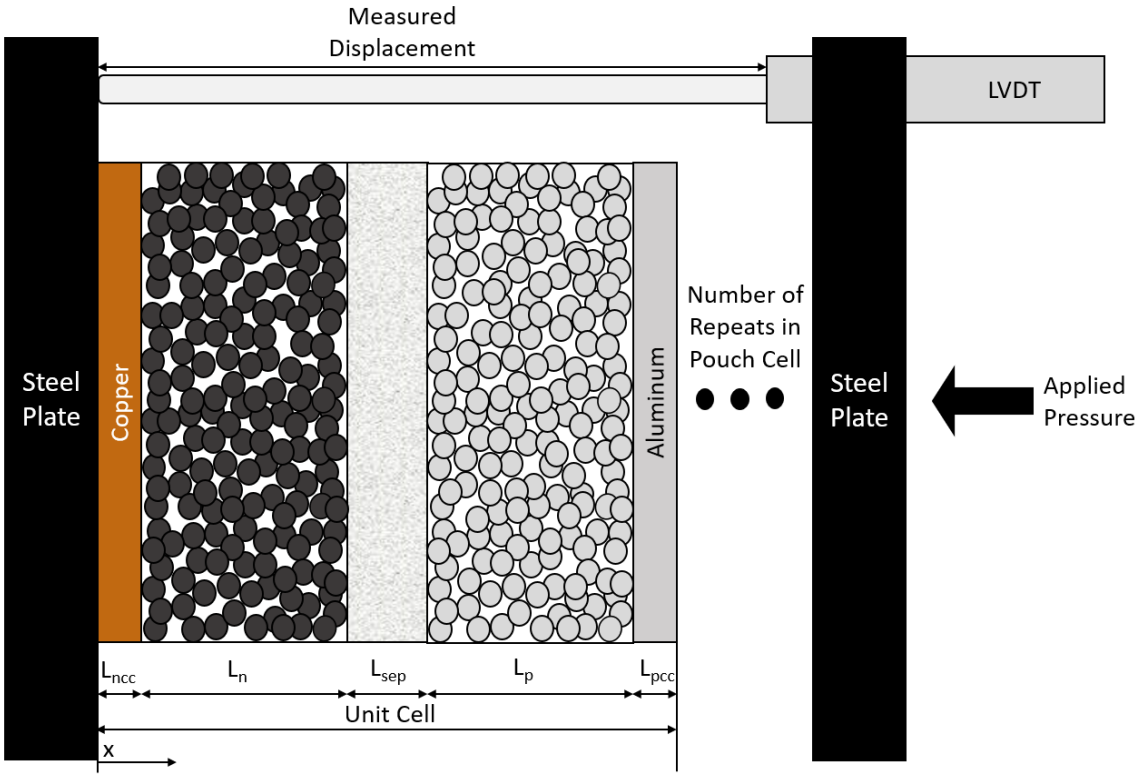

Figure 3.2. Depiction of the pouch cell model geometry inside of the test apparatus from Figure 3.1. The unit cell can be scaled up by the number of repeats in the pouch cell to make pouch cell scale predictions of mechanical and electrochemical behavior.

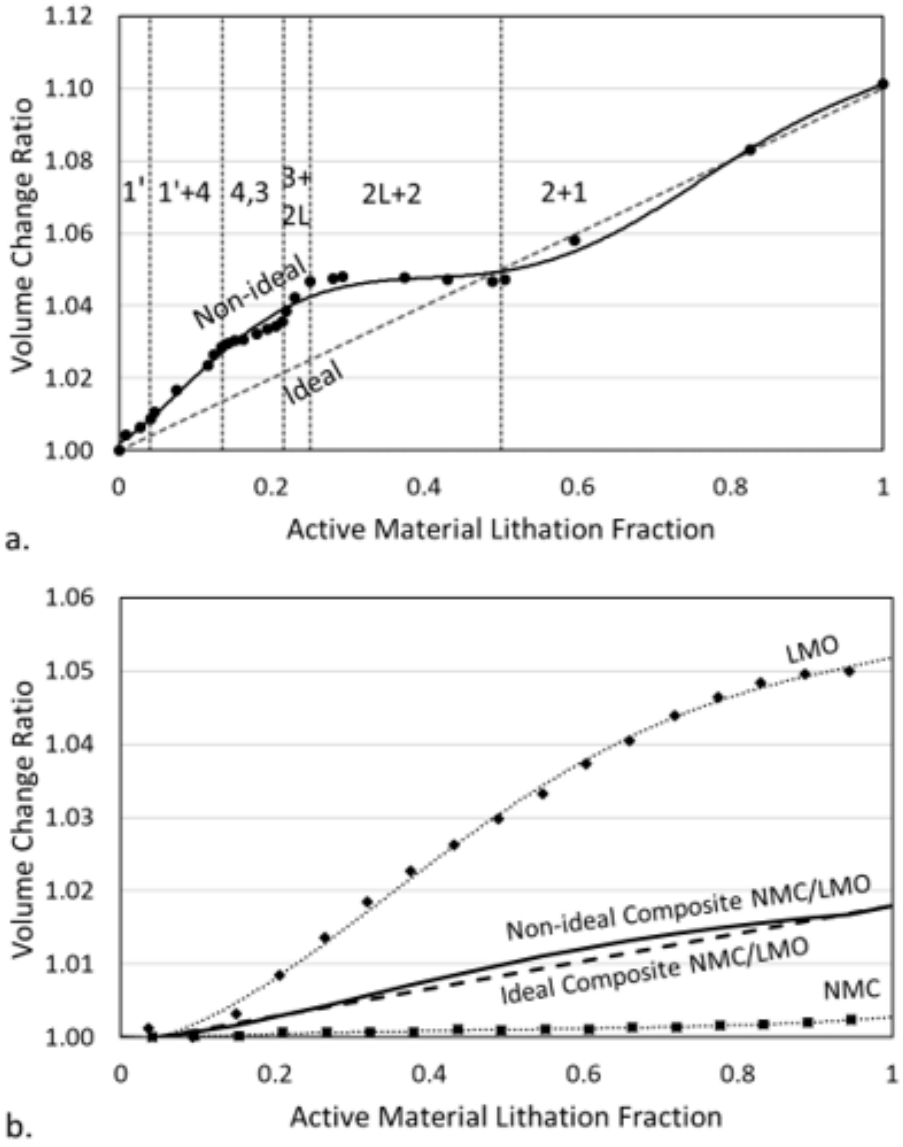

Figure 3.3. The volume change ratio data are shown for (a) anode(88, 90) and (b) cathode(89) materials used in the simulation. Solid lines represent the non-ideal lithiation-based active material volume change profiles used within the simulations. The graphite profile (a) shows significant links to lithiation-based phase changes, marked with vertical dotted lines. Both anode and cathode profiles are compared to a dashed line representing the ideal lithiation behavior.

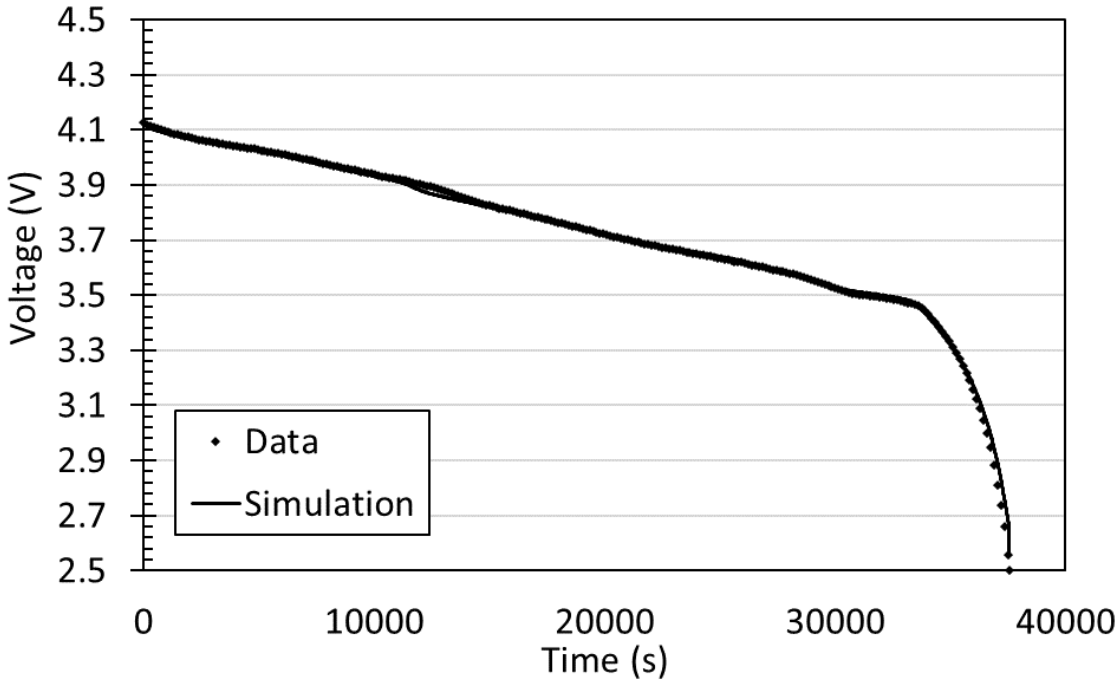

Figure 3.4. Measured data and simulated voltage during a 2.59 A discharge of a 24.9 Ah NMC/LMO:Graphite pouch cell.

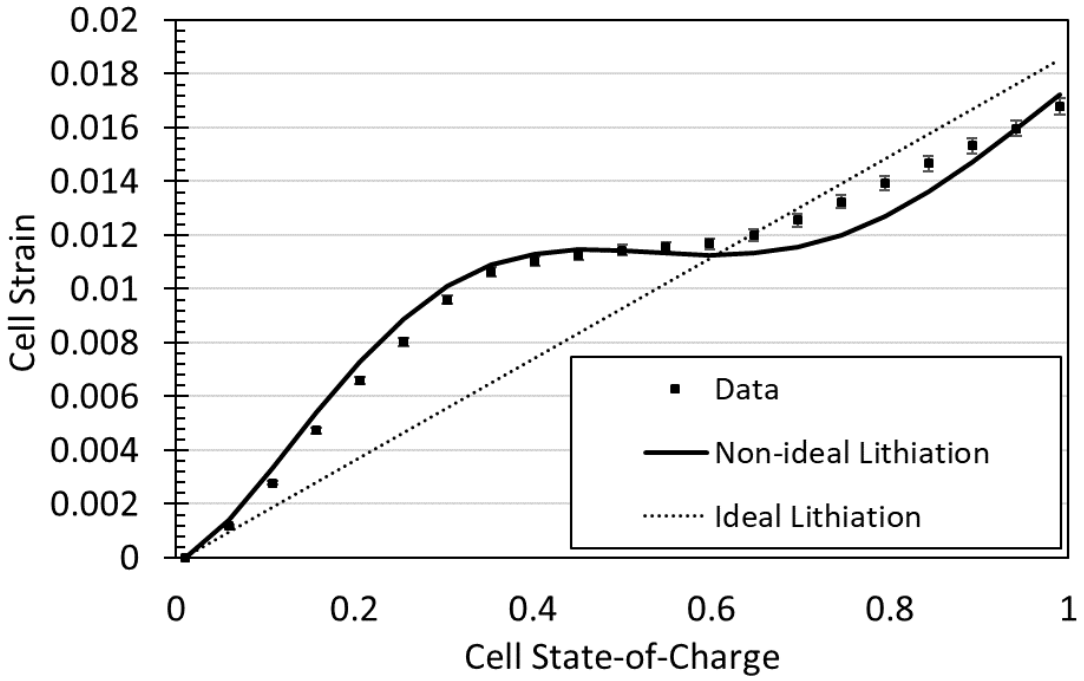

Figure 3.5. Experimentally measured data and simulations using ideal and non-ideal active material volume change behavior for a NMC/LMO:Graphite pouch cell strain as a function of cell state-of-charge.

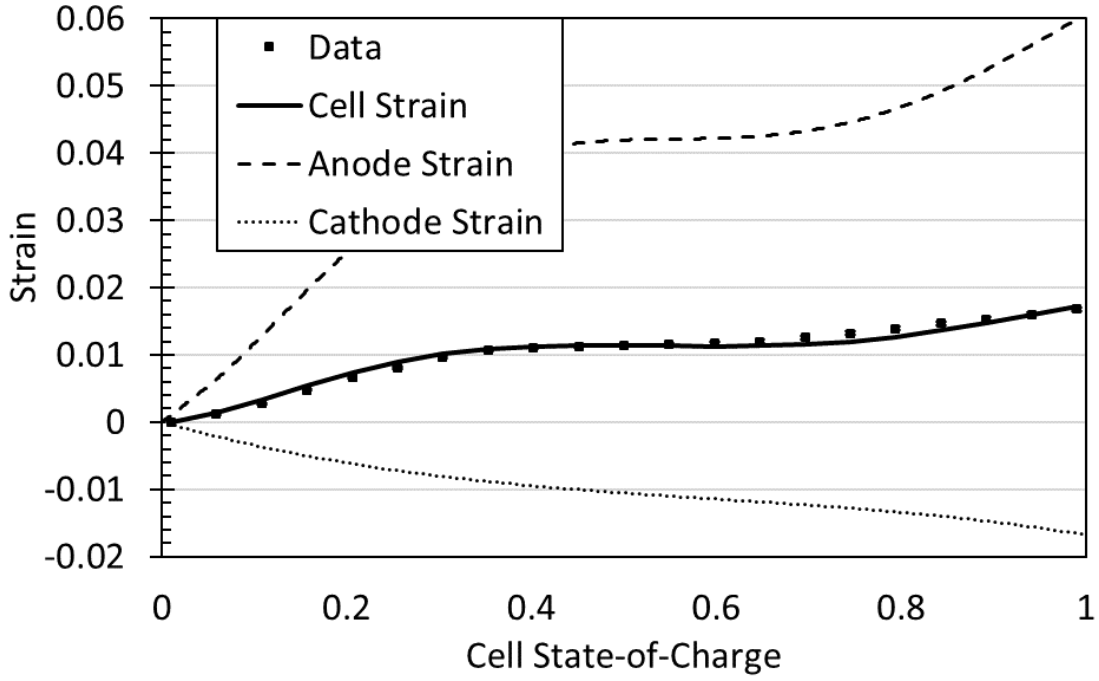

Figure 3.6. Cell, anode layer, and cathode layer strain during simulation of cell discharge.

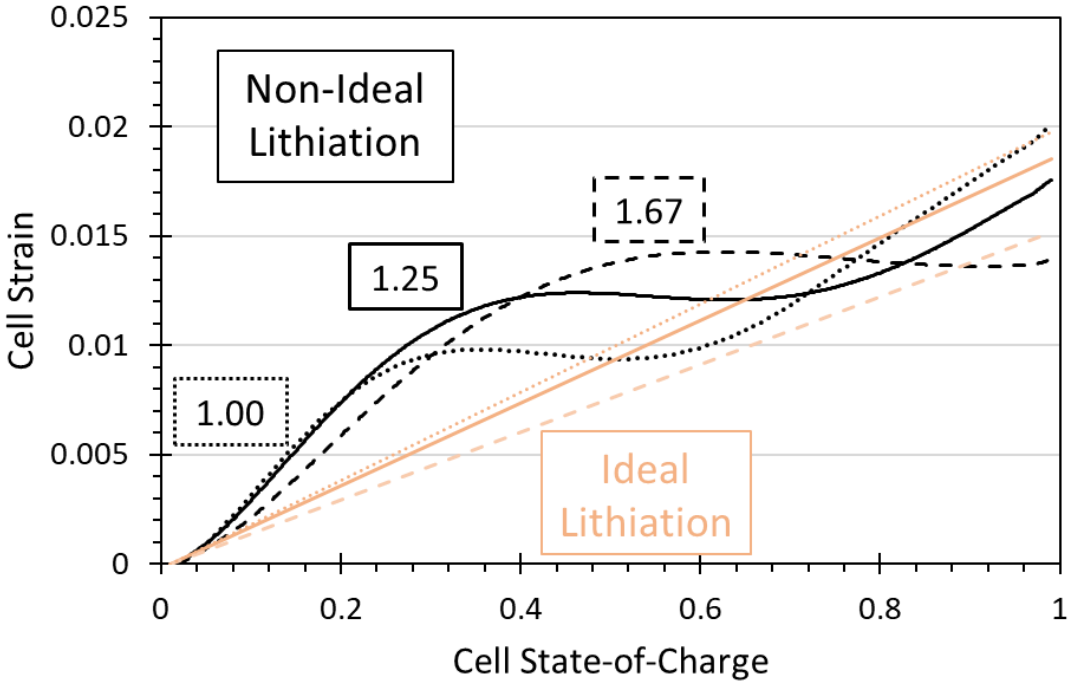

Figure 3.7. Black curves represent low-rate volume change profiles of theoretical NMC/LMO:Graphite pouch cells with modified anode/cathode capacity ratios, 1.00(dotted), 1.25(solid), and 1.67(dashed). Simulations using thermodynamically ideal lithiation-based volume change are shown as peach lines of the respective patterns for comparison.

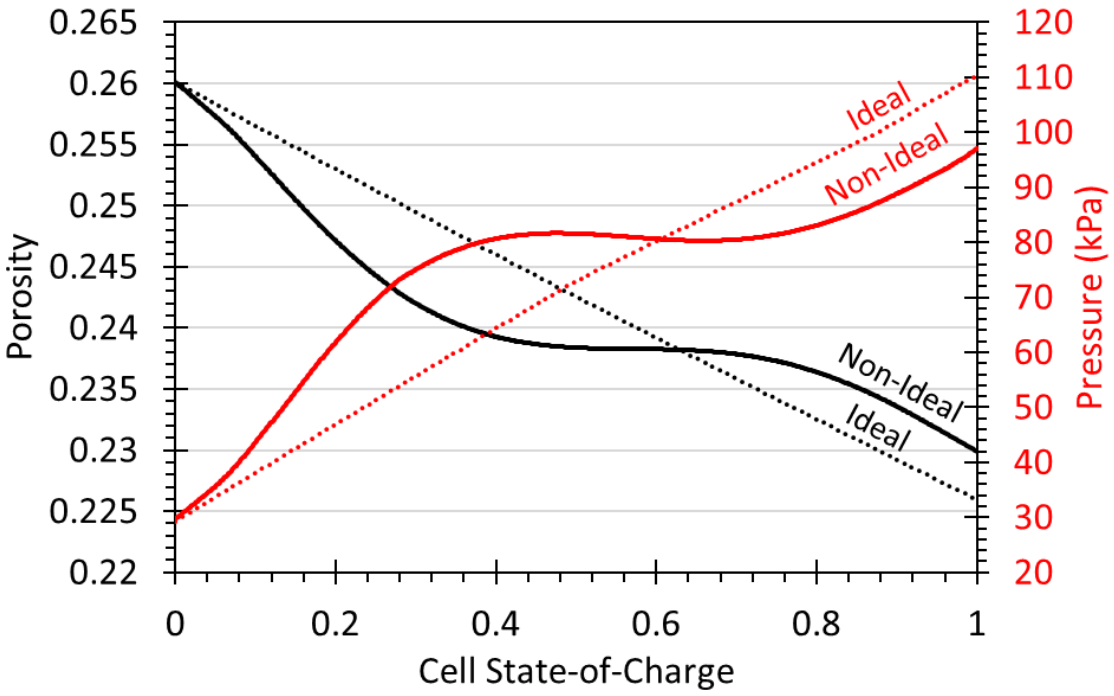

Figure 3.8. Comparison of simulations using non-ideal (solid) and ideal (dotted) volume change to predict porosity change and pressure generation of a pouch cell with foam packaging.

CHAPTER 4

A MECHANO-ELECTROCHEMICAL BATTERY MODEL THAT ACCOUNTS FOR PREFERENTIAL LITHIATION INSIDE BLENDED SILICON GRAPHITE ANODES

This chapter focuses on accounting for the effect of preferential lithiation, which occurs to active materials in blended electrode composites, on mechano-electrochemical behavior. Some results from this work were presented at the Virtual Meeting of the Electrochemical Society in October 2020.(98)

A societal push to utilize clean, renewable energy has encouraged the automotive industry to offer electric vehicles (EVs) in their lineups. However, most currently offered EVs are small- the size of a coupe or sedan. In recent years, automotive sales show that consumers are shifting away from these smaller vehicles and towards larger format vehicles, such as crossovers, sport utility vehicles (SUVs), and trucks.(1) Many companies within the automotive industry are pushing to provide fully electric trucks to the general population, however, certain advancements in technology can lead to improvements in performance and decreases in cost. These metrics to improve are common among all electric vehicles: cost, charging time, battery capacity, and capacity retention. However, when considering a large format vehicle, a sufficient capacity (vehicle range) becomes exponentially more difficult to provide. The larger vehicle size and mass reduces efficiency, and thus, range. More cells can be added to the automotive battery pack to

provide a reasonable range. However, current battery technology is gravimetrically inefficient, so adding more cells will significantly increase vehicle mass, further reducing vehicle efficiency. In many cases, the large-format vehicles will be used for transporting people, tools, or goods, meaning additional capacity will be needed to account for the higher payloads. For these reasons, scientists and engineers look to use more promising chemistries in large-format vehicles' batteries.

Several classes of anode active materials have been proposed in recent years, and silicon has received considerable attention as a result of its high theoretical capacity (4200 mAh/g for $Li_{22}Si_5$).(78) However, developers have not yet been able to realize pure Si anodes with sufficient cycle life for commercial use, due in part to the large volume change that occurs during lithium intercalation.(99) Silicon cycles through at least four stable alloy phases during a charge/discharge cycle, leading to a complete transformation in the crystal structure and a ~400% volume expansion between the fully charged and fully discharged states.(38, 60) The coupled high crystallographic strain and large volume change leads to Si fracturing and pulverization, which detaches Si from the electrode during discharge, rapidly decreasing capacity and electrical contact.(40) In fact, metallurgical silicon loses nearly all of its capacity after only ~10 cycles. To mitigate structural strain, and thus, reduce capacity loss with cycling, designers have employed the use of silicon/graphite (Si/C) composites to incorporate the energy dense silicon active material without excessive expansion.(61, 62) However, it is still poorly understood how stresses develop in the porous structure during cycling, which in turn provides a degree of uncertainty in how materials, electrodes, cells, and ultimately battery packs can be rationally designed to mitigate the effects of volume change inherent in these silicon-based chemistries. A multi-

scale modeling approach shows promise of better understanding these phenomena, as the important couplings of mechanical and electrochemical behavior at the particle, electrode, and cell scales can be simultaneously accounted for.

In consideration of Si/C anodes, Dash and Pannala previously modeled the theoretical capacities of anodes with varying Si/C ratios.(63) In their study, they assumed that the volume of the anode layer would be fixed, and that the active material volume change would only affect the porosity of the composite electrode. Their calculations of capacity assumed that the active materials would expand until the electrode would reach a porosity of 0. Recently, our group employed our previously developed multi-scale model(52-54, 100) that predicts the split between electrode porosity and dimensional changes upon lithiation to expand upon this theoretical study of Si/C electrodes.(59, 76) This study focused on the implementation of a representative volume element (RVE) model to generate realistic mechanical predictions on the cell scale. The accessible capacities of the Si/C electrodes could then be determined using physical limitations of the cell system, such as a maximum pressure limitation or a minimum porosity limitation, where structural limits or performance limits may be exceeded. However, in this previous work, the active material was assumed to mechanically and electrochemically behave as the composition-weighted average of the mixed materials. That is, the equilibrium potential, diffusion behavior, the capacity, and the volume change of the electrode would be a compositional average between the multiple active materials within the same electrode. This assumption may be reasonable for active materials that are significantly mixed using ball-milling/alloying techniques. However, the cheapest, simplest, and most common synthesis of electrodes with multiple active materials involves a simple mixing of

two powders of each active material type in the electrode slurry. Figure 4.1 shows a representation of the electrode matrix that forms when mixing two active material powders. The resulting composite matrix is comprised of separate particles of each active material. The separate active materials will have their own intercalation equilibrium potential, as well as diffusion, kinetic, mechanical, and volume change behaviors. The implication of the mixed-powder type of electrode is that the previous assumption of compositionally-averaged behavior between the two active materials will not account for competing kinetics and the resulting difference in state-of-lithiation and volume change of each active material.

Previously, modeling efforts have been made to represent electrodes matrixes that contain separate active material particles. Gomadam et al. developed a mathematical model that predicts the voltage-capacity behavior of a primary lithium battery containing a hybrid cathode to take advantage of the high energy density of carbon monofluoride and high power-density of silver vanadium oxide.(101) Albertus et al. expanded upon this concept by adapting their previously developed lithium-ion mathematical model to treat multiple types of active materials in a single electrode, including experimental validation of their results.(102) The idea behind these two studies is to treat the active materials separately within the same electrode, meaning there will be competing intercalation kinetics. Therefore, the active materials will lithiate preferentially based on their fundamental electrochemical parameters. Since these initial modeling efforts, more blended-electrode models have been developed with the focus on dynamic electrochemical performance, especially in high power applications.(103, 104) However, most haven't focused on mechanical behavior in the battery. One effort to simulate stress generation due to Li

intercalation was conducted by Dai et al.(57) Their focus was to simulate internal particle stress of blended $LiNi_{0.8}Co_{0.15}Al_{0.05}O_2$ and $LiMn_2O_4$ cathodes to provide indication of where fracturing may occur within the electrode. However, little effort has been made to model blended anodes, to model active materials with large volume change, or to model multi-scale mechano-electrochemical phenomena of blended electrodes.

Therefore, the focus of this study is to understand how preferential lithiation in blended anodes affects coupled mechano-electrochemical behavior. This study was conducted by adapting a previously-developed multi-scale, mechano-electrochemical model to treat the silicon and graphite separately within the same anode. The silicon active material undergoes significantly more volume change than graphite, so the goal of this work is to represent the preferential lithiation of the silicon and graphite in order to improve simulation accuracy of intercalation-driven, volume-change phenomena within the active material particle, the electrode, and the overall cell. Additionally, operation of a cell will be simulated while assuming compositionally averaged behavior of the two active materials, providing a good comparison to the assumptions used in previous mechano-electrochemical modeling of blended anodes.

4.1 MODELING METHOD

The electrochemical governing equations used in this study come from porous electrode theory, with adaptations to account for multiple active materials within the same electrode. Figure 4.2 depicts the model geometry used in this study. To briefly summarize, the electrochemical model is a modified Newman-type, Pseudo-Two Dimensional (P2D) model, where the first dimension represents the thickness of the electrochemical cell (x-axis in Figure 4.2), and the pseudo-second dimension represents the radial direction of a

spherical active material particle (r-axis in Figure 4.2). The key difference from previous geometries is that there are now two separate radial dimensions in the anode, representing the spherical silicon and graphite active material particles. Previously, Albertus et al. adapted a P2D model to treat two active materials within the same cathode.(102) In the study shown here, a similar approach was taken to represent the silicon and graphite active material particles in a blended anode.

The treatment of the two active materials using separate pseudo-second (particle radius) dimensions has electrochemical implications. First, solid phase transport of Li^+ will differ between the two materials because they will have their own diffusion coefficients, as noted in literature.(105, 106) A material with significantly slower solid-phase transport will have more performance limitations than a material with faster transport; so higher-rate operation may cause a different Li^+ concentration gradient between the two materials and impact cell performance. However, a more important implication is the effect of the differing intercalation reaction equilibrium potentials between the two active materials. Figure 4.3 shows the equilibrium potential of silicon and graphite.(49, 107) It is evident that for the majority of the lithiation ranges of the two active materials, the silicon has a higher equilibrium potential. Therefore, it is expected that as a charge current is applied, the silicon would preferentially lithiate first, based on the overpotential, η_i, at the surface of the active material particle:

$$\eta_{AM} = \phi_{1,i} - \phi_{2,i} - U_{AM} \qquad [4.1]$$

Another way to phrase this phenomenon is that the two active material particles will have competing Butler-Volmer kinetics.(24)

$$j_{AM} = Fk_{AM}^{(\alpha_{a,AM}+\alpha_{c,AM})}\left(c_{s,AM,max} - c_i\right)^{\alpha_{c,AM}} c_i^{\alpha_{a,AM}}$$
$$\cdot\left[exp\left(\frac{\alpha_{a,AM}n_{AM}F}{RT}\eta_{AM}\right) - exp\left(-\frac{\alpha_{c,AM}n_{AM}F}{RT}\eta_{AM}\right)\right] \quad [4.2]$$

The Butler-Volmer expressions will differ in concentration, c_i, maximum solid concentration, $c_{s,AM,max}$, rate constant, k_{AM}, and overpotential, η_i, for each active material. This difference will drive how much of the applied current will go into lithiation/delithiation of either active material. Accounting for preferential lithiation of the active materials is important to consider, as the active material lithiation is directly connected to the volume change behavior of the two active materials.

The fundamental governing equations and general construction of the coupled mechano-electrochemical model used for this study has been described in previous work.(52-54, 59, 76, 100) Some of the key concepts and equations will be described again in order to better illustrate how the model is adapted for mechano-electrochemical simulation of blended anodes. During charging and discharging, Li^+ ions move from the cathode to the anode and from the anode to the cathode, respectively. The lithiation and de-lithiation of the anode and cathode lead to active material volume change. As shown previously, the volume change phenomena are based on the electrode material balance governing equation shown below:

$$\frac{\partial\,(1-\varepsilon_i)}{\partial \mathrm{t}} + (1-\varepsilon_i)\frac{\partial\,\varphi_i}{\partial \mathrm{t}} = -\frac{s_i\Delta\hat{V}_i}{n_iF}J_i \quad [4.3]$$

The right side of the equal sign represents the volume change due to the intercalation or de-intercalation of Li^+ in the electrode active material. This volume change either causes change in the electrode layer dimensions (second term on the left) or change

in electrode porosity (first term on the left). J_i, is the variable that links the volume change behavior to electrochemical kinetics, and thus, the rest of the electrochemical and transport phenomena within the anode, cathode, and separator. Previously, an averaged volume change behavior and single intercalation rate was considered, where in this study, the focus is to account for the separate intercalation-based volume change of both active materials in the blended anode. Therefore, Equation [4.3] is modified:

$$\frac{\partial\,(1-\varepsilon_n)}{\partial \mathrm{t}} + (1-\varepsilon_n)\frac{\partial\,\varphi_n}{\partial \mathrm{t}} = \; -\sum \frac{s_{AM}\Delta\widehat{V}_{AM}}{n_{AM}F} J_{AM} \qquad [4.4]$$

The intercalation-based volume change term is now a sum of the two blended anode materials, which each have their own intercalation rate and molar volume.

$$\sum \frac{s_{AM}\Delta\widehat{V}_{AM}}{n_{AM}F} J_i = \; \frac{s_{Si}\Delta\widehat{V}_{Si}}{n_{Si}F} J_{Si} + \; \frac{s_C\Delta\widehat{V}_C}{n_CF} J_C \qquad [4.5]$$

Equation [4.5] represents how the intercalation-driven volume change contributes to changes in electrode dimensions or porosity. However, to accurately represent mechanical phenomena of the electrode, the mechanics of all cell components must be accounted for. In previous work(59), a representative volume element (RVE) model was incorporated to produce realistic simulations of pressure, porosity, and component strain. In this study, a similar approach will be used. Figure 2 shows all the mechanical elements for consideration in the RVE model. For the solid-metal current collectors, linear elastic mechanics is assumed:

$$\varphi_i = \frac{P}{E_i} \qquad [4.6]$$

Previously, the porous components in the cell (anode, separator, cathode, and a foam packaging) were assumed to have a compressive response to pressure that followed an interpolation function of measured data from literature, and the importance of accounting for the compressibility of a foam packaging or casing was shown.(59) In this study, the same interpolation was used for the separator, cathode, and foam packaging:

$$\varphi_{mech,i} = -f_i(P) \quad [4.7]$$

It has been shown that the active materials' modulus will change with lithiation fraction, τ_i.(108) As mentioned previously, in the blended anode, the two active materials will lithiate preferentially. Therefore, to appropriately account for both active materials' changing moduli, the compressive response to pressure in the blended anode is changed:

$$\varphi_{mech,n} = -\sum \varepsilon_{AM} \frac{P}{E_{AM}(\tau_{AM})} = -\varepsilon_c \frac{P}{E_c(\tau_c)} - \varepsilon_{Si} \frac{P}{E_{Si}(\tau_{Si})} - \varepsilon_f \frac{P}{E_f} \quad [4.8]$$

The anode and cathode will have an additional contribution to their strain, coming from the intercalation-driven volume change. From previous work, it was shown that accounting for the thermodynamically, non-ideal volume change is important to accurately simulate mechano-electrochemical phenomena on the electrode and cell scales.(76) Therefore, the measured non-ideal volume change ratios, $\frac{\Delta \hat{V}_i}{\hat{V}^0{}_i}(\tau_i)$, are incorporated from literature to accurately represent the volume change's dependence on active material state of lithiation, τ_i. For the blended anode, the intercalation-driven strain contribution will be modified to be the sum of the two active materials' contributions:

$$\varphi_{int} = \frac{\Delta \hat{V}_n}{\hat{V}^0{}_n}(\tau_n) = \sum \left(\frac{\Delta \hat{V}_{AM}}{\hat{V}^0{}_{AM}}(\tau_{AM}) * \frac{\varepsilon^0_{AM}}{\varepsilon^0_{AM,total}} \right) \quad [4.9]$$

The overall strain of the anode and cathode is calculated as the sum of the compressive strain and the intercalation-driven strain.

$$\varphi_i = \varphi_{mech,i} + \varphi_{int,i} \quad [4.10]$$

In summary, it is assumed that each component in the cell will experience the same stress in the thickness direction of the cell (x-axis in Fig. 4.2). This pressure variable, along with each component's strain response, which is described by a data-driven interpolation, Eq. [4.6], or Eq. [4.10], is what links each individual component strain. Then, as the electrode active materials expand and contract upon cell operation (linked to electrochemical operation by Eq. [4.4]), changes in electrode dimensions, pressure, and porosity will occur. The changing diffusion length of the liquid phase is inherently accounted for using the provided model equations. But the changing diffusion length of the pseudo-dimensions of the spherical active material particles must be explicitly defined. Therefore, the active material particle radius is linked to its state-of-lithiation-dependent volume change ratio.

$$R_{AM} = \frac{3R^0_{AM}}{4\pi} * \left[\frac{\Delta\hat{V}_{AM}}{\hat{V}^0{}_{AM}}(\tau_{AM})\right]^{1/3} \quad [4.11]$$

In this study, we specifically focus on the differences to mechano-electrochemical behavior when treating active materials separately within the same electrode. Simulations from a model with the former assumption that the anode particle would behave as a compositional average of the two blended materials were made for comparison. The two modeling theories may also show some insight to the differences between manufacturing

methods: electrode synthesis by mixing powders of two active materials and electrode synthesis using significantly mixed particles or even alloyed particles.

4.2 RESULTS AND DISCUSSION

Simulation Setup and Inputs:

The model was written in COMSOL Multiphysics Version 4.4 using the Partial Differential Equations (PDE) interface to incorporate the governing equations for the physics, as described in the "Modeling Method" section. Cell operation was simulated with the Time Dependent Solver tool; the governing PDEs were solved using an iterative, numerical solver method. Figure 4.2 depicts the model geometry, with the unit cell shown for electrochemical simulation and the summary of all cell components, including the packing, shown for the RVE mechanical model.

To accurately represent the mechanical behavior inside the RVE geometry, strain responses for the anode, cathode, and separator were taken from literature.(64, 65, 72, 109) The copper anode and aluminum cathode current collectors were assumed to follow linear elastic mechanics, Equation [4.6] with their Young's Moduli being obtained from literature.(73) These stress-strain responses were used to determine the component level strain as a function of cell face pressure. In this study, an initial pressure, 30 kPa, was applied. This initial pressure is relevant to automotive pouch cell stacks, where its application ensures good thermal and electrochemical contact.

In a previous modeling study, the incorporation of non-linear, lithiation-based volume change profiles for the anode and cathode was shown to increase model accuracy. Therefore, the volume change profiles for graphite, silicon, and NMC will also be

incorporated. Figure 4.4 shows the volume change ratio (active material volume divided by the de-lithiated volume) as a function of state-of-lithiation, from 0 to 1. Figure 4.4 shows both measured data from literature and the polynomial fit of the data to be used as a model input.(88, 90) One of the key features to point out is in the graphite volume change profile. Graphite exhibits a particularly unique lithiation phase, which is evident in Figure 4.4a at the lithiation fraction range of 0.25 to 0.5. There, the graphite is said to transition to a "liquid-like" 2L phase, where the graphite undergoes very little volume change upon lithiation. This phase is a defining feature in the graphite expansion profile and will be referred to as the "plateau" in the graphite volume change profile. This plateau will help to identify graphite's contribution to the blended-electrode mechanics. Silicon, Figure 4.4b, doesn't have any significant features like the graphite, as its profile shows a mostly linear volume change behavior with lithiation fraction. However, even small amounts of silicon will significantly impact cell mechanics due to its higher volume change ratio. For the NMC in the cathode, volume change profiles were not readily available in literature. However, Nam et al. previously conducted a study using in-situ X-ray diffraction (XRD) to study blended NMC/LMO cathodes during charge and discharge cycles.(89) Their study was unique in that they had the ability to differentiate between the layered (NMC) and spinel (LMO) phases in the resulting XRD data. With this information, they could separately calculate just the unit cell volumes for NMC as a function of cell charge in a functional voltage range, 2.5 to 3.2V. In this study the assumption was made that the unit cell volumes could translate to the active material volume expansion to derive the volume change profile for NMC.

The model was populated with relevant parameters to represent the Silicon/Graphite:NMC cell. Table 4.1 lists all relevant parameters that were used in the mechano-electrochemical model; they were measured, taken from the COMSOL material database, or taken from literature. To maintain a capacity balance between the anode and the cathode, the initial anode thickness, $L_{n,0}$, was varied to match the cathode capacity. That is, as silicon composition is increased in the anode, the anode thickness would be decreased to maintain the same N:P capacity ratio. For the model that treats the active materials separately, which will be referred to as the "Separate-Particle Model", each material will have its own parameters or coefficients from Table 4.1. For the model that treats the two materials as a single, mixed particle, which will be referred to as the "Averaged-Particle Model", the parameters or coefficients, β, become a compositional average between the two materials:

$$\beta_{average} = \sum \beta_{AM} * \frac{\varepsilon_{AM}}{\varepsilon_{AM,total}} \quad [4.12]$$

This compositional averaging is used for diffusion coefficients, kinetic coefficients, volume change behavior, and equilibrium potential. This methodology provides comparison to a previously used modeling method(59) as well as comparison to manufacturing methods where the resulting active material particles are alloyed or well-mixed. With the parameters input, the model was ready for cell simulation.

To run the simulation, the model was initialized to set the cell at a fully-discharged state, where graphite and silicon were set to a lithiation fraction of 0.75 and 1, respectively. These lithiation fractions are chosen based the active materials' equilibrium potentials at the fully-discharged cell voltage. Then, a constant-rate charge was simulated using a cell

voltage cutoff window that is relevant to automotive battery applications, between 2.5 and 3.2V. This simulation was run at varied compositions of silicon (5%, 10%, 15%, and 20%) and at varied rates (C/10, C/4, C/2, 1C, 2C, and 3C, where C represents the rate needed to fully discharge the cell in one hour).

Preferential Lithiation/Delithiation:

The preferential lithiation/delithiation of the graphite and silicon plays an important role in electrochemical simulation. In an electrode composed of a single active material, binder, and conductive additive, the open circuit voltage of the electrode follows the intercalation equilibrium potential as a function of state-of-lithiation for that material. Therefore, battery algorithm engineers could appropriately predict cell state-of-charge through the use of the anode and cathode materials' equilibrium potentials and lithiation fraction ranges combined with some form of Kalman filter.(110-112) In a blended electrode, the competing kinetics and differing equilibrium potentials within the same electrode complicate how cell voltage can be used to predict state-of-charge and state-of-life. Figure 4.5 shows the open circuit voltage of the cell (Fig. 4.5a) and the anode (Fig. 4.5b). as a function of the cell state-of-charge for electrodes with varying silicon compositions. As silicon composition is increased, the open circuit voltage changes in accordance to the ratio of the materials and the previously described preferential lithiation.

Accurately predicting electrode and cell voltage is imperative for engineers who develop battery management systems. However, looking at the individual active material state-of-lithiation throughout the cycle at different conditions gives a better idea of how the two materials' kinetics are competing. Figure 4.6 shows the simulated active material

average state-of-lithiation as a function of cell charge capacity from the separate-particle and averaged-particle models. From Figure 4.6, we confirm silicon significantly lithiates before the graphite, which is expected due to the relatively lower equilibrium potential of the graphite. The dashed lines in Figure 4.6 show the uniform lithiation of the averaged-particle model for comparison. The significant difference between the two simulations gives reason to see how preferential lithiation can significantly affect electrochemical and volume change behavior of the electrode.

Figure 4.6a shows the effect of C-rate on the preferential lithiation of the active materials, where the arrows represent increasing C-rate. It is seen that as C-rate is increased, the state-of-lithiation of the two active materials move closer to each other. The slower solid-phase diffusion and de-intercalation kinetics become limiting at higher C-rates, driving the intercalation overpotential to increase. The result is that the overpotential becomes high enough to lithiate graphite earlier in the charge. However, in Figure 4.6a, it is clear that rate doesn't significantly impact preferential lithiation until reaching high rates.

Figure 4.6b shows the effect of Si/C composition on the preferential lithiation of the two active materials, where the arrows represent increasing silicon composition. The total amount of lithiation sites are maintained in the anode to keep the capacity balance between the anode and cathode constant. That is, as the silicon composition increases, the graphite composition and electrode thickness decreases. The result of increasing silicon composition is that it will accept more charge, or Li^+ intercalation. Because silicon preferentially lithiates due to its higher overpotential, the graphite lithiation will occur later in the charge cycle with increasing silicon composition. With these clear results indicating preferential lithiation, its effects on volume change phenomena can be observed.

Anode Strain and Porosity- the Broader Impacts on Electrode Behavior:

The blended anode active materials have significantly different volume change behavior and magnitude, graphite with a single particle expansion of ~10% and silicon with a single particle expansion of ~280% for this state-of-charge window.(88, 90) Therefore, it is expected that preferential lithiation will significantly impact how mechano-electrochemical variables, strain and porosity, change during cell operation. Figure 4.7 shows the anode strain as a function of charge capacity at varied rates. It is evident that the simulation of anode strain significantly differs between the separate and averaged particle models, including the total strain when fully charged to 3.2V. When assuming uniform lithiation, both the graphite and the silicon will be charged and contribute to the volume change equally until reaching the 3.2V charge cutoff. When accounting for the competing kinetics, the preferential lithiation shows that silicon starts at a higher state-of-lithiation at 2.5V and doesn't experience the full lithiation that the graphite active material does. Therefore, the prescribed operation condition shows less anode strain from 2.5 to 3.2V. The averaged-particle model assuming uniform lithiation is fed by a measurement of the electrode's open circuit voltage for simulation, therefore, the strain is simply a compositionally-averaged volume change profile, dependent on state-of-lithiation. Also confirmed in Figure 4.7 is that rate does not significantly affect the strain profile before becoming electrochemically limiting. Therefore, the primary impact on mechano-electrochemical phenomena will be the differing equilibrium potentials of the two materials and the electrode composition.

Equation [4.4] describes how the lithiation-based volume change affects either the dimensions (thickness) of the electrode or porosity of the electrode. Figure 4.8 shows the

porosity of the electrode as a function of charge capacity for a 5% silicon anode being charged at C/10. From Figure 4.8, as the cell is charged, the increased volume and pressure leads to a decreasing porosity. The dotted line shows the previously-assumed averaged particle model for comparison. There is quite a noticeable difference in porosity between the two simulations, which primarily occurs due to the preferential lithiation of the active materials as well as their lithiation ranges in the operational 2.5-3.2V window. Additionally, due to the differing lithiation ranges of the two materials, the beginning and ending porosity differ as well. This information is important for cell manufacturers to understand how the material lithiation settles after conducting cell formation cycles and setting specific voltage windows.

Porosity plays an important role in the liquid-phase transport of Li^+. However, the change in porosity is not the only impact on ionic transport. As the anode is lithiated and de-lithiated, the total thickness of the anode is changing, which also effects diffusion length. To see how both porosity (effective diffusion) and anode strain affect cell performance, the simulation outputs were used in an explicitly defined equation for diffusion transport resistance in the liquid phase of the anode.(113)

$$R_e = \frac{\Gamma_2 RTL_n}{\epsilon_n F^2 D_{electrolyte} c_0} \quad [4.13]$$

Figure 4.9 shows the resulting electrode resistance as a function of state-of-charge. The separate particle simulation, shown as a black solid line, experiences higher resistance early in the charge process. This follows the trend of the higher volume change silicon preferentially lithiating first. This means that the electrode thickness is increasing and the porosity is decreasing faster when silicon is lithiating more than graphite. However, at the

higher state-of-charge, graphite is primarily lithiating, meaning a lower impacts from volume change. At this point, the averaged-particle model volume change overtakes the volume change seen from the separate particle model, because the silicon and graphite are lithiating uniformly. Again, the starting and ending resistances do not align due to the differing lithiation ranges of the individual active materials.

These types of information may be important to cell designers working to develop a cell for high-power applications where diffusion can limit cell performance. Similarly, understanding the impact of preferential lithiation on high strain regions of both materials may better inform modelers who hope to simulate anode and cathode mechanical degradation in order to better understand capacity fade. This type of comprehensive model that accounts for the impact of particle-scale behavior, including preferential lithiation, shows promise to not only better understand blended-electrode behavior, but also to aid in the design of new, advanced electrodes containing multiple active materials.

4.3 CONCLUSIONS

A multi-scale mechano-electrochemical modeling method was shown that simulates behavior of batteries that contain blended Si/C anodes. The model development included an adaptation to treat active materials within the same electrode separately, which is more representative of electrodes that are manufactured by simply blending active material powders in the electrode slurry. That is, separate representative particles will display the specific electrochemical behavior of each active material. Concurrently, a model was run that assumes a compositionally-averaged behavior of the blended active

materials. This is a commonly used assumption is possibly more representative of active materials that are well-mixed or even alloyed in each particle.

One of the primary insights gained from this study is the understanding of how active materials will preferentially lithiate. The differing electrochemical parameters, primarily equilibrium potential, will dictate the rate at which active materials lithiate within the same electrode. From this study, it is shown that silicon will preferentially lithiate first and de-lithiate last when mixed with graphitic carbon. This has a significant impact on battery algorithms engineers who often rely on open circuit voltages for state-of-charge or state-of-life prediction. Simulating preferential lithiation not only yields a better understanding of electrochemical performance. Due to silicon's significantly higher volume change, the overall electrode and cell mechanical behavior are impacted by the preferential lithiation as well.

As more materials with high lithiation-based volume change are considered, the need to simultaneously account for mechanical and electrochemical phenomena increases. Treating the active materials separately and predicting the preferential active material lithiation impact on both mechanical and electrochemical phenomena shows promise as a tool for designers who are developing batteries with blended electrodes. The insights that were gained from this study not only help to understand how mechanical behavior and electrochemical performance manifest within blended electrodes, but also may prove useful to engineers looking to understand, predict, and ultimately mitigate electrode degradation.

4.4 TABLES AND FIGURES

Table 4.1. List of design parameters used in the mechano-electrochemical model simulation and analysis.

Parameter	Source	Value
$L_{ncc,0}$	assumed	1.0E-5 m
$L_{n,0}$	calculated	Composition-dependent to have an N:P ratio of 1:1
$L_{sep,0}$	assumed	2.0E-5 m
$L_{p,0}$	assumed	10E-5 m
$L_{pcc,0}$	assumed	2.0E-5 m
$R_{C,0}$	assumed	2.5E-6 m
$R_{Si,0}$	assumed	2.5E-6 m
$R_{NMC,0}$	assumed	2.5E-6 m
k_C	assumed	2.54E-9 m s^{-1}
k_{Si}	assumed	2.0E-9 m s^{-1}
$c_{s,\max,C}$	COMSOL Material Spec.	31,507 mol m^{-3}
$c_{s,\max,Si}$	COMSOL Material Spec.	2.78E5 mol m^{-3}
ε_n^0	assumed	0.35
ε_{sep}^0	assumed	0.4
ε_p^0	assumed	0.35
$\varepsilon_{f,n}^0$	assumed	0.1
$\varepsilon_{f,p}^0$	assumed	0.1
$\varepsilon_{AM,n}^0$	calculated	1-ε_n-$\varepsilon_{f,n}$
$\varepsilon_{AM,p}^0$	calculated	1-ε_p-$\varepsilon_{f,p}$
R	known	8.314 J mol^{-1} K^{-1}
F	known	96485 C mol^{-1}
T	assumed	298.15 K
c_0	COMSOL Material Spec.	1000 mol m^{-3}
$D_{electrolyte}$	COMSOL Material Spec.	2E-10 m^2 s^{-1}
$\overline{D_{s,C}}$	assumed(114)	2.0E-14 m^2 s^{-1}
$\overline{D_{s,Si}}$	assumed(115)	1.0E-12 m^2 s^{-1}
$D_{s,p}$	COMSOL Material Spec.	5.0E-13 m^2 s^{-1}
$\alpha_{a,n}$	assumed (57)	0.5
$\alpha_{c,n}$	assumed (57)	0.5
$\alpha_{a,p}$	assumed (57)	0.5
$\alpha_{c,p}$	assumed (57)	0.5

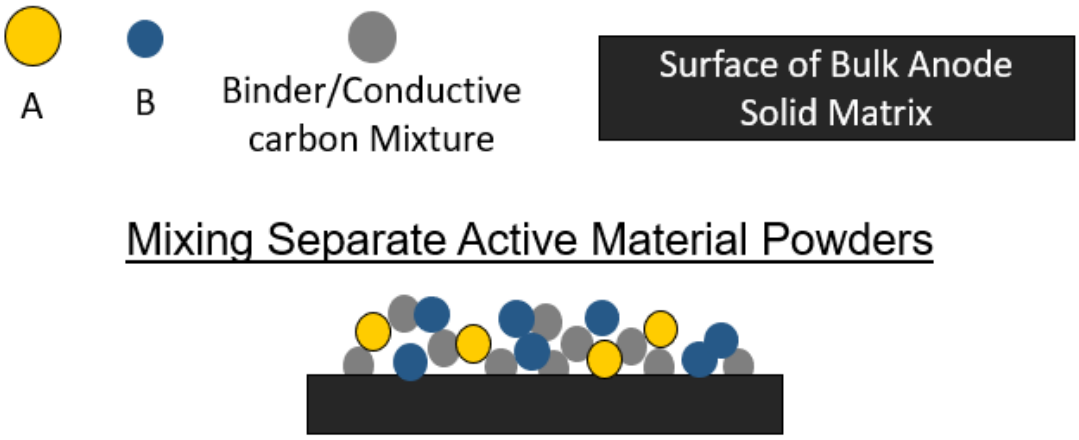

Figure 4.1. Depiction of electrode matrix when mixing two active material powders into an electrode slurry.

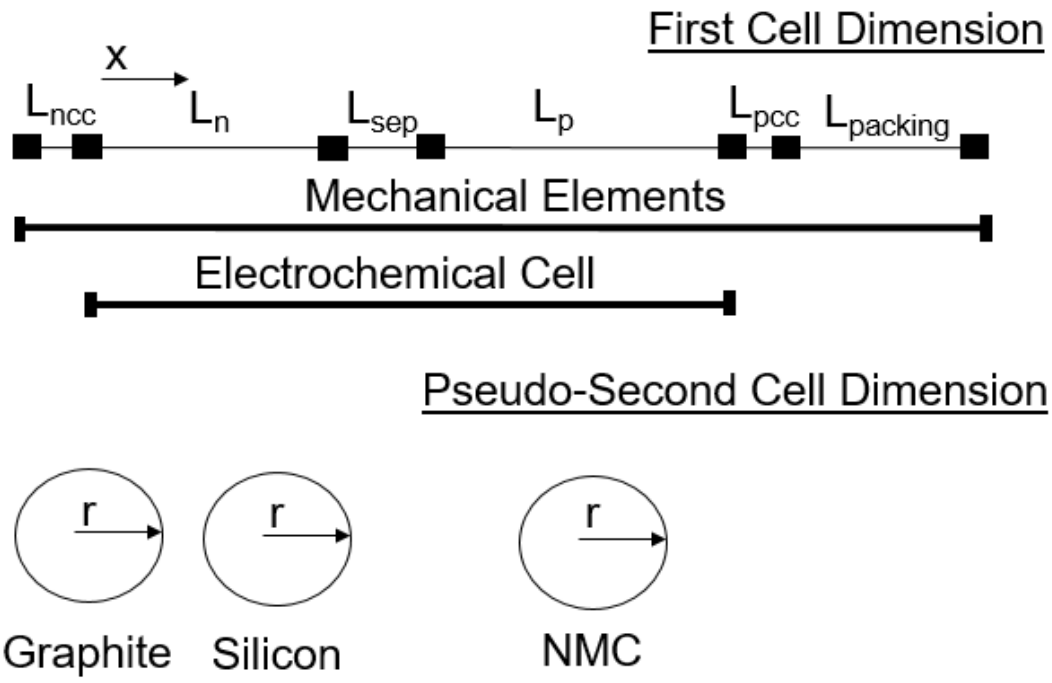

Figure 4.2. Depiction of the model geometry used in this modeling study. The anode in this study is blended silicon-graphite, therefore, two pseudo-second dimensions represent the radial direction in spherical coordinates of the two active material particle types in the anode.

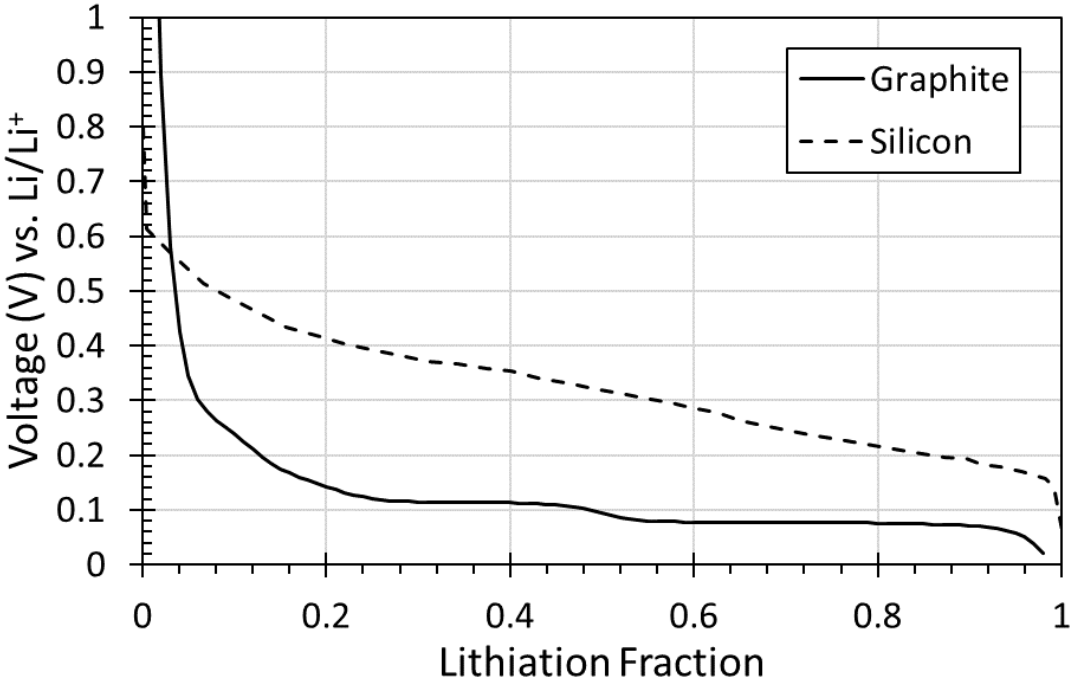

Figure 4.3. Equilibrium potential of the Li^+ intercalation reaction for both graphite and silicon as a function of lithiation fraction. (49, 107)

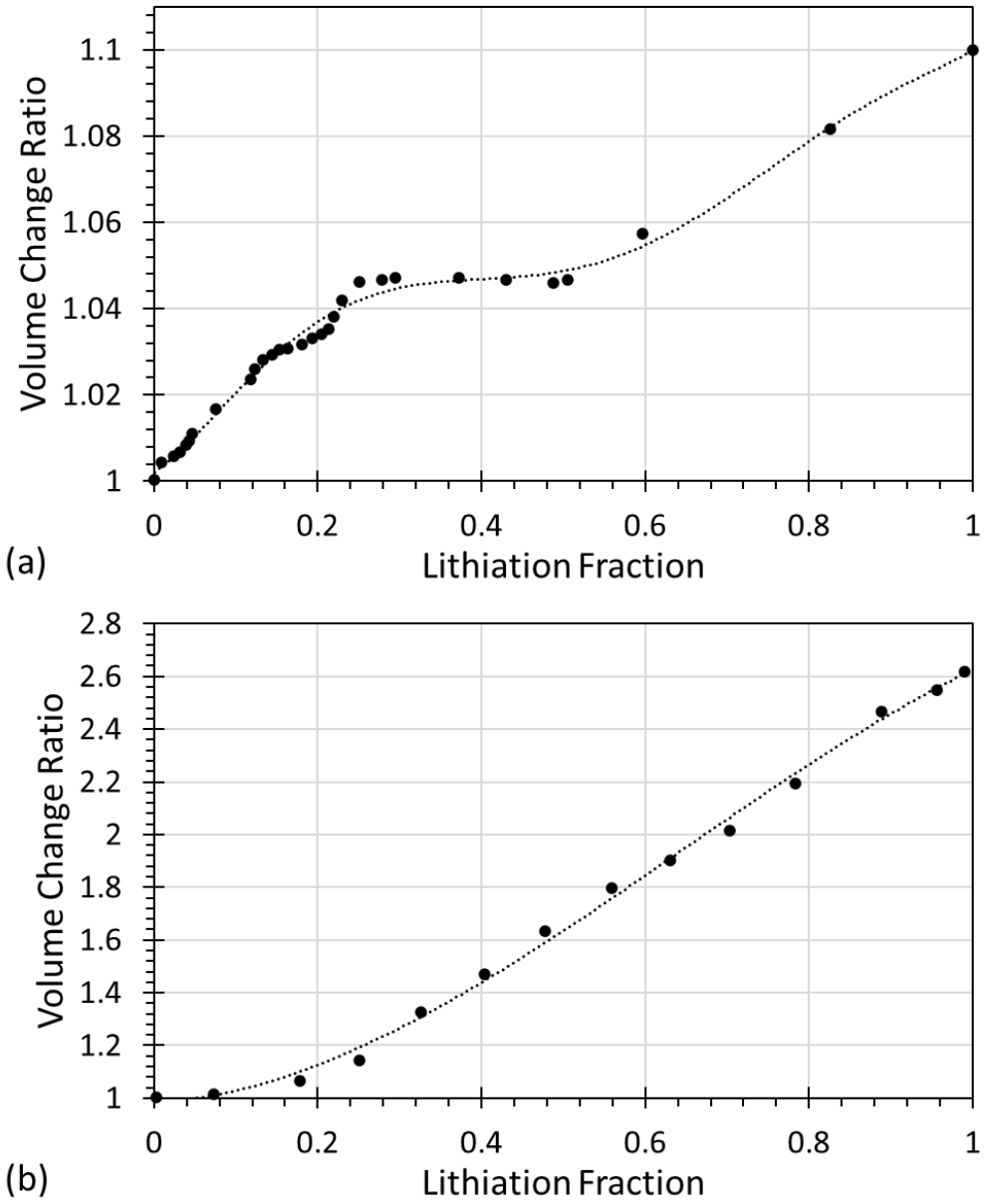

Figure 4.4. The volume change ratio of (a) graphite and (b) silicon with respect to lithiation fraction. Polynomial fits used as model inputs are shown as black dotted curves. (88, 90)

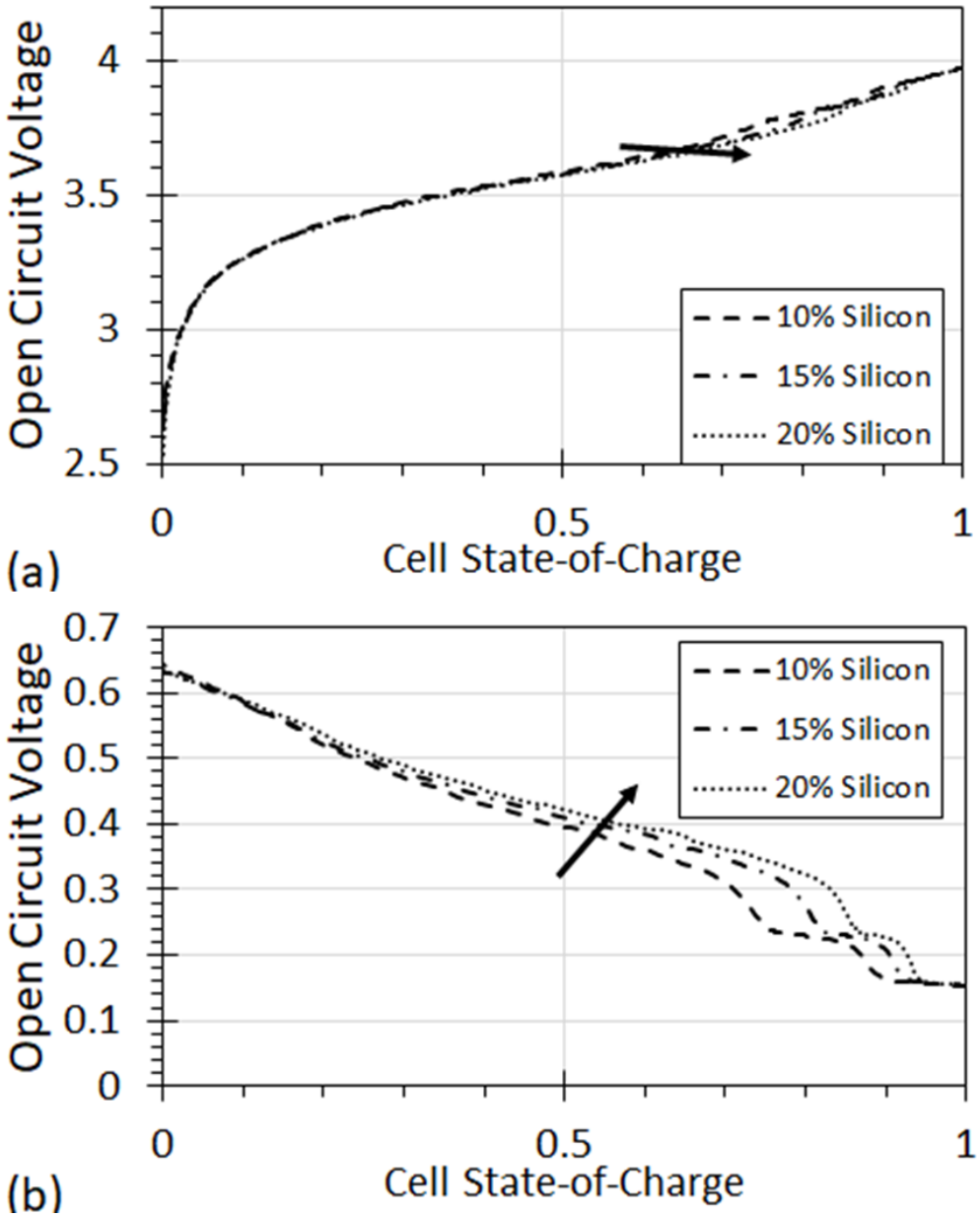

Figure 4.5. The open circuit voltage of a (a) cell and (b) anode using a blended silicon-graphite composite for the anode.

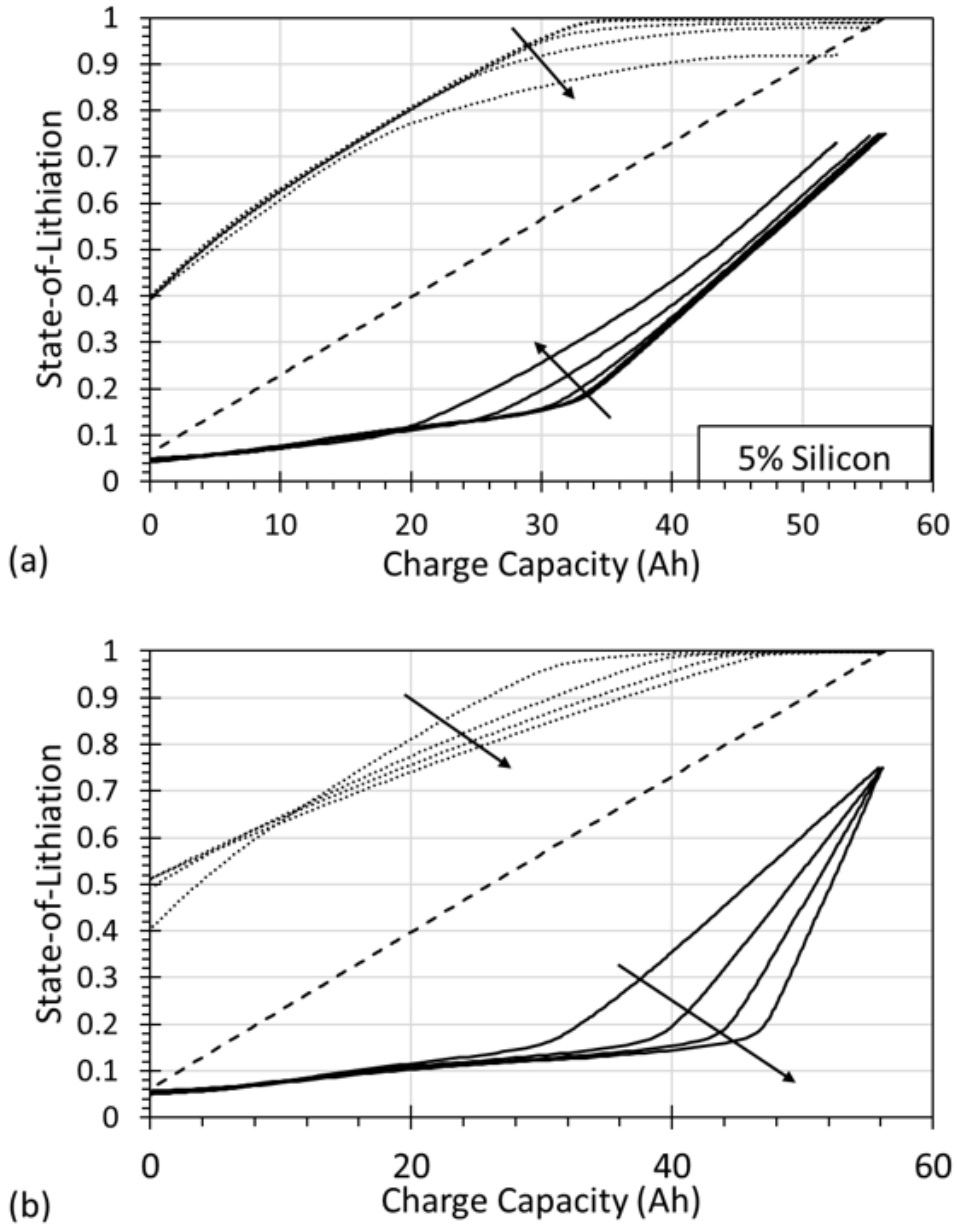

Figure 4.6. State-of-lithiation of graphite (solid) and silicon (dots) as a function of cell charge capacity for the separate-particle model. The arrows in (a) indicate increasing rate (C/10, C/4, C/2, 1C, 2C, and 3C) while the arrows in (b) indicate increasing silicon composition (5%, 10%, 15%, and 20%). The dashed line shows uniform lithiation for reference.

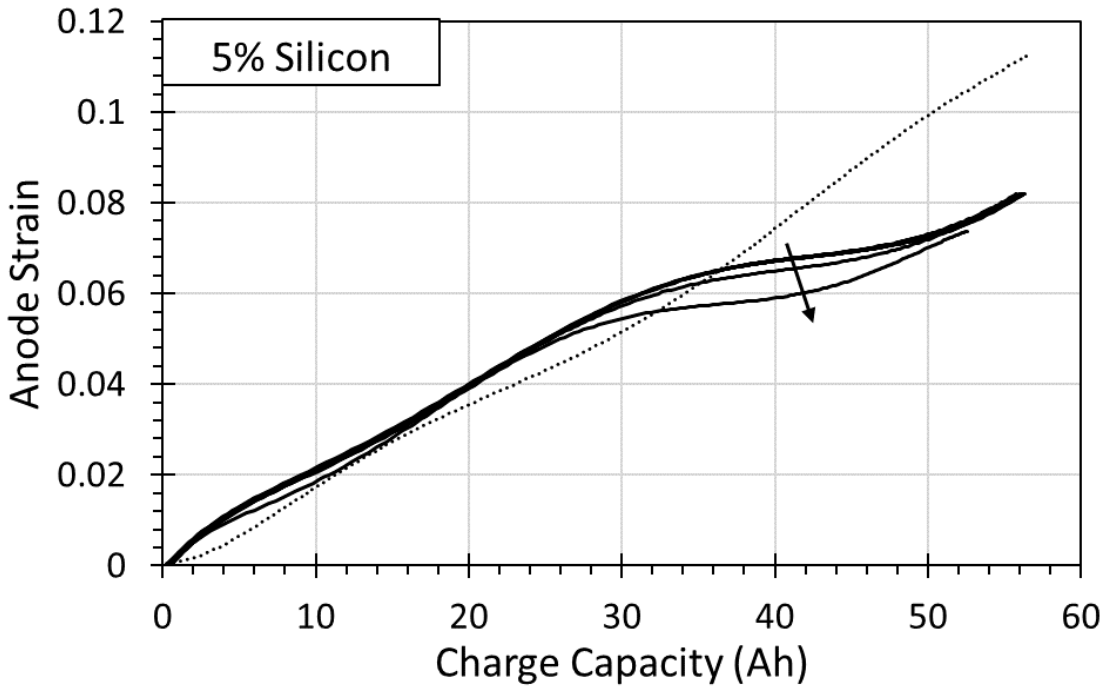

Figure 4.7. Simulation of anode strain as a function of charge capacity at varied C-rates. The arrow indicates increasing C-rates from C/10 to 3C. The dotted line represents the result from an averaged particle model for comparison.

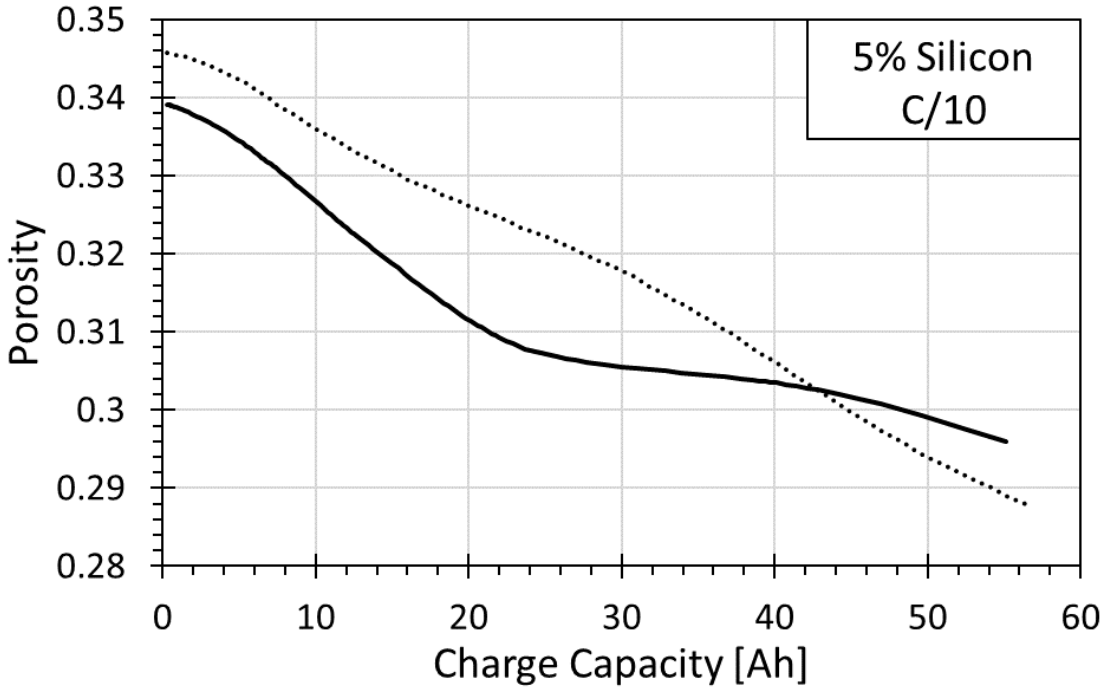

Figure 4.8. Anode porosity from the separate-particle (solid) and averaged-particle (dotted) models as a function of discharge capacity for a 5% silicon anode being discharged at a rate of C/10.

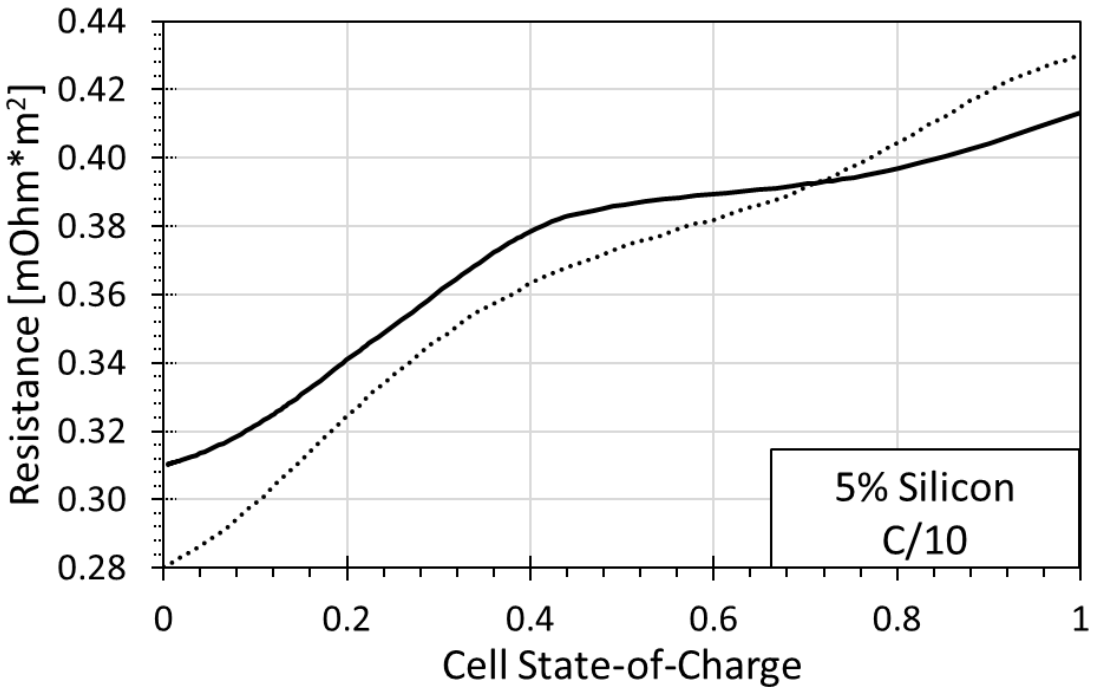

Figure 4.9. Resistance as a function of state-of-charge for a blended Si/C anode using a separate (solid) and averaged (dotted) particle model.

CHAPTER 5

CONCLUSIONS

The studies presented in this dissertation address the increasingly important connections between mechanical and electrochemical phenomena at the particle, electrode, cell, and pack scales. A multi-scale modeling approach was the most suitable tool to address these coupled phenomena due to the difficulty in simultaneous observation of each scale. The model developments of interest here include: (1) A representative volume element model was incorporated into standard battery models to generate realistic predictions of mechanical behavior in the battery cell and pack. (2) Thermodynamically non-ideal, lithiation-based volume change behavior of the active materials was accounted for in the model, leading to higher accuracy in simulations of pressure and cell strain and a stronger understanding of how anode/cathode capacity balance impacts volume change. And (3) a mechano-electrochemical model of a blended electrode was developed, bringing a better understanding of how active materials preferentially lithiate and the resulting effects on mechano-electrochemical behavior of the cell.

When incorporating a representative volume element model into a standard P2D-type model, realistic simulations of changing variables, such as pressure and porosity, were presented for the first time. The value here is that the RVE model and P2D model will take advantage of the same geometry, representing 1D in the through-plane direction of the cell. One key finding from this study is how much the most mechanically compliant component,

often a foam packaging in automotive modules, will impact pressure generation in the battery. This mechano-electrochemical model was used to illustrate how other features in the cell, such as component thicknesses, electrode/electrolyte chemistries, and packing thickness/materials would impact mechano-electrochemical behavior of the cell.

Next, non-ideal lithiation-based volume change profiles for the electrode active materials were incorporated into a previously developed mechano-electrochemical model. Then, the cell-level simulation was validated with measured pouch cell electrochemical performance data and thickness change data during low-rate discharge. To measure thickness change as a function of state-of-charge, a unique apparatus was set up to maintain a constant cell face pressure, measure the thickness change of the pouch cell, and electrochemically operate the cell. The model predictions proved to agree with the experimentally measured data and captured the primary feature of the volume change profile, the graphite 2L phase. The increased accuracy of the model using non-ideal lithiation behavior shows the importance of accounting for individual active material volume change behavior on cell level predictions. Theoretical predictions of individual component strain, capacity balance effects, porosity, and pressure were also explored. This model can be used to help designers to estimate pouch level volume change using knowledge of particle-level lithiation-based volume change behavior. The resulting understanding from the model may aid in cell design or in the determination of operational parameters to mitigate negative effects from active material volume change. Additionally, this model may prove useful to consider how mechanical and electrochemical phenomena intertwine as promising new chemistries are considered.

Finally, A multi-scale mechano-electrochemical modeling method was shown that simulates behavior of batteries that contain blended Si/C anodes. The model development included an adaptation to treat active materials within the same electrode separately. One of the primary insights gained from this study is the understanding of how active materials will preferentially lithiate. The differing electrochemical parameters, primarily equilibrium potential, will dictate the rate at which active materials lithiate within the same electrode. From this study, it is shown that silicon will preferentially lithiate first and de-lithiate last when mixed with graphitic carbon. This has a significant impact on battery algorithms engineers who often rely on open circuit voltages for state-of-charge or state-of-life prediction. Simulating preferential lithiation not only yields a better understanding of electrochemical performance. Due to silicon's significantly higher volume change, the overall electrode and cell mechanical behavior are impacted by the preferential lithiation as well. Treating the active materials separately and predicting the preferential active material lithiation impact on both mechanical and electrochemical phenomena shows promise as a tool for designers who are developing batteries with blended electrodes. The insights that were gained from this study not only help to understand how mechanical behavior and electrochemical performance manifest within blended electrodes, but also may prove useful to engineers looking to understand, predict, and ultimately mitigate electrode degradation.

1.1 FUTURE WORK

Ai et al. recently studied the stress response inside electrode particles via a P2D model with mechanically coupled diffusion mechanics.(39) Their model accurately represented internal particle stress generation, with an explanation of why particle

fragmentation occurs near the separator. It would be interesting to observe how internal particle stresses generate using a “separate-particle model” method to gain insight to how fracturing stresses appear in blended-anodes with preferential lithiation. Additionally, some scientists have proposed using core-shell particles to control which active material interfaces with electrolyte. Development of a model to capture the unique diffusion through a core-shell particle would be a useful tool alongside the “separate particle model” which simulates electrodes that are made by blending two active material powders in a slurry.

As is, the model developments shown in this dissertation show promise as a tool to inform cell designers how behavior at the active material particle scale affect electrode, cell, and pack level mechano-electrochemical phenomena. However, the next key step for predictive ability would be the development of a method to link the mechano-electrochemical behavior at each of these scales to the sub-particle scale to predict mechanical degradation of the electrode. Some of the difficulty in this is that particle-particle and grain-grain interactions are difficult to observe, and therefore, difficult to mathematically describe. However, a combination of experimental observation, such as electron backscatter diffraction, and 3D modeling may be used to derive a reduced order model to simulate these interactions with computational efficiency. A success in this effort would involve the ability to simulate the cell under a given face pressure while predicting the accelerated capacity fade, like the phenomena observed by Cannarela.(45) The field of mechano-electrochemical, multi-scale battery modeling is rapidly developing and shows promise to continue delivering unique insights into battery behavior.

REFERENCES

1. C. Harto, *Consumer Reports* (2019).
2. R. Petibon, V. Chevrier, C. Aiken, D. Hall, S. Hyatt, R. Shunmugasundaram and J. Dahn, *Journal of The Electrochemical Society*, **163**, A1146 (2016).
3. H. Wang, Y. I. Jang, B. Huang, D. R. Sadoway and Y. M. Chiang, *Journal of the Electrochemical Society*, **146**, 473 (1999).
4. J. Ji, J. Liu, L. Lai, X. Zhao, Y. Zhen, J. Lin, Y. Zhu, H. Ji, L. L. Zhang and R. S. Ruoff, *Acs Nano*, **9**, 8609 (2015).
5. P. Keil, S. F. Schuster, J. Wilhelm, J. Travi, A. Hauser, R. C. Karl and A. Jossen, *Journal of The Electrochemical Society*, **163**, A1872 (2016).
6. E. Markevich, G. Salitra and D. Aurbach, *Journal of The Electrochemical Society*, **163**, A2407 (2016).
7. V. P. Nemani, S. J. Harris and K. C. Smith, *Journal of The Electrochemical Society*, **162**, A1415 (2015).
8. V. R. Subramanian, P. Yu, B. N. Popov and R. E. White, *Journal of power sources*, **96**, 396 (2001).
9. P. Yu, J. A. Ritter, R. E. White and B. N. Popov, *Journal of the Electrochemical Society*, **147**, 1280 (2000).
10. K. G. Gallagher, S. Goebel, T. Greszler, M. Mathias, W. Oelerich, D. Eroglu and V. Srinivasan, *Energy & Environmental Science*, **7**, 1555 (2014).
11. S. K. Martha, O. Haik, E. Zinigrad, I. Exnar, T. Drezen, J. H. Miners and D. Aurbach, *Journal of the Electrochemical Society*, **158**, A1115 (2011).
12. C. Pillot, in *31st International Battery Seminar & Exhibit*, p. 5 (2015).
13. G. Berckmans, M. Messagie, J. Smekens, N. Omar, L. Vanhaverbeke and J. Van Mierlo, *Energies*, **10**, 1314 (2017).
14. Y. Zheng, X. Hao, J. Niu and B. Pan, *Materials Letters*, **163**, 98 (2016).
15. A. R. Armstrong and P. G. Bruce, *Nature*, **381**, 499 (1996).
16. F. Capitaine, P. Gravereau and C. Delmas, *Solid State Ionics*, **89**, 197 (1996).

17. J. Reimers, E. W. Fuller, E. Rossen and J. Dahn, *Journal of the Electrochemical Society*, **140**, 3396 (1993).

18. T. F. Fuller, M. Doyle and J. Newman, *Journal of the Electrochemical Society*, **141**, 1 (1994).

19. M. Doyle and J. Newman, *Journal of Power Sources*, **54**, 46 (1995).

20. M. Doyle and J. Newman, *Journal of Applied Electrochemistry*, **27**, 846 (1997).

21. D. Zhang, B. N. Popov and R. E. White, *Journal of the Electrochemical Society*, **147**, 831 (2000).

22. S. Santhanagopalan, Q. Guo, P. Ramadass and R. E. White, *Journal of power sources*, **156**, 620 (2006).

23. G. Ning, R. E. White and B. N. Popov, *Electrochimica acta*, **51**, 2012 (2006).

24. L. Cai and R. E. White, *Journal of Power Sources*, **196**, 5985 (2011).

25. P. Arora, M. Doyle, A. S. Gozdz, R. E. White and J. Newman, *Journal of power Sources*, **88**, 219 (2000).

26. M. Doyle, J. Newman, A. S. Gozdz, C. N. Schmutz and J. M. Tarascon, *Journal of the Electrochemical Society*, **143**, 1890 (1996).

27. P. Ramadass, B. Haran, P. M. Gomadam, R. White and B. N. Popov, *Journal of the Electrochemical Society*, **151**, A196 (2004).

28. X. Zhang, W. Shyy and A. M. Sastry, *Journal of the Electrochemical Society*, **154**, A910 (2007).

29. J. Park, W. Lu and A. M. Sastry, *Journal of the Electrochemical Society*, **158**, A201 (2010).

30. A. Mauger, H. Xie and C. M. Julien, *AIMS Materials Science*, **3**, 1054 (2016).

31. B. Boukamp, G. Lesh and R. Huggins, *Journal of the Electrochemical Society*, **128**, 725 (1981).

32. J. Christensen and J. Newman, *Journal of Solid State Electrochemistry*, **10**, 293 (2006).

33. U. Kasavajjula, C. Wang and A. J. Appleby, *Journal of power sources*, **163**, 1003 (2007).

34. D. Larcher, S. Beattie, M. Morcrette, K. Edstroem, J.-C. Jumas and J.-M. Tarascon, *Journal of Materials Chemistry*, **17**, 3759 (2007).

35. M. Obrovac, L. Christensen, D. B. Le and J. R. Dahn, *Journal of The Electrochemical Society*, **154**, A849 (2007).

36. X. H. Liu, L. Zhong, S. Huang, S. X. Mao, T. Zhu and J. Y. Huang, *ACS nano*, **6**, 1522 (2012).

37. K. Zhao, W. L. Wang, J. Gregoire, M. Pharr, Z. Suo, J. J. Vlassak and E. Kaxiras, *Nano letters*, **11**, 2962 (2011).

38. J. R. Szczech and S. Jin, *Energy & Environmental Science*, **4**, 56 (2011).

39. W.-J. Zhang, *Journal of Power Sources*, **196**, 877 (2011).

40. J. H. Ryu, J. W. Kim, Y.-E. Sung and S. M. Oh, *Electrochemical and Solid State Letters*, **7**, A306 (2004).

41. S. Golmon, K. Maute, S.-H. Lee and M. L. Dunn, *Applied Physics Letters*, **97**, 033111 (2010).

42. Y.-T. Cheng and M. W. Verbrugge, *Journal of the Electrochemical Society*, **157**, A508 (2010).

43. R. Parrish, K. Elankumaran, M. Gandhi, B. Nance, P. Meehan, D. Milburn, S. Siddiqui and A. Brenz, Voltec battery design and manufacturing, in, SAE Technical Paper (2011).

44. A. Papathanassiou, *Journal of Physics and Chemistry of Solids*, **58**, 2107 (1997).

45. J. Cannarella and C. B. Arnold, *Journal of Power Sources*, **245**, 745 (2014).

46. X. Zhang, A. M. Sastry and W. Shyy, *Journal of The Electrochemical Society*, **155**, A542 (2008).

47. M. Jain and J. W. Weidner, *Journal of The Electrochemical Society*, **146**, 1370 (1999).

48. M. Jain, G. Nagasubramanian, R. G. Jungst and J. W. Weidner, *Journal of the Electrochemical Society*, **146**, 4023 (1999).

49. R. Chandrasekaran, A. Magasinski, G. Yushin and T. F. Fuller, *Journal of the Electrochemical Society*, **157**, A1139 (2010).

50. R. Chandrasekaran and T. F. Fuller, *Journal of The Electrochemical Society*, **158**, A859 (2011).

51. P. M. Gomadam and J. W. Weidner, *Journal of The Electrochemical Society*, **153**, A179 (2005).

52. T. R. Garrick, K. Higa, S.-L. Wu, Y. Dai, X. Huang, V. Srinivasan and J. W. Weidner, *Journal of The Electrochemical Society*, **164**, E3592 (2017).

53. T. R. Garrick, X. Huang, V. Srinivasan and J. W. Weidner, *Journal of The Electrochemical Society*, **164**, E3552 (2017).

54. T. R. Garrick, K. Kanneganti, X. Huang and J. W. Weidner, *Journal of The Electrochemical Society*, **161**, E3297 (2014).

55. W. Mai, A. Colclasure and K. Smith, *Journal of the Electrochemical Society*, **166**, A1330 (2019).

56. W. Ai, L. Kraft, J. Sturm, A. Jossen and B. Wu, *Journal of The Electrochemical Society*, **167**, 013512 (2019).

57. Y. Dai, L. Cai and R. E. White, *Journal of power sources*, **247**, 365 (2014).

58. T. R. Garrick, D. J. Pereira and J. W. Weidner, in *ECS Meeting Abstracts*, p. 219 (2019).

59. D. J. Pereira, J. W. Weidner and T. R. Garrick, *Journal of The Electrochemical Society*, **166**, A1251 (2019).

60. W.-J. Zhang, *Journal of Power Sources*, **196**, 13 (2011).

61. C. Paireau, S. Jouanneau, M.-R. Ammar, P. Simon, F. Béguin and E. Raymundo-Piñero, *Electrochimica Acta*, **174**, 361 (2015).

62. J. Yang, B. Wang, K. Wang, Y. Liu, J. Xie and Z. Wen, *Electrochemical and solid state letters*, **6**, A154 (2003).

63. R. Dash and S. Pannala, *Mater. Today*, **19**, 483 (2016).

64. C. Zhang, J. Xu, L. Cao, Z. Wu and S. Santhanagopalan, *Journal of Power Sources*, **357**, 126 (2017).

65. G. Y. Gor, J. Cannarella, J. H. Prévost and C. B. Arnold, *Journal of the Electrochemical Society*, **161**, F3065 (2014).

66. L. Yang and V. Shim, *International journal of impact engineering*, **30**, 1099 (2004).

67. M. Doyle, T. F. Fuller and J. Newman, *Journal of the Electrochemical society*, **140**, 1526 (1993).

68. T. R. Garrick, Y. Dai, K. Higa, V. Srinivasan and J. W. Weidner, *Ecs Transactions*, **72**, 11 (2016).

69. Y. Qi, H. Guo, L. G. Hector and A. Timmons, *Journal of The Electrochemical Society*, **157**, A558 (2010).

70. Y. Reynier, R. Yazami and B. Fultz, *Journal of power sources*, **165**, 616 (2007).

71. O. Dolotko, A. Senyshyn, M. Mühlbauer, K. Nikolowski and H. Ehrenberg, *Journal of Power Sources*, **255**, 197 (2014).

72. C. Zhang, S. Santhanagopalan, M. A. Sprague and A. A. Pesaran, *Journal of Power Sources*, **298**, 309 (2015).

73. D. Callister and D. G. Rethwisch, *Materials Science and Engineering, An Introduction, 7th Ed. ed. John Willey & Sons, Inc*, 19 (2007).

74. D. J. Pereira, M. Fernandez, K. C. Streng, J. Gao, T. R. Garrick and J. W. Weidner, in *ECS Meeting Abstracts*, p. 428 (2019).

75. D. J. Pereira, M. Fernandez, K. C. Streng, X. X. Hou, J. Gao, T. R. Garrick and J. W. Weidner, in *ECS Meeting Abstracts*, p. 1605 (2020).

76. D. J. Pereira, M. A. Fernandez, K. C. Streng, X. X. Hou, X. Gao, J. W. Weidner and T. R. Garrick, *Journal of The Electrochemical Society*, **167**, 080515 (2020).

77. O. Egbue and S. Long, *Energy policy*, **48**, 717 (2012).

78. B. Boukamp, G. Lesh and R. Huggins, *Journal of The Electrochemical Society*, **128**, 725 (1981).

79. J. Christensen and J. Newman, *Journal of The Electrochemical Society*, **153**, A1019 (2006).

80. X. Zhang, A. M. Sastry and W. Shyy, *Journal of The Electrochemical Society*, **155**, A542 (2008).

81. M. A. Ansari, P. Y. Kumbhar and N. Swaminathan, *Journal of The Electrochemical Society*, **166**, A2574 (2019).

82. J. Park, W. Lu and A. M. Sastry, *Journal of The Electrochemical Society*, **158**, A201 (2011).

83. J. Shim and K. A. Striebel, *Journal of power sources*, **130**, 247 (2004).

84. H. Zheng, L. Zhang, G. Liu, X. Song and V. S. Battaglia, *Journal of Power Sources*, **217**, 530 (2012).

85. J. Xu, B. Liu and D. Hu, *Scientific reports*, **6**, 21829 (2016).

86. W. Mai, A. Colclasure and K. Smith, *Journal of The Electrochemical Society*, **166**, A1330 (2019).

87. W. Ai, L. Kraft, J. Sturm, A. Jossen and B. Wu, *Journal of The Electrochemical Society*, **167**, 013512 (2020).

88. J. Dahn, *Physical Review B*, **44**, 9170 (1991).

89. K.-W. Nam, W.-S. Yoon, H. Shin, K. Y. Chung, S. Choi and X.-Q. Yang, *Journal of power sources*, **192**, 652 (2009).

90. A. Louli, J. Li, S. Trussler, C. R. Fell and J. Dahn, *Journal of The Electrochemical Society*, **164**, A2689 (2017).

91. S.-W. Lee, K.-S. Kim, H.-S. Moon, J.-P. Lee, H.-J. Kim, B.-W. Cho, W.-I. Cho and J.-W. Park, *Journal of power sources*, **130**, 227 (2004).

92. R. M. Spotnitz, Trilayer battery separator, in, Google Patents (2001).

93. J.-P. Yen, C.-C. Chang, Y.-R. Lin, S.-T. Shen and J.-L. Hong, *Journal of The Electrochemical Society*, **160**, A1811 (2013).

94. . Wu, She-huang, and Po-Han Lee. *Journal of Power Sources* 349 (2017): 27-36.

95. J. Cannarella, X. Liu, C. Z. Leng, P. D. Sinko, G. Y. Gor and C. B. Arnold, *Journal of The Electrochemical Society*, **161**, F3117 (2014).

96. W. D. Callister, Jr. , *Materials Science and Engineering: An Introduction*, **7th Edition** (2007).

97. K. Raghunathan and B. J. Koch, Method and apparatus for monitoring a DC power source, in, Google Patents (2019).

98. D. J. Pereira, A. M. Aleman, T. R. Garrick, V. A. Sethuraman and J. W. Weidner, in *ECS Meeting Abstracts*, p. 1608 (2020).

99. T. Yoon, C. C. Nguyen, D. M. Seo and B. L. Lucht, *Journal of The Electrochemical Society*, **162**, A2325 (2015).

100. P. M. Gomadam and J. W. Weidner, *Journal of The Electrochemical Society*, **153**, A179 (2006).

101. P. M. Gomadam, D. R. Merritt, E. R. Scott, C. L. Schmidt, P. M. Skarstad and J. W. Weidner, *Journal of the Electrochemical Society*, **154**, A1058 (2007).

102. P. Albertus, J. Christensen and J. Newman, *Journal of the Electrochemical Society*, **156**, A606 (2009).

103. S. Jung, *Journal of Power Sources*, **264**, 184 (2014).

104. M. Petit, E. Calas and J. Bernard, *Journal of Power Sources*, **479**, 228766 (2020).

105. P. Yu, B. N. Popov, J. A. Ritter and R. E. White, *Journal of The Electrochemical Society*, **146**, 8 (1999).

106. C. J. Wen and R. A. Huggins, *Journal of solid state chemistry*, **37**, 271 (1981).

107. D. Allart, M. Montaru and H. Gualous, *Journal of The Electrochemical Society*, **165**, A380 (2018).

108. H. Xie, W. Qiu, H. Song and J. Tian, *Journal of The Electrochemical Society*, **163**, A2685 (2016).

109. J. Cannarella, X. Liu, C. Z. Leng, P. D. Sinko, G. Y. Gor and C. B. Arnold, *Journal of The Electrochemical Society*, **161**, F3117 (2014).

110. O. Barbarisi, F. Vasca and L. Glielmo, *Control Engineering Practice*, **14**, 267 (2006).

111. H. He, R. Xiong, X. Zhang, F. Sun and J. Fan, *IEEE Transactions on vehicular technology*, **60**, 1461 (2011).

112. P. Shrivastava, T. K. Soon, M. Y. I. B. Idris and S. Mekhilef, *Renewable and Sustainable Energy Reviews*, **113**, 109233 (2019).

113. D. R. Baker and M. W. Verbrugge, *Journal of The Electrochemical Society*, **160**, A1319 (2013).

114. L. Cai and R. E. White, *Journal of the Electrochemical Society*, **156**, A154 (2008).

115. N. Ding, J. Xu, Y. Yao, G. Wegner, X. Fang, C. Chen and I. Lieberwirth, *Solid State Ionics*, **180**, 222 (2009).